

SCHOOL OF ENGINEERING
UNIVERSITY OF PRETORIA



**DEVELOPMENT OF PARALLEL STRONGLY
COUPLED HYBRID FLUID-STRUCTURE
INTERACTION TECHNOLOGY INVOLVING
THIN GEOMETRICALLY NON-LINEAR
STRUCTURES**

RIDHWAAN SULIMAN

SUPERVISORS: DR. S. KOK, PROF. A.G. MALAN AND PROF. J.P. MEYER

THESIS SUBMITTED TO THE UNIVERSITY OF PRETORIA IN CANDIDATURE
FOR THE DEGREE OF MASTERS IN ENGINEERING

NOVEMBER 2011

Abstract

This work details the development of a computational tool that can accurately model strongly-coupled fluid-structure-interaction (FSI) problems, with a particular focus on thin-walled structures undergoing large, geometrically non-linear deformations, which has a major interest in, amongst others, the aerospace and biomedical industries.

The first part of this work investigates improving the efficiency with which a stable and robust in-house code, *Elemental*, models thin structures undergoing dynamic fluid-induced bending deformations. Variations of the existing finite volume formulation as well as linear and higher-order finite element formulations are implemented. The governing equations for the solid domain are formulated in a total Lagrangian or undeformed configuration and large geometrically non-linear deformations are accounted for. The set of equations is solved via a single-step Jacobi iterative scheme which is implemented such as to ensure a matrix-free and robust solution. Second-order accurate temporal discretisation is achieved via dual-timestepping, with both consistent and lumped mass matrices and with a Jacobi pseudo-time iteration method employed for solution purposes. The matrix-free approach makes the scheme particularly well-suited for distributed memory parallel hardware architectures. Three key outcomes, not well documented in literature, are highlighted: the issue of shear locking or sensitivity to element aspect ratio, which is a common problem with the linear Q4 finite element formulation when subjected to bending, is evaluated on the finite volume formulations; a rigorous comparison of finite element vs. finite volume methods on geometrically non-linear structures is done; a higher-order finite volume solid mechanics procedure is developed and evaluated.

The second part of this work is concerned with fluid-structure interaction (FSI) modelling. It considers the implementation and coupling of a higher-order finite element structural solver with the existing finite volume fluid-flow solver in *Elemental*. To the author's knowledge, this is the first instance in which a strongly-coupled hybrid finite element–finite volume FSI formulation is developed. The coupling between the fluid and structural components with non-matching nodes is rigorously assessed. A new partitioned fluid-solid interface coupling methodology is also developed, which ensures stable partitioned solution for strongly-coupled problems without any additional computational overhead. The solver is parallelised for distributed memory parallel hardware architectures. The developed technology is successfully validated through rigorous temporal and mesh independent studies of representative two-dimensional strongly-coupled large-displacement FSI test problems for which analytical or benchmark solutions exist.

Acknowledgements

I would like first and foremost to express my utmost gratitude to my supervisors, Prof. Arnaud Malan and Dr. Schalk Kok, for their guidance and support. Your advice and patience have enabled me to develop an understanding of the subject.

To all my colleagues at the CSIR and specifically at the Advanced Computational Methods research group, thank you for your interest and insightful discussions. Special recognition and thanks must go to my colleague and friend, Dr. Oliver Oxtoby. You have provided advice and assistance at various stages throughout this project and your friendship in times of trial and jubilation has been invaluable.

I would like to take this opportunity to thank my family and friends. To my brothers, Mohamed and Raihaan, for their advice, motivation and fruitful discussions. Special thanks to Raihaan for taking me on all the adventures during this time: not only have they kept me sane, but they were thoroughly enjoyable too. Finally, I am indebted to my parents who have been a constant source of advice, encouragement, motivation and support. Your love and motivation have kept me going and seen me through this long journey. Without you, none of this would have been possible.

Contents

Abstract	i
Acknowledgements	ii
Nomenclature	v
List of Figures	ix
List of Tables	xi
1 Introduction	1
1.1 Background and Purpose of Study	1
1.2 Project Outline	3
1.3 Publication List	5
1.3.1 Journal Papers	5
1.3.2 Conference Papers	5
1.3.3 Poster Presentation	5
I Geometrically Non-Linear Structures	6
2 Problem Formulation	7
2.1 Introduction	7
2.2 Governing Equations	7
2.3 Constitutive Equations	11
2.4 Boundary Conditions	12
2.5 Conclusion	13
3 Numerical Discretisation Procedures	14
3.1 Introduction	14
3.2 Method of Weighted Residuals	14
3.3 FEM vs. FVM for Solid Mechanics	16
3.4 Spatial Discretisation: Finite Element Method	17
3.4.1 Q4 Finite Element Method	20
3.4.2 Q8 Finite Element Method	22
3.5 Spatial Discretisation: Finite Volume Method	23
3.5.1 Vertex-centred Finite Volume Method	24
3.5.2 Hybrid Finite Volume Method	26
3.5.3 Proposed Higher-Order Finite Volume Method	27

3.6	Temporal Discretisation and Solution Procedure	33
3.7	Conclusion	37
4	Numerical Results and Evaluation	38
4.1	Introduction	38
4.2	Uniaxial Tension	38
4.3	Simple Shear	39
4.4	Pure Bending	41
4.4.1	Error Analysis: Application to Beam in Pure Bending	42
4.5	Thin Cantilever Beam in Non-linear Bending	44
4.5.1	Error Analysis: Application to Thin Beam in Bending	45
4.6	Dynamic 2D Beam	48
4.7	Conclusion	49
II	Fluid-Structure Interaction	52
5	Fluid-Structure Interaction: Implementation	53
5.1	Introduction	53
5.2	Fluid Governing Equation Set	54
5.3	Fluid Constitutive Equations	55
5.4	Fluid-Solid Interface Treatment	55
5.4.1	Consistent Nodal Loads	55
5.4.2	FSI Interface Coupling Scheme	58
5.5	Parallelisation	59
5.6	Mesh Movement and Solution Procedure	59
5.7	Conclusion	60
6	Fluid-Structure Interaction: Validation and Verification	61
6.1	Introduction	61
6.2	Dynamic Piston-channel System	61
6.3	Block-tail in Second Mode of Vibration	64
6.4	Block-tail in First Mode of Vibration	70
6.5	Conclusion	73
7	Conclusions and Future Work	74
7.1	Consolidation of Work Performed	74
7.2	Future Work	75
A	Error Analysis: Analytical Approach	76
B	Derivation of Third-Order Gradient Approximation	93
	References	95

Nomenclature

Roman Symbols

a	Acceleration (m/s^2)
A	Boundary surface of control volume (m^2)
B	Derivatives of shape functions
B_{mn}	Boundary edge coefficient connecting nodes m and n (m^2)
b	Body force in deformed configuration (N/m^3)
b_o	Body force in undeformed configuration (N/m^3)
b	thickness (m)
C_{mn}	Internal edge coefficient connecting nodes m and n (m^2)
C	Fourth order elasticity tensor or material matrix
c	Half the thickness of beam (m)
E	Green-Lagrange strain
E	Young's modulus of material (Pa)
F_{i,j}	Deformation gradient
F	External forces or loads (N)
G	Shear modulus (Pa)
H	Displacement gradient
I	Moment of inertia of beam ($kg.m^2$)
J	Jacobian matrix
K	Bulk modulus (Pa)
k	Spring constant (N/m)

L	Length of beam (m)
l_j	Length of an edge (m)
m	Mass of body (kg)
M_e	Mass matrix of element (kg)
M	Bending-moment ($N.m$)
\mathbf{n}	Outward pointing unit normal vector
\mathbf{N}	Basis or shape functions
\mathbf{P}	First Piola-Kirchoff stress (Pa)
p	Pressure (Pa)
\mathbf{R}	Residual of equation
Re	Reynolds number
RHS	Right-hand-side of algebraic equation
\mathbf{S}	Second Piola-Kirchoff stress (Pa)
t	Time (s)
\mathbf{t}	Surface traction (N/m^2)
\mathbf{u}	Displacement (m)
U	Nodal displacements (m)
\ddot{U}	Nodal accelerations (m/s^2)
\bar{u}	Projected displacement (m)
\mathbf{v}	Velocity (m/s)
\mathcal{V}_m	Control volume (m^3)
\mathcal{V}	Volume in deformed configuration (m^3)
\mathcal{V}_o	Volume in undeformed configuration (m^3)
\mathbf{w}	Weighting field
W_{GP}	Gauss quadrature weighting factor
W	Nodal weighting values
\mathbf{x}	Coordinate of point on body in deformed configuration (m)
\mathbf{X}	Coordinate of point on body in undeformed configuration (m)

Greek Symbols

η	Coordinate in natural or transformed space
λ	Eigenvalue of mode of oscillation
μ	Viscosity of fluid (kg/ms)
ω	Frequency of oscillation (Hz)
ρ	Density in deformed configuration (kg/m^3)
ρ_o	Density in undeformed configuration (kg/m^3)
σ	Cauchy stress (Pa)
τ	Pseudo-time (s)
ν	Poisson's ratio of material
Υ_{mn}	Edge connecting nodes m and n
φ	Slope of beam
ξ	Coordinate in natural or transformed space

Superscripts

e	Element
p	Prescribed
T	Transpose of a matrix

Subscripts

cons	Consistent mass
cr	Critical
e	Element
ext	External
f	Fluid
in	Inlet
int	Interface
lumped	Lumped mass
m	Node index
n	Node index

normal Component in direction normal to edge

mn Edge connecting nodes m and n

s Solid

t Traction

u Displacement

Mathematical Operators

$\det \bullet$ Determinant of \bullet

$\text{Div} \bullet$ Divergence of \bullet

\cdot Dot product

$\nabla \bullet$ Gradient operator of \bullet

$\Delta \bullet$ Increment in \bullet

δ_{ij} Kronecker delta operator: unity if $i = j$ and zero if $i \neq j$

$|\bullet|$ Norm of \bullet

$\partial \bullet$ Partial derivative of \bullet

Notes on Notation

Both vector and index notation are used in this thesis. Vectors and matrices are denoted in bold. Where index notation is used, component subscripts may appear as super or subscripts and are typically denoted by i , j and k . Einstein's summation convention is implied in the case of index notation.

List of Figures

2.1	Solid body in undeformed and deformed configurations	8
3.1	Schematic of the finite element method on a 2D unstructured mesh	15
3.2	Two variants of the finite volume method on 2D unstructured grids: element-based or cell-centred (left) and node-based or vertex-centred (right)	16
3.3	Isoparametric Q4 element in physical space (left) and reference space (right)	20
3.4	Isoparametric Q8 element in physical space (left) and reference space (right)	23
3.5	Schematic of the construction of a dual-mesh	25
3.6	Schematic of a mesh showing the calculation of element-based gradients	27
3.7	Schematic of the mesh indicating an internal, boundary and corner node	29
3.8	Schematic of the mesh indicating a boundary node	32
3.9	Schematic of the mesh indicating a corner node	33
4.1	Solid body in uniaxial tension	39
4.2	Comparison of σ_{11} stress for uniaxial tension	39
4.3	Solid body in simple shear	40
4.4	Comparison of σ_{11} and σ_{12} stress for simple shear	40
4.5	Cantilever beam in pure bending	41
4.6	Meshes with varying element aspect ratios used for analysing a beam in pure bending	42
4.7	Tip displacement as a function of element aspect ratio: (a) Q4 and Q8 FEM; (b) vertex-centred, hybrid and higher-order FVM .	43
4.8	Thin cantilever beam undergoing large non-linear displacements .	44
4.9	Calculated beam deflection for various meshes: (a) Vertex-centred FVM; (b) Hybrid FVM; (c) Higher-order FVM; (d) Q4 FEM; (e) Q8 FEM	46
4.10	Tip displacement as a function of element aspect ratio for a thin cantilever beam subjected to a concentrated tip load	47
4.11	Convergence rate of displacements	48

4.12	Dynamic beam with applied shear	49
4.13	Transient response of a cantilever beam when a shear traction of 0.1 Pa is suddenly applied at the free end: (a) Q8 40×1 mesh; (b) using different timesteps and mesh sizes	50
5.1	Arbitrary solid edge along the FSI interface	56
6.1	Geometry and boundary conditions for the piston-channel system	62
6.2	Representative spring-mass system for the piston-channel configuration	62
6.3	Displacement (left) and velocity (right) of the interface of the piston and channel	63
6.4	Displacement (left) and velocity (right) of the interface of the piston-channel using various meshes	63
6.5	Velocity contours of the piston and pressure contours of the fluid at various times	64
6.6	Geometry and boundary conditions for the block-tail FSI test-case	65
6.7	Block-tail test-case: (a) and (b) 6 000 element fluid mesh. (c) and (d) Plots of the deformed mesh	65
6.8	Pressure (left) and velocity contours (right) for the block-tail test-case with the beam oscillating in its second mode of vibration	66
6.9	Tip displacement for the block-tail test-case in second mode of vibration with various meshes and timestep sizes	68
6.10	Block-tail test-case: 25 000 (left) and 50 000 cell (right) fluid mesh	69
6.11	Tip displacement for the block-tail test-case in second mode of vibration using consistent and lumped traction forces at the interface	69
6.12	Block-tail test-case: Plots of the deformed mesh with the beam oscillating in its first mode of vibration	71
6.13	Pressure (left) and velocity contours (right) for the block-tail test-case with the beam oscillating in its first mode of vibration	71
6.14	Tip displacement for the block-tail test-case in first mode of vibration with various meshes and timestep sizes	72
A.1	Schematic of the mesh indicating an internal node	77
A.2	Schematic of the mesh indicating a boundary node	83
A.3	Schematic of the mesh indicating a corner node	88
B.1	Schematic of mesh indicating a boundary node at the bottom boundary of a beam	94

List of Tables

3.1	Order of accuracy of the vertex-centred and hybrid formulations	31
4.1	Errors of vertex-centred and hybrid formulations for a beam in pure bending	43
4.2	Errors of vertex-centred and hybrid formulations for a cantilever beam subjected to a tip load	47
6.1	Comparison of amplitude and frequency for the block-tail test-case in second mode of vibration with various meshes and timestep sizes	67
6.2	Piecewise-constant force as a function of time applied to tip of beam to reproduce initial deflection in results of [1].	70
6.3	Comparison of amplitude and frequency for the block-tail test-case in first mode of vibration with various meshes and timestep sizes	73

Chapter 1

Introduction

1.1 Background and Purpose of Study

Computational mechanics is a growing discipline which uses computational methods to obtain approximate solutions to problems governed by the principles of mechanics. With the massive advances in computer technology over the past few decades, computational mechanics has become an important tool in analysing complex physical phenomena and has had a significant influence on science and technology.

Fluid-structure interaction (FSI) constitutes a branch of computational mechanics in which there exists an intimate coupling between fluid and structural or solid domains; the behaviour of the system is influenced by the interaction of a moving fluid and a flexible solid structure. There are a wide variety of FSI problems encountered in many areas of aerospace, biomedical, mechanical and civil engineering. Examples of such problems include wing flutter on aircraft [2,3], flows in elastic pipes and blood vessels [4,5], heart valve dynamics [6], structural loads on ships [7], flow induced vibrations in nuclear power plants [8] and wind response of buildings [9]. Though much effort has been spent over recent years in developing FSI modelling technology [1,10–14], significant scope for improvement still exists in terms of industrial relevance and impact.

The purpose of this study is to furnish a computational tool that can accurately model strongly-coupled FSI problems, with a particular focus on thin-walled structures undergoing large, non-linear deformations. At the commencement of this study, a stable and robust in-house code, *Elemental*, was available [15,16]. It is a novel multi-physics parallel code with fluid-structure interaction [17,18] and free-surface-modelling [19] capabilities. With reference to FSI, the solver makes use of a compact edge-based vertex-centred finite volume approach to model both fluid and structures in a strongly-coupled partitioned manner. While the aforementioned edge-based approach has been demonstrated to be effective for the fluid domain, thin structures have been found to require many elements through the thickness to ensure accuracy [20].

The first objective of this study is to improve the efficiency with which *Elemental* models thin structures undergoing dynamic fluid-induced bending deformations. Shell theory is normally used for modelling thin-walled structures, where the wall thickness is negligible compared to other dimensions. However, for structures with a thin but moderate wall thickness and to account for a wall with varying thickness, it is more appropriate to use a solid element of finite thickness. Furthermore, with a solid element detailed stress distributions within the structure can be obtained, which can provide more insight of engineering interest. This leaves the choice of either the finite element method or finite volume method. Both schemes can be considered as methods of weighted residuals where they differ in the choice of the weighting function. Since the 1960s, the finite element method [21] has been used for modelling the mechanics of solids, but over the last two decades use of the finite volume method [22] has received increased attention. As a result, many studies have been conducted over the last two decades on the application of the finite volume method to linear elastic structures [23–28]. However, the optimal choice of numerical scheme for all cases still remains open.

It is well known that the linear finite element formulation suffers from sensitivity to element aspect ratio or shear locking when subjected to bending [29]. Fallah [28] and Wheel [26] present a locking-free finite volume approximation to Mindlin-Reissner plates for both cell-centred and vertex-centred formulations. However, using solid elements, Wenke and Wheel [30] present results that do indicate shear locking with the displacement-based vertex-centred finite volume approach. Further, little work has been done on the use of finite volume methods to model structures undergoing bending deformations. A more rigorous evaluation of the suitability of the finite volume method for modelling such systems is therefore required.

When considering geometrically non-linear solid mechanics problems as seen in this work, Fallah et al. [31] presented a finite volume procedure and also compared the results with the finite element method. They concluded that for a low mesh density the difference between the finite volume and finite element methods are considerable, but by increasing the number of elements the accuracy of the two methods are comparable. On the other hand, Vaz Jr. et al. [32] state that the finite element formulation provides higher accuracy for displacement solutions. The question of finite element vs. finite volume still remains unanswered. In addition, the finite element Galerkin method uses shape functions as the weighting functions, which allows natural extension to higher-order via higher-order polynomials for the shape functions [21]. This is of particular interest to thin structures under non-linear bending, where at the least a cubic displacement field results. The finite volume method results by choosing the weighting function as unity. Although higher-order accurate finite volume methods have been used extensively in computational fluid dynamics [33,34], to the author’s knowledge no higher-order finite volume method for computational solid mechanics has been presented.

The most suitable solid modelling method is to be implemented within the existing *Elemental* framework and applied to FSI applications. Many recent FSI

efforts have made use of a single discretisation scheme, either finite volume [11, 13, 14, 35] or finite element [1, 10, 36–39], to solve the entire domain. However, each method contains certain inherent advantages and should be used as such. Since the framework within *Elemental* is independent of discretisation strategy employed, it allows for the development of a hybrid finite volume–finite element FSI formulation. To the author’s knowledge, to date no hybrid formulation has been successfully applied to strongly-coupled FSI problems.

The solution of FSI systems range from single or monolithic methods that are inherently strongly-coupled to separate or partitioned methods that can be strongly- or weakly-coupled. This work focusses on FSI systems where there are strong interactions between the fluid and structural domains and weakly-coupled methods are, therefore, not considered as they may diverge or result in inaccurate solutions [1, 10, 11]. For strongly-coupled methods, the advantage of a monolithic over a partitioned approach is that all the equations are considered simultaneously and a single system of equations is solved, which ensures stability and convergence. However, this approach may suffer from ill conditioning and convergence is generally slow [1]. The advantage of a partitioned approach is that it allows the use of two independent solution techniques for the fluid and solid equations in isolation. The drawback of partitioned approaches is that they generally require a separate coupling algorithm or additional outer iterations between the fluid and solid to achieve strong-coupling, which places an additional computational cost on the scheme [1, 40, 41]. The most popular partitioned coupling algorithms use fixed-point iteration methods or interface Newton-Krylov methods [40, 42]. Fixed-point methods generally make use of Gauss-Seidel iterations which are slow to converge and methods to accelerate convergence, including Aitken and steepest descent relaxation and coarse-grid preconditioning, have been used [41–45]. The Newton-Raphson methods require the computation of Jacobians, which may be difficult to compute exactly and various methods have been developed that use approximate Jacobians [46–48]. In this work the fluid and structural domains are to be solved in a strongly-coupled partitioned manner, where the transfer of information occurs at solver sub-iteration level negating the need for a separate coupling algorithm. To ensure solver stability and computational speed, a simple interface coupling algorithm is to be implemented at sub-iteration level. For scalability to large problems the scheme is to be implemented in a matrix-free approach and in such a manner that makes it particularly well-suited for distributed memory parallel hardware architectures. Finally, rigorous temporal and mesh independent studies are to be conducted on the developed FSI technology.

1.2 Project Outline

In summary from the above, the first objective of this study is to improve the efficiency with which *Elemental* models thin structures undergoing dynamic fluid-induced bending deformations. This involves the rigorous evaluation and comparison of variations of the existing formulation to finite element meth-

ods, as well as the development and evaluation of a higher-order finite volume method. This study will be limited to isotropic, elastic structures and will focus on representative two-dimensional problems. At the end of this part of the study a dynamic solid mechanics solution procedure capable of handling large non-linear deformations is to be developed.

The second objective of this study is to implement the most suitable solid modelling method into *Elemental* and couple with the existing fluid-flow solver. The coupling between the fluid and structural components is to be rigorously assessed and the developed FSI technology evaluated on strongly-coupled FSI test problems.

The dissertation is thus subdivided into two parts and seven chapters, including an introduction and conclusion. The first part focusses on the development and evaluation of the geometrically non-linear structural modelling technology, while the second details its application to FSI. The following is a synopsis of each chapter.

- *Chapter One: Introduction.* The background and motivation behind this project is discussed. In addition, this chapter contains the scope of work, research contributions made and gives an outline of the dissertation.

Part One: Geometrically Non-Linear Structures

- *Chapter Two: Problem Formulation.* The set of governing equations describing the mechanics of structures undergoing non-linear deflections, as well as the constitutive equations and boundary conditions employed in this work are presented.
- *Chapter Three: Numerical Discretisation Procedures.* Once the equations are formulated, it remains to be discretised and solved in an accurate and efficient manner. This process is the major focus of Part One of the dissertation. Two spatial discretisation techniques are investigated, viz. the finite volume and finite element methods. Variations of each are considered, an in-depth error analysis is conducted on the finite volume formulations and a higher-order accurate finite volume method developed. Furthermore, temporal discretisation and solution procedure are also discussed.
- *Chapter Four: Numerical Results and Evaluation.* Following on from the previous chapter, the implementation and numerical results for the different scheme variations are detailed. The preferred discretisation method for the solid domain is chosen.

Part Two: Fluid-Structure Interaction

- *Chapter Five: Fluid-Structure Interaction: Implementation.* A strongly-coupled parallel hybrid finite volume–finite element fluid-structure interaction scheme is developed. The coupling between the fluid and structural components is rigorously assessed. The solution procedure and implementation into *Elemental* are explained.

- *Chapter Six: Fluid-Structure Interaction: Validation and Verification.* The developed FSI technology is evaluated and benchmarked on representative two-dimensional strongly-coupled large-displacement FSI test problems.
- *Chapter Seven: Conclusions and Future Work.* The work done is consolidated in this chapter and recommendations are made for the continuation of this work through future research.

1.3 Publication List

The publications produced from this work follow:

1.3.1 Journal Papers

- SULIMAN R., OXTOBY O., MALAN A.G., KOK S., 'A novel finite volume method to model linear elastic structures', In Process.
- SULIMAN R., MALAN A.G., KOK S., OXTOBY O., 'A partitioned finite volume-finite element fluid-structure interaction scheme for strongly-coupled problems', In Process.

1.3.2 Conference Papers

- SULIMAN R., OXTOBY O., MALAN A.G., KOK S. (2010), 'An enhanced matrix-free edge-based finite volume approach to model structures', Proceedings of the 7th South African Conference on Computational and Applied Mechanics, SACAM10, Paper no. 074, Pretoria, South Africa, 10-13 January 2010.
- SULIMAN R., OXTOBY O., MALAN A.G., KOK S. (2011), 'Development of strongly coupled FSI technology involving thin walled structures', Proceedings of the 2nd African Conference on Computational Mechanics - An International Conference - AfriCOMP11, Cape Town, South Africa, 5-8 January 2011.

1.3.3 Poster Presentation

- SULIMAN R., OXTOBY O., MALAN A.G., KOK S. (2011), 'Development of strongly-coupled hybrid fluid-structure interaction technology involving thin geometrically non-linear structures', CSIR Emerging Researcher Symposium, Pretoria, South Africa, 13 October 2011.

Part I

**Geometrically Non-Linear
Structures**

Chapter 2

Problem Formulation

2.1 Introduction

The aim of this project is to develop the technology capable of solving strongly-coupled fluid-structure interaction problems involving thin structures. A stable and robust fluid-flow solver is available prior to the commencement of this study [16], whereas a similar solver for the structural component is required. The set of equations which describe a homogeneous isotropic elastic solid is presented in this chapter. Large non-linear displacements are to be accounted for and the equations are to be formulated in a total Lagrangian or undeformed configuration.

2.2 Governing Equations

Consider a homogeneous isotropic elastic solid undergoing large non-linear deformation. The partial differential equations that describe its motion are given by Cauchy's first equation of motion (balance of linear momentum) [49], which in local or strong form is

$$\nabla \cdot \boldsymbol{\sigma} + \mathbf{b} = \rho \mathbf{a}, \quad (2.1)$$

where $\boldsymbol{\sigma}$, \mathbf{b} , ρ and \mathbf{a} are the Cauchy stress, body force, density and acceleration respectively.

Equation (2.1) may be cast into global or weak form by integrating over an arbitrary spatial volume, \mathcal{V} ,

$$\int_{\mathcal{V}} (\nabla \cdot \boldsymbol{\sigma} + \mathbf{b} - \rho \mathbf{a}) d\mathcal{V} = \mathbf{0}. \quad (2.2)$$

For a solid undergoing large non-linear deformations it is necessary to distinguish between the body in the undeformed or reference configuration and that in the deformed or current configuration, as shown in Figure 2.1. The undeformed body is denoted by \mathcal{V}_0 whereas the deformed body, after undergoing a

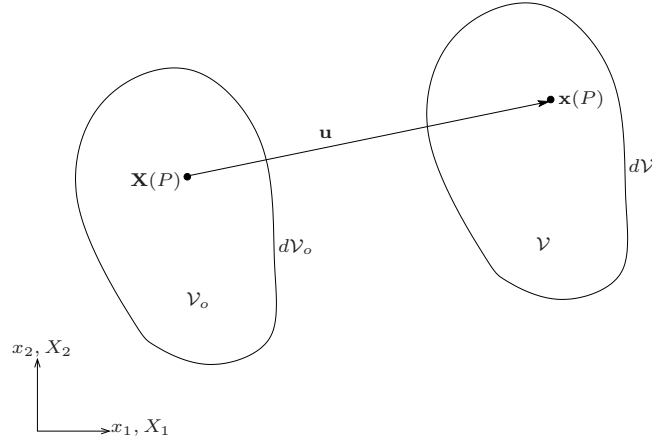


Figure 2.1: Solid body in undeformed and deformed configurations

displacement \mathbf{u} , is denoted by \mathcal{V} . The coordinates of any point P on the body are given by $\mathbf{X}(P)$ in the undeformed configuration and $\mathbf{x}(P)$ in the deformed configuration.

Equation (2.1) uses quantities defined in the deformed configuration and is therefore with respect to the current configuration. It is also referred to as an updated Lagrangian formulation [49]. The equilibrium equations may also be written with respect to the undeformed configuration, referred to as a total Lagrangian formulation [49]. The total and updated Lagrangian formulations are mathematically equivalent, and one formulation can be transformed to the other using a coordinate transformation and the chain rule of differentiation. The choice of formulation is typically viewed as a matter of convenience [50]. During this study, it was however found that when considering transient systems, the updated Lagrangian formulation results in the accumulation of temporal discretisation errors due to repeated oscillations with a resultant loss in geometric conservation. Also, the updated Lagrangian formulation requires the computation of integrals over domains in the deformed configuration, which are not known at the start of an analysis and must, therefore, be determined as part of the solution process. On the other hand, the total Lagrangian formulation needs no update, while the original configuration will always result when the structure returns to rest. As a result, the total Lagrangian formulation is selected for this work.

The transformation of the equilibrium equation, Equation (2.2), to a total Lagrangian description is shown next. Neglecting body forces and writing Equation (2.2) in indicial notation gives

$$\int_{\mathcal{V}} \rho a_i d\mathcal{V} = \int_{\mathcal{V}} \frac{\partial}{\partial x_j} \sigma_{ij} d\mathcal{V}. \quad (2.3)$$

Assuming no destruction or creation of mass, the density ρ is equal to the mass of the domain divided by the volume, therefore

$$\int_{\mathcal{V}} \frac{dm}{d\mathcal{V}} a_i d\mathcal{V} = \int_{\mathcal{V}} \frac{\partial}{\partial x_j} \sigma_{ij} d\mathcal{V}. \quad (2.4)$$

Now, we would like to express this relation in the undeformed configuration. As such, we introduce the deformation gradient, F_{iJ} , which relates quantities in the undeformed configuration to their counterparts in the deformed configuration:

$$F_{iJ} = \frac{\partial x_i}{\partial X_J} \quad (2.5)$$

where lowercase subscripts are used to refer to quantities in the current or deformed configuration while uppercase subscripts denote quantities in the undeformed configuration.

The volume integral in Equation (2.4) may now be transformed to the undeformed configuration by using the determinant of the deformation gradient [50], $d\mathcal{V} = \det(F_{iJ})d\mathcal{V}_o$, which gives

$$\int_{\mathcal{V}_o} \frac{dm}{\det(F_{iJ})d\mathcal{V}_o} a_i \det(F_{iJ})d\mathcal{V}_o = \int_{\mathcal{V}_o} \frac{\partial}{\partial x_j} \sigma_{ij} \det(F_{iJ})d\mathcal{V}_o. \quad (2.6)$$

The mass dm remains constant and noting that $\frac{dm}{d\mathcal{V}_o} = \rho_o$, which is the density in the undeformed configuration and is constant,

$$\rho_o \int_{\mathcal{V}_o} a_i d\mathcal{V}_o = \int_{\mathcal{V}_o} \frac{\partial}{\partial x_j} \sigma_{ij} \det(F_{iJ})d\mathcal{V}_o. \quad (2.7)$$

Noting that

$$\frac{\partial x_i}{\partial X_I} \frac{\partial X_I}{\partial x_j} = (F_{iI})(F^{-1})_{Ij} = \delta_{ij} \quad (2.8)$$

therefore, Equation (2.7) can be simplified by multiplying the RHS by a term equivalent to unity, using the chain rule of differentiation and manipulating as follows:

$$\rho_o \int_{\mathcal{V}_o} a_i d\mathcal{V}_o = \int_{\mathcal{V}_o} \frac{\partial \sigma_{ij}}{\partial x_j} \det(F_{iJ})d\mathcal{V}_o \quad (2.9)$$

$$= \int_{\mathcal{V}_o} \frac{\partial \sigma_{ij}}{\partial x_j} \frac{\partial X_J}{\partial X_J} \det(F_{iJ})d\mathcal{V}_o \quad (2.10)$$

$$= \int_{\mathcal{V}_o} \frac{\partial \sigma_{ij}}{\partial X_J} \frac{\partial X_J}{\partial x_j} \det(F_{iJ})d\mathcal{V}_o \quad (2.11)$$

$$= \int_{\mathcal{V}_o} \frac{\partial \sigma_{ij}}{\partial X_J} (F^{-1})_{Jj} \det(F_{iJ})d\mathcal{V}_o \quad (2.12)$$

$$= \int_{\mathcal{V}_o} \frac{\partial \sigma_{ij}}{\partial X_J} (F^{-T})_{jJ} \det(F_{iJ})d\mathcal{V}_o. \quad (2.13)$$

Now, using the product rule of differentiation, it can be shown that

$$\frac{\partial}{\partial X_J} [\det(F_{iJ})\sigma_{ij}(F^{-T})_{jJ}] = \frac{\partial}{\partial X_J} \left[\sigma_{ij} [\det(F_{iJ})(F^{-T})_{jJ}] \right] \quad (2.14)$$

$$= \frac{\partial \sigma_{ij}}{\partial X_J} \det(F_{iJ})(F^{-T})_{jJ} + \frac{\partial}{\partial X_J} [\det(F_{iJ})(F^{-T})_{jJ}] \sigma_{ij} \quad (2.15)$$

$$= \frac{\partial \sigma_{ij}}{\partial X_J} \det(F_{iJ})(F^{-T})_{jJ}, \quad (2.16)$$

since $\frac{\partial}{\partial X_J} [\det(F_{iJ})(F^{-T})_{jJ}] = 0$ from the Piola identity [49].

Therefore, Equation (2.13) simplifies to:

$$\rho_o \int_{\mathcal{V}_o} a_i d\mathcal{V}_o = \int_{\mathcal{V}_o} \frac{\partial}{\partial X_J} [\det(F_{iJ})\sigma_{ij}(F^{-T})_{jJ}] d\mathcal{V}_o. \quad (2.17)$$

Next, we make use of the Piola transformation [49], which relates the Cauchy stress to the first Piola-Kirchoff stress, P_{iJ} ,

$$\sigma_{ij} = \frac{1}{\det(F_{iJ})} P_{iJ} (F^T)_{jJ} \quad (2.18)$$

therefore,

$$P_{iJ} = \det(F_{iJ}) \overline{\sigma_{ij}} (F^{-T})_{jJ}. \quad (2.19)$$

The first Piola-Kirchoff stress is a stress measure defined in the undeformed configuration and relates forces in the deformed configuration with areas in the undeformed configuration.

Substituting Equation (2.19) into Equation (2.17) gives

$$\rho_o \int_{\mathcal{V}_o} a_i d\mathcal{V}_o = \int_{\mathcal{V}_o} \frac{\partial}{\partial X_J} P_{iJ} d\mathcal{V}_o \quad (2.20)$$

or

$$\rho_o \int_{\mathcal{V}_o} a_i d\mathcal{V}_o = \int_{\mathcal{V}_o} \nabla_X \cdot P_{iJ} d\mathcal{V}_o. \quad (2.21)$$

Written in vector form, Equation (2.21) becomes

$$\int_{\mathcal{V}_o} (\text{Div} \mathbf{P} - \rho_o \mathbf{a}) d\mathcal{V}_o = \mathbf{0}. \quad (2.22)$$

Equation (2.22) also holds for an arbitrary volume \mathcal{V}_o , therefore expressing it in strong form gives

$$\text{Div} \mathbf{P} = \rho_o \mathbf{a}. \quad (2.23)$$

If the body forces are not negligible, it can be shown [49] that the body force term in the undeformed configuration is related to its counterpart in the deformed configuration by

$$\mathbf{b}_o = \mathbf{b} \det(\mathbf{F}). \quad (2.24)$$

The complete equation of motion in the undeformed configuration therefore becomes

$$\text{Div} \mathbf{P} + \mathbf{b}_o = \rho_o \mathbf{a}, \quad (2.25)$$

where the nomenclature is as previously defined.

2.3 Constitutive Equations

In order to solve the elastic boundary value problem, Equation (2.25), a relationship between stress and displacement is required. This relation is obtained indirectly through the strain. Assuming an isotropic hyperelastic St-Venant-Kirchoff material model, the Green-Lagrange strain, \mathbf{E} , which is a strain measure in the undeformed configuration, is related to the stress by

$$\mathbf{S} = \mathcal{C} \mathbf{E}, \quad (2.26)$$

where \mathbf{S} is the second Piola-Kirchoff stress, a stress tensor in the undeformed configuration, and \mathcal{C} is the fourth order elasticity tensor.

For convenience, we can represent the stress and strain tensors in Equation (2.26) as vectors and the fourth order elasticity tensor as a matrix:

$$\begin{Bmatrix} S_{11} \\ S_{22} \\ S_{33} \\ S_{12} \\ S_{13} \\ S_{23} \end{Bmatrix} = d \begin{bmatrix} 1 & \frac{\nu}{1-\nu} & \frac{\nu}{1-\nu} & 0 & 0 & 0 \\ \frac{\nu}{1-\nu} & 1 & \frac{\nu}{1-\nu} & 0 & 0 & 0 \\ \frac{\nu}{1-\nu} & \frac{\nu}{1-\nu} & 1 & 0 & 0 & 0 \\ 0 & 0 & 0 & \frac{1-2\nu}{1-\nu} & 0 & 0 \\ 0 & 0 & 0 & 0 & \frac{1-2\nu}{1-\nu} & 0 \\ 0 & 0 & 0 & 0 & 0 & \frac{1-2\nu}{1-\nu} \end{bmatrix} \begin{Bmatrix} E_{11} \\ E_{22} \\ E_{33} \\ E_{12} \\ E_{13} \\ E_{23} \end{Bmatrix} \quad (2.27)$$

where d is a constant defined as

$$d = \frac{E(1-\nu)}{(1+\nu)(1-2\nu)} \quad (2.28)$$

and E is the Young's modulus and ν is the Poisson's ratio of the material.

Considering only two-dimensional cases, two possibilities exist to simplify the analysis. These are conditions of plane stress and plane strain. The plane stress condition exists when the body is very thin, i.e. in the limit where the third dimension approaches zero. Under such conditions Equation (2.27) simplifies to:

$$\begin{Bmatrix} S_{11} \\ S_{22} \\ S_{12} \end{Bmatrix} = \frac{E}{(1-\nu^2)} \begin{bmatrix} 1 & \nu & 0 \\ \nu & 1 & 0 \\ 0 & 0 & 1-\nu \end{bmatrix} \begin{Bmatrix} E_{11} \\ E_{22} \\ E_{12} \end{Bmatrix}. \quad (2.29)$$

The plane strain condition exists when the body is very thick, i.e. in the limit where the third dimension approaches infinity. Equation (2.27) now becomes:

$$\begin{Bmatrix} S_{11} \\ S_{22} \\ S_{12} \end{Bmatrix} = \frac{E(1+\nu)}{(1-2\nu)} \begin{bmatrix} 1-\nu & \nu & 0 \\ \nu & 1-\nu & 0 \\ 0 & 0 & 1-2\nu \end{bmatrix} \begin{Bmatrix} E_{11} \\ E_{22} \\ E_{12} \end{Bmatrix}. \quad (2.30)$$

As the second Piola-Kirchoff stress does not admit any physical interpretation in terms of stress tractions, it is more convenient to express the governing equations in terms of the first Piola-Kirchoff stress, \mathbf{P} , as shown in Equation (2.25). The first Piola-Kirchoff stress is then obtained by multiplying the second Piola-Kirchoff stress, \mathbf{S} , with the deformation gradient:

$$\mathbf{P} = \mathbf{F}\mathbf{S}. \quad (2.31)$$

Finally, to close the governing equations, the relationship between strain and the displacement field is given by

$$\mathbf{E} = \frac{1}{2}(\mathbf{H} + \mathbf{H}^T + \mathbf{H}^T\mathbf{H}), \quad (2.32)$$

where \mathbf{H} is the displacement gradient defined as

$$\mathbf{H} = \frac{d\mathbf{u}}{d\mathbf{X}}. \quad (2.33)$$

2.4 Boundary Conditions

For a unique solution to the governing equations, appropriate boundary conditions are to be prescribed. The boundary of the solid domain is split into two parts: \mathcal{A}_u where the displacement \mathbf{u}^p is prescribed, and \mathcal{A}_t where the surface traction \mathbf{t}_o^p is prescribed:

$$\mathbf{u} = \mathbf{u}^p \quad \text{on} \quad \mathcal{A}_u \quad (2.34)$$

$$\mathbf{P}\mathbf{n}_o = \mathbf{t}_o^p \quad \text{on} \quad \mathcal{A}_t \quad (2.35)$$

where \mathbf{n}_o is the outward pointing unit vector normal to the undeformed surface along which \mathbf{t}_o^p acts. This form of the traction, based in the undeformed configuration, may be related to its counterpart in the current configuration through force balance relations [49, 50] defined as

$$\mathbf{t}_o^p dS_o = \mathbf{t}^p dS \quad (2.36)$$

where dS_o and dS are infinitesimal surface area elements in the undeformed and deformed configurations respectively.

2.5 Conclusion

The set of equations governing a homogeneous isotropic geometrically non-linear elastic solid of volume \mathcal{V}_o in the undeformed configuration were described in this chapter. To summarise, the problem can be stated as follows:

Find the displacement \mathbf{u} such that it satisfies the equilibrium equation:

$$\text{Div}\mathbf{P} + \mathbf{b}_o = \rho_o \mathbf{a}$$

where the stress is related to the strain by

$$\mathbf{P} = \mathbf{F}\mathbf{S}$$

$$\mathbf{S} = \mathcal{C}\mathbf{E}$$

and the strain-displacement relationship is

$$\mathbf{E} = \frac{1}{2}(\mathbf{H} + \mathbf{H}^T + \mathbf{H}^T\mathbf{H})$$

$$\mathbf{H} = \frac{d\mathbf{u}}{d\mathbf{X}}$$

and with boundary conditions

$$\begin{aligned} \mathbf{u} &= \mathbf{u}^p & \text{on} & \mathcal{A}_u \\ \mathbf{P}\mathbf{n}_o &= \mathbf{t}_o^p & \text{on} & \mathcal{A}_t \end{aligned}$$

where the nomenclature is as defined in the preceding sections.

Chapter 3

Numerical Discretisation Procedures

3.1 Introduction

The equations presented in the previous chapter cannot be solved analytically in the generic case, necessitating numerical solution. To do so the equations first need to be discretised and placed in a form suitable for implementation into a computer program. The method of weighted residuals is to date the most popular approach, of which the finite element (FEM) and finite volume (FVM) methods are two popular sub-sets. In this chapter, the method of weighted residuals is discussed and the finite element and finite volume methods explored for solving the governing equations under consideration. Finally, temporal discretisation and solution procedure are presented.

3.2 Method of Weighted Residuals

The method of weighted residuals constitutes a modern numerical method by which to approximate solution of complex differential equations. In this method, a system of differential equations of the form

$$f(\mathbf{U}(x, t), x, t) = 0 \quad \forall \quad x \in d\mathcal{V}, t > 0 \quad (3.1)$$

with initial and boundary conditions, $\mathbf{U}(x, 0)$ and $f(\mathbf{U}(\mathcal{A}, t))$, are solved. In this equation, $\mathbf{U}(x, t)$ is a vector containing the dependent variables or unknowns to be solved for, \mathcal{V} is the spatial domain, \mathcal{A} is the boundary area and x and t are the independent spatial and temporal variables. The system is cast into integral or weak form and solved for in an approximate or weighted average sense as follows:

$$\int_{\mathcal{V}} \mathbf{w}(x) f(\bar{\mathbf{U}}(x, t), x, t) d\mathcal{V} = 0 \quad (3.2)$$

where $\mathbf{w}(x)$ is a weighting field and $\bar{\mathbf{U}}$ an approximate solution that satisfies Equation (3.2) as well as the initial and boundary conditions. The finite element and finite volume methods are sub-sets of the method of weighted residuals that differ in the choice of the weighting function.

In the finite element method, basis functions $\mathbf{N}(x)$ are used for construction of the approximate solution:

$$\bar{\mathbf{U}} = [\mathbf{N}]\{U\} \quad (3.3)$$

where $\{U\}$ is the set of n discrete unknowns to be solved for. Many different choices for the weighting function are possible, as almost any set of independent functions can be used. The most popular choice in finite elements is the Bubnov-Galerkin approach [21, 29], where the original basis or shape functions are used for weighting, i.e. $\mathbf{w}(x) = \mathbf{N}(x)$. The finite element method supports arbitrary accuracy via the appropriate selection of the basis functions. It is also applicable to unstructured grids (Figure 3.1), which makes it suitable for problems involving complex geometries.

The finite volume method results by choosing the weighting function in Equation (3.2) as unity:

$$\mathbf{w}(x) = 1 \quad \forall x \in d\mathcal{V}. \quad (3.4)$$

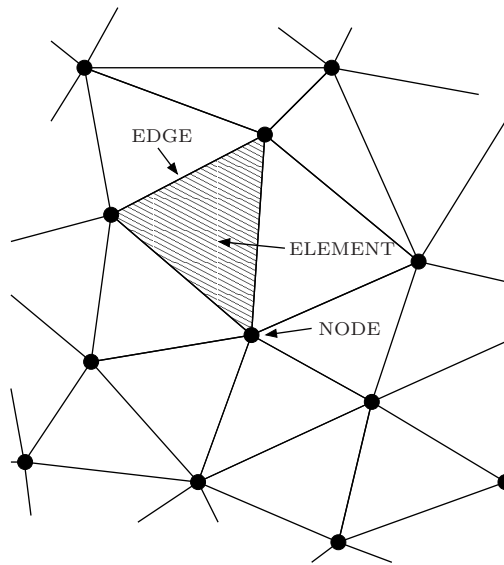


Figure 3.1: Schematic of the finite element method on a 2D unstructured mesh

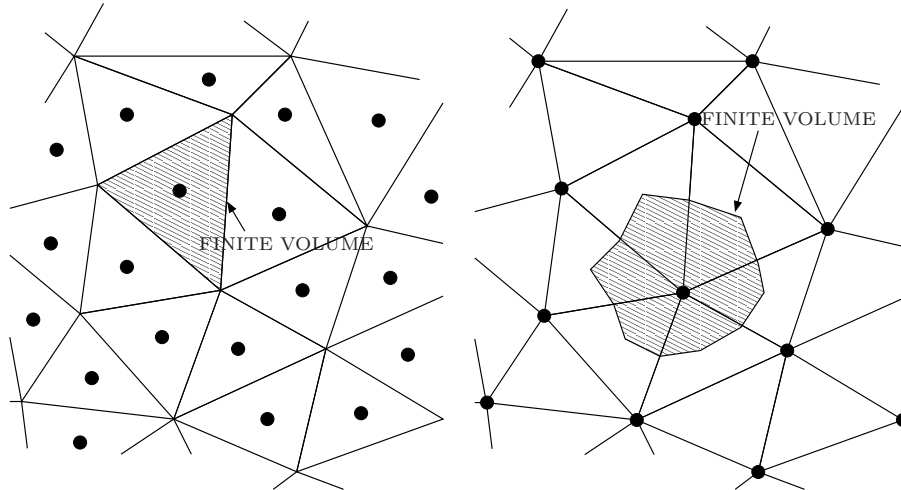


Figure 3.2: Two variants of the finite volume method on 2D unstructured grids: element-based or cell-centred (left) and node-based or vertex-centred (right)

Two procedures exist with the finite volume method viz. an element-based or cell-centred and node-based or vertex-centred approach (see Figure 3.2). In the cell-centred approach, the control volumes are taken as the elements of the original mesh and unknown variables are stored at element centres. In the vertex-centred case, control volumes are constructed by joining edge centres and element centres to form a dual mesh. The unknown variables are now stored at the nodes or vertices of the original mesh. The vertex-centred approach utilises edge-based data-structures and is preferred for this work due to its increased efficiency compared to element-based approaches [51,52], and it is also supported by *Elemental*.

3.3 FEM vs. FVM for Solid Mechanics

Since the 1960s, the finite element method [21] has mainly been used to discretise the governing equations of solid mechanics. Over the last two decades, however, the finite volume method [22] has received increasing attention. As a result, many studies have been conducted on the application of the finite volume method to linear elasticity [23–28]. It has also been extended to incompressible material deformation analysis [53,54] and problems involving material non-linearities [55,56]. Finite volume methods incorporating rotational degrees of freedom in addition to the displacement degrees of freedom have been presented in [30,54]. Aiming at fluid-structure interaction problems, [2, 11, 13, 35] have also made use of a finite volume technique for the discretisation of a linear elastic solid structure.

It is well known that the linear finite element formulation suffers from sensitivity to element aspect ratio or shear locking when subjected to bending [29]. Fallah [28] and Wheel [26] present a locking-free finite volume approximation to Mindlin-Reissner plates for both cell-centred and vertex-centred formulations. However, using solid elements, Wenke and Wheel [30] present results that do indicate shear locking with the displacement-based vertex-centred finite volume approach. Further, Oxtoby et al. [17] developed a displacement-based hybrid finite volume method that holds promise as being locking-free [20]. A more rigorous evaluation of the suitability of the finite volume method for modelling a structure under bending with varying element aspect ratios, is presented in this work.

When considering geometrically non-linear problems as seen in this work, Fallah et al. [31] presented a finite volume procedure and also compared the results with a finite element method. They concluded that for a low mesh density the difference between the finite volume and finite element methods are considerable, with the finite element method being more accurate, but by increasing the number of elements the accuracy of the two methods are comparable. On the other hand, Vaz Jr. et al. [32] state that the finite element formulation provides higher accuracy for displacement solutions. In this work, a rigorous comparison between the two methods will be made.

For structures under non-linear bending, it is known that at the least cubic displacement fields result. Therefore, higher-order methods are also considered in this work. The finite element Galerkin method uses shape functions as the weighting functions and may be easily extended to higher-order via higher-order polynomials for the shape functions [21]. The finite volume method results by choosing the weighting function as unity. To the author's knowledge no higher-order finite volume method for computational solid mechanics has been presented thus far. Such a formulation is therefore developed in this work.

3.4 Spatial Discretisation: Finite Element Method

The standard Galerkin finite element method of discretisation is described in this section. The strong form of the equilibrium equation written in terms of the undeformed configuration, Equation (2.25), in the absence of body forces is given by

$$\rho_o \mathbf{a} = \text{Div} \mathbf{P}. \quad (3.5)$$

The equation is cast into weak form based on the method of weighted residuals. This is done by first expressing the governing equation as a residual, \mathbf{R} , as follows

$$\mathbf{R} = \text{Div} \mathbf{P} - \rho_o \mathbf{a}. \quad (3.6)$$

The residual is then dotted with a weighting field, \mathbf{w} , and integrated over

the entire domain, \mathcal{V}_o , which renders the equation in weak form

$$\int_{\mathcal{V}_o} \mathbf{w} \cdot \mathbf{R} d\mathcal{V}_o = 0. \quad (3.7)$$

The weighting field, \mathbf{w} , is the set of all possible functions, with the restriction that $\mathbf{w} = \mathbf{0}$ along that part of the boundary of the domain where the displacement is prescribed, \mathcal{A}_u .

Expanding the terms in Equation (3.7) gives

$$\int_{\mathcal{V}_o} \mathbf{w} \cdot (\text{Div} \mathbf{P} - \rho_o \mathbf{a}) d\mathcal{V}_o = 0 \quad (3.8)$$

$$\int_{\mathcal{V}_o} \mathbf{w} \cdot \text{Div} \mathbf{P} d\mathcal{V}_o - \int_{\mathcal{V}_o} \rho_o \mathbf{w} \cdot \mathbf{a} d\mathcal{V}_o = 0. \quad (3.9)$$

Using the definition of the divergence of a second order tensor, as well as the product rule of differentiation, it can be shown [57] that

$$\text{Div}(\mathbf{P}^T \mathbf{w}) = \mathbf{w} \cdot \text{Div} \mathbf{P} + \mathbf{P} \cdot \frac{\partial \mathbf{w}}{\partial \mathbf{X}}. \quad (3.10)$$

Re-arranging and substituting Equation (3.10) in Equation (3.9) gives

$$\int_{\mathcal{V}_o} \left[\text{Div}(\mathbf{P}^T \mathbf{w}) d\mathcal{V}_o - \mathbf{P} \cdot \frac{\partial \mathbf{w}}{\partial \mathbf{X}} \right] d\mathcal{V}_o - \int_{\mathcal{V}_o} \rho_o \mathbf{w} \cdot \mathbf{a} d\mathcal{V}_o = 0 \quad (3.11)$$

$$\int_{\mathcal{V}_o} \text{Div}(\mathbf{P}^T \mathbf{w}) d\mathcal{V}_o - \int_{\mathcal{V}_o} \mathbf{P} \cdot \frac{\partial \mathbf{w}}{\partial \mathbf{X}} d\mathcal{V}_o - \int_{\mathcal{V}_o} \rho_o \mathbf{w} \cdot \mathbf{a} d\mathcal{V}_o = 0. \quad (3.12)$$

We now apply Gauss's Divergence Theorem to the first term on the left-hand-side of Equation (3.12):

$$\int_{\mathcal{A}_o} (\mathbf{P}^T \mathbf{w}) \cdot \mathbf{n}_o d\mathcal{A}_o - \int_{\mathcal{V}_o} \mathbf{P} \cdot \frac{\partial \mathbf{w}}{\partial \mathbf{X}} d\mathcal{V}_o - \int_{\mathcal{V}_o} \rho_o \mathbf{w} \cdot \mathbf{a} d\mathcal{V}_o = 0 \quad (3.13)$$

$$\int_{\mathcal{A}_o} (\mathbf{P} \mathbf{n}_o) \cdot \mathbf{w} d\mathcal{A}_o - \int_{\mathcal{V}_o} \mathbf{P} \cdot \frac{\partial \mathbf{w}}{\partial \mathbf{X}} d\mathcal{V}_o - \int_{\mathcal{V}_o} \rho_o \mathbf{w} \cdot \mathbf{a} d\mathcal{V}_o = 0, \quad (3.14)$$

where \mathcal{A}_o is the boundary surface enclosing \mathcal{V}_o and \mathbf{n}_o is the outward pointing unit normal vector.

But, $\mathbf{t}_o = \mathbf{P} \mathbf{n}_o$ [57], where \mathbf{t}_o denotes the surface traction expressed in the undeformed configuration, therefore

$$\int_{\mathcal{A}_o} \mathbf{t}_o \cdot \mathbf{w} d\mathcal{A}_o - \int_{\mathcal{V}_o} \mathbf{P} \cdot \frac{\partial \mathbf{w}}{\partial \mathbf{X}} d\mathcal{V}_o - \int_{\mathcal{V}_o} \rho_o \mathbf{w} \cdot \mathbf{a} d\mathcal{V}_o = 0. \quad (3.15)$$

Splitting up the boundary integral into two parts: \mathcal{A}_u where the displacement \mathbf{u}^p is prescribed and \mathcal{A}_t where the surface traction \mathbf{t}_o^p is prescribed gives

$$\int_{\mathcal{A}_t} \mathbf{t}_o \cdot \mathbf{w} d\mathcal{A}_o + \int_{\mathcal{A}_u} \mathbf{t}_o \cdot \mathbf{w} d\mathcal{A}_o - \int_{\mathcal{V}_o} \mathbf{P} \cdot \frac{\partial \mathbf{w}}{\partial \mathbf{X}} d\mathcal{V}_o - \int_{\mathcal{V}_o} \rho_o \mathbf{w} \cdot \mathbf{a} d\mathcal{V}_o = 0. \quad (3.16)$$

Equation (3.16) is now simplified by noting that $\mathbf{w} = \mathbf{0}$ along \mathcal{A}_u and along \mathcal{A}_t the traction is prescribed, therefore

$$\int_{\mathcal{A}_t} \mathbf{t}_o^p \cdot \mathbf{w} d\mathcal{A}_o - \int_{\mathcal{V}_o} \mathbf{P} \cdot \nabla_X \mathbf{w} d\mathcal{V}_o - \rho_o \int_{\mathcal{V}_o} \mathbf{w} \cdot \mathbf{a} d\mathcal{V}_o = 0. \quad (3.17)$$

Equation (3.17) represents the general weak form of the solid mechanics boundary value problem. There are two interesting facts to note about this equation. Firstly, the traction boundary condition now appears explicitly within the governing equation. Secondly, since we apply this boundary condition $\mathbf{P}\mathbf{n} = \mathbf{t}_o^p$ within the integral, this means that the boundary condition is only satisfied in weak form or in a weighted average sense.

Instead of solving for all possible set of weighting functions for \mathbf{w} to obtain an exact solution, we consider only a finite set of functions for \mathbf{w} . These functions are chosen as piecewise-continuous low-order polynomial functions defined on sub-domains (elements) within the total domain \mathcal{V}_o and are referred to as basis or shape functions $[N]$. The weighting field is now interpolated between nodal weighting values $\{W\}$ using these shape functions, i.e.

$$\mathbf{w} = [N] \{W\}. \quad (3.18)$$

The primary variable, viz. the displacement field \mathbf{u} , is interpolated over an element using the same shape functions:

$$\mathbf{u} = [N] \{U\}, \quad (3.19)$$

where $\{U\}$ is the vector containing the nodal displacements. Using the same shape functions for both the displacement and weighting field is referred to as the Bubnov-Galerkin method.

Substituting Equations (3.18) and (3.19) into Equation (3.17) and simplifying, noting that $\mathbf{a} = [N]\{\ddot{U}\}$, gives

$$\int_{\mathcal{A}_t} \mathbf{w}^T \mathbf{t}_o^p d\mathcal{A}_o - \int_{\mathcal{V}_o} (\nabla_X \mathbf{w})^T \mathbf{P} d\mathcal{V}_o = \rho_o \int_{\mathcal{V}_o} \mathbf{a}^T \mathbf{w} d\mathcal{V}_o \quad (3.20)$$

$$\int_{\mathcal{A}_t} \{W\}^T [N]^T \{\mathbf{t}_o^p\} d\mathcal{A}_o - \int_{\mathcal{V}_o} \{W\}^T [B]^T \{P\} d\mathcal{V}_o = \rho_o \int_{\mathcal{V}_o} \{W\}^T [N]^T [N] \{\ddot{U}\} d\mathcal{V}_o, \quad (3.21)$$

where $[B]$ is a matrix containing the derivatives of the shape functions and $\{P\}$ is a vector containing the first Piola-Kirchoff stress. The details of how this matrix is constructed is discussed in the next section.

Since $\{W\}$ is arbitrary and not equal to zero, Equation (3.21) can be simplified to:

$$\int_{\mathcal{A}_t} [N]^T \{\mathbf{t}_o^p\} d\mathcal{A}_o - \int_{\mathcal{V}_o} [B]^T \{P\} d\mathcal{V}_o = \rho_o \int_{\mathcal{V}_o} [N]^T [N] \{\ddot{U}\} d\mathcal{V}_o \quad (3.22)$$

where $\{\ddot{U}\}$ contains constant nodal values and can be removed from the integral.

The domain is discretised into a finite number of non-overlapping control volumes or element domains \mathcal{V}_e , which are defined in the undeformed configuration. Equation (3.22) is now expressed as the sum over all the elements within the domain:

$$\sum_e \int_{\mathcal{A}_e^c} [N]^T \{t_o^p\} d\mathcal{A}_o - \sum_e \int_{\mathcal{V}_e} [B]^T \{P\} d\mathcal{V}_o = \sum_e \rho_o \int_{\mathcal{V}_e} [N]^T [N] d\mathcal{V}_o \{\ddot{U}\}. \quad (3.23)$$

3.4.1 Q4 Finite Element Method

The bilinear quadrilateral or Q4 plane element is described in this section. In this form of the finite element method, the domain is discretised into four-noded isoparametric quadrilateral elements. Figure 3.3 (left) shows an actual Q4 element in physical space. With the isoparametric formulation, the same shape functions used to interpolate displacements are also used for interpolating the geometry. Therefore, isoparametric elements need not be restricted to rectangular shapes, making it suitable to be used to mesh complicated geometries.

To facilitate the isoparametric formulation the element is mapped or transformed into a reference element. As shown in Figure 3.3 (right), this is done using reference or natural coordinates ξ and η . The sides of the reference element intersect the ξ and η axes at $\xi = \pm 1$ and $\eta = \pm 1$, thus making the reference element a square of two units width on either side. The point $\xi = \eta = 0$ is the centre of the element.

The Q4 element can only accommodate bilinear polynomials as shape functions. These shape functions can be derived intuitively by noting that for any shape function N_i , $N_i = 1$ at node i and $N_i = 0$ at every other node. Following this approach, the Q4 shape functions are:

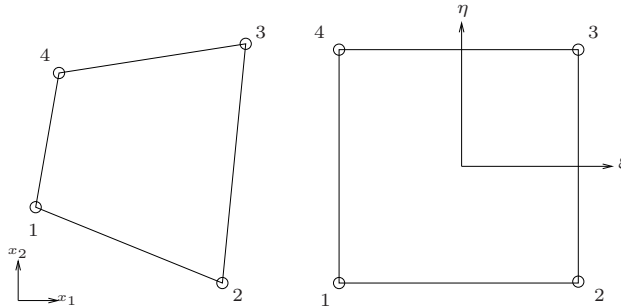


Figure 3.3: Isoparametric Q4 element in physical space (left) and reference space (right)

$$\begin{aligned} N_1 &= \frac{1}{4}(1 - \xi)(1 - \eta) & N_2 &= \frac{1}{4}(1 + \xi)(1 - \eta) \\ N_3 &= \frac{1}{4}(1 + \xi)(1 + \eta) & N_4 &= \frac{1}{4}(1 - \xi)(1 + \eta) \end{aligned} \quad (3.24)$$

The displacements can now be expressed as

$$\begin{Bmatrix} u_1 \\ u_2 \end{Bmatrix} = \begin{Bmatrix} N_1 U_{1_1} + N_2 U_{1_2} + N_3 U_{1_3} + N_4 U_{1_4} \\ N_1 U_{2_1} + N_2 U_{2_2} + N_3 U_{2_3} + N_4 U_{2_4} \end{Bmatrix} \quad (3.25)$$

$$\begin{Bmatrix} u_1 \\ u_2 \end{Bmatrix} = \begin{bmatrix} N_1 & 0 & N_2 & 0 & N_3 & 0 & N_4 & 0 \\ 0 & N_1 & 0 & N_2 & 0 & N_3 & 0 & N_4 \end{bmatrix} \begin{Bmatrix} U_{1_1} \\ U_{2_1} \\ U_{1_2} \\ U_{2_2} \\ U_{1_3} \\ U_{2_3} \\ U_{1_4} \\ U_{2_4} \end{Bmatrix} \quad (3.26)$$

$$\mathbf{u} = [N] \{U\}. \quad (3.27)$$

Referring back to the discrete equation, Equation (3.23), matrix $[B]$ still has to be computed. To compute $[B]$, we require the derivatives of the shape functions $N_i(\xi, \eta)$ with respect to the physical coordinates X_1 and X_2 , i.e. $\frac{\partial N_i}{\partial X_1}$ and $\frac{\partial N_i}{\partial X_2}$. To do this, we make use of the isoparametric formulation to relate (X_1, X_2) to (ξ, η) , i.e. the same interpolation functions are used for the geometry as that for the displacements, therefore

$$\begin{Bmatrix} X_1 \\ X_2 \end{Bmatrix} = \begin{Bmatrix} N_1 X_{1_1} + N_2 X_{1_2} + N_3 X_{1_3} + N_4 X_{1_4} \\ N_1 X_{2_1} + N_2 X_{2_2} + N_3 X_{2_3} + N_4 X_{2_4} \end{Bmatrix} \quad (3.28)$$

or

$$\mathbf{X} = [N] \{X\}. \quad (3.29)$$

Now, using the chain rule of differentiation, the derivatives of the shape functions can be expressed as

$$\frac{\partial N_i}{\partial \xi} = \frac{\partial N_i}{\partial X_1} \frac{\partial X_1}{\partial \xi} + \frac{\partial N_i}{\partial X_2} \frac{\partial X_2}{\partial \xi} \quad (3.30)$$

$$\frac{\partial N_i}{\partial \eta} = \frac{\partial N_i}{\partial X_1} \frac{\partial X_1}{\partial \eta} + \frac{\partial N_i}{\partial X_2} \frac{\partial X_2}{\partial \eta}. \quad (3.31)$$

Therefore,

$$\begin{Bmatrix} \frac{\partial N_i}{\partial \xi} \\ \frac{\partial N_i}{\partial \eta} \end{Bmatrix} = \begin{bmatrix} \frac{\partial X_1}{\partial \xi} & \frac{\partial X_2}{\partial \xi} \\ \frac{\partial X_1}{\partial \eta} & \frac{\partial X_2}{\partial \eta} \end{bmatrix} \begin{Bmatrix} \frac{\partial N_i}{\partial X_1} \\ \frac{\partial N_i}{\partial X_2} \end{Bmatrix} \quad (3.32)$$

$$\begin{Bmatrix} \frac{\partial N_i}{\partial \xi} \\ \frac{\partial N_i}{\partial \eta} \end{Bmatrix} = [\mathbf{J}] \begin{Bmatrix} \frac{\partial N_i}{\partial X_1} \\ \frac{\partial N_i}{\partial X_2} \end{Bmatrix}, \quad (3.33)$$

where $[\mathbf{J}]$ is called the Jacobian matrix and is computed using Equation (3.28) and (3.24).

The required derivatives for the matrix $[B]$ are now computed using the inverse of the Jacobian matrix

$$\begin{Bmatrix} \frac{\partial N_i}{\partial X_1} \\ \frac{\partial N_i}{\partial X_2} \end{Bmatrix} = [\mathbf{J}]^{-1} \begin{Bmatrix} \frac{\partial N_i}{\partial \xi} \\ \frac{\partial N_i}{\partial \eta} \end{Bmatrix}. \quad (3.34)$$

Equation (3.23) now reads

$$\sum_e \{F_{\text{ext}}\} - \sum_e \left(\int_{-1}^1 \int_{-1}^1 [B]^T \{P\} \det(\mathbf{J}) d\xi d\eta \right) = \sum_e \rho_o \int_{\mathcal{V}_e} [N]^T [N] d\mathcal{V}_o \{\dot{U}\}, \quad (3.35)$$

where the external loads are simply denoted as $\{F_{\text{ext}}\}$ and $\det(\mathbf{J})$ is the determinant of the Jacobian matrix and is used to transform the integral in the physical coordinates to that in the reference coordinates.

Finally, the double spatial integral in Equation (3.35) is computed numerically using Gauss quadrature, i.e. the integral is evaluated at a specific number of Gauss points, the result is then multiplied by a weighting factor W_{GP} and the results summed over all the Gauss points

$$\sum_e \{F_{\text{ext}}\} - \sum_e \left(\sum_{\text{Gauss pts}} [B]^T \{P\} \det(\mathbf{J}) W_{GP} \right) = \sum_e \rho_o \int_{\mathcal{V}_e} [N]^T [N] d\mathcal{V}_o \{\ddot{U}\}. \quad (3.36)$$

The temporal term on the right-hand-side of the equation is discretised using a dual-timestepping procedure and is discussed later.

3.4.2 Q8 Finite Element Method

The Q4 element, described in the previous section, is limited to linear shape functions within each element. Use of higher-order interpolation may lead to far more accurate results. For thin structures under non-linear bending as seen in this work, higher-order displacement fields result. As we would like to use as few elements through the thickness as possible, higher-order methods will be considered. The Q8 finite element formulation is a direct extension of the Q4 approach discussed above. The eight-noded quadrilateral or Q8 element is obtained by adding a mid-node to each side of the Q4 element. These mid-nodes allow the Q8 element to even have curved sides. Figure 3.4 (left) shows a Q8 element in the physical space and in the reference space (right).

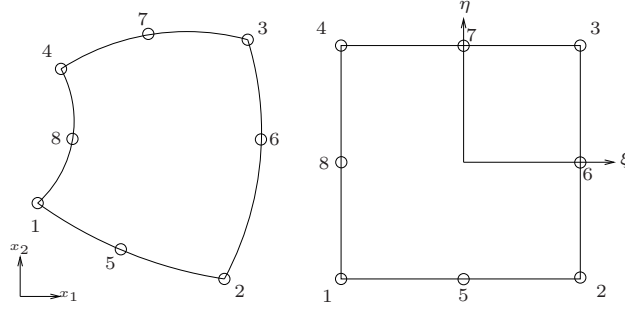


Figure 3.4: Isoparametric Q8 element in physical space (left) and reference space (right)

The shape functions for the Q8 element contain higher-order quadratic terms:

$$\begin{aligned}
 N_1 &= -0.25(1 - \xi)(1 - \eta)(1 + \xi + \eta) & N_5 &= 0.5(1 - \xi^2)(1 - \eta) \\
 N_2 &= -0.25(1 + \xi)(1 - \eta)(1 - \xi + \eta) & N_6 &= 0.5(1 + \xi)(1 - \eta^2) \\
 N_3 &= -0.25(1 + \xi)(1 + \eta)(1 - \xi - \eta) & N_7 &= 0.5(1 - \xi^2)(1 + \eta) \\
 N_4 &= -0.25(1 - \xi)(1 + \eta)(1 + \xi - \eta) & N_8 &= 0.5(1 - \xi)(1 - \eta^2),
 \end{aligned} \tag{3.37}$$

which are then implemented directly into Equation (3.36).

3.5 Spatial Discretisation: Finite Volume Method

At the commencement of this study, *Elemental* supported the finite volume framework. In this section, we now describe the finite volume method of discretising the equations governing solid mechanics. Two variants thereof, the standard vertex-centred approach and the hybrid finite volume approach, both supported by *Elemental*, are implemented. We then extend the finite volume method to a higher-order accurate formulation.

Consider again the equilibrium equation, Equation (2.25):

$$\rho_o \mathbf{a} = \text{Div} \mathbf{P} + \mathbf{b}_o. \tag{3.38}$$

For the purposes of discretisation, the equation above is re-written in indicial notation as

$$\rho_o a_i = \frac{\partial P_{iJ}}{\partial X_J} + b_I^o. \tag{3.39}$$

Assuming the body forces, b_I^o , to be negligible and expressing the acceleration, a_i , as the rate of change of velocity, v_i , gives

$$\rho_o \frac{\partial v_i}{\partial t} = \frac{\partial P_{iJ}}{\partial X_J}. \quad (3.40)$$

As per the finite element method, discretisation commences by casting the equation into integral or weak form by integrating over an arbitrary spatial subdomain \mathcal{V}_m in the reference (undeformed) configuration:

$$\int_{\mathcal{V}_m} \rho_o \frac{\partial v_i}{\partial t} d\mathcal{V}_o = \int_{\mathcal{V}_m} \frac{\partial P_{iJ}}{\partial X_J} d\mathcal{V}_o. \quad (3.41)$$

The control volume, \mathcal{V}_m , is fixed in time, therefore differentiation and integration of the temporal term are interchangeable. In addition, ρ_o is constant, so the left-hand-side of the equation simplifies to

$$\rho_o \frac{d}{dt} \int_{\mathcal{V}_m} v_i d\mathcal{V}_o = \int_{\mathcal{V}_m} \frac{\partial P_{iJ}}{\partial X_J} d\mathcal{V}_o. \quad (3.42)$$

Applying the Divergence Theorem of Gauss, the spatial derivative may be written in terms of fluxes as:

$$\rho_o \frac{d}{dt} \int_{\mathcal{V}_m} v_i d\mathcal{V}_o = \oint_{\mathcal{A}_m} P_{iJ} \cdot n_J d\mathcal{A}_o \quad (3.43)$$

where \mathcal{A}_m is the surface enclosing \mathcal{V}_m and $\mathbf{n} = (n_1, n_2)$ is the outward pointing unit-vector normal to \mathcal{A}_m .

3.5.1 Vertex-centred Finite Volume Method

A vertex-centred finite volume approach utilising edge-based data-structures was selected over an element-based approach for use in *Elemental*, due to its increased computational efficiency [51, 52] and suitability for computation on distributed memory parallel hardware architectures. In the edge-based vertex-centred method, the dependent variables are stored at nodes around which control volumes are constructed. In 2D, these control volumes are constructed by joining the midpoints of edges with element centroids and in such a way that only one node lies within each control volume. The set of surfaces forming the control volumes are referred to as a dual-mesh. This is shown schematically for a node m in Figure 3.5 [15]. In the figure, \mathcal{V}_m is the control volume associated with node m . Its bounding surface \mathcal{A}_m is composed of a number of surfaces which are defined based on their associated edges. For example, \mathcal{A}_{mn} is the surface segment intersecting the edge Υ_{mn} which connects nodes m and n .

The surface integrals in Equation (3.43) are now calculated in an edge-wise manner, i.e. the surface integral is expressed as the sum over all the edges connecting the control volume

$$\rho_o \frac{d}{dt} \int_{\mathcal{V}_m} v_i d\mathcal{V}_o = \sum_{\Upsilon_{mn} \cap \mathcal{V}_m} P_{iJ} \cdot C_{J:mn}, \quad (3.44)$$

where C_{mn} is the edge-coefficient for an internal edge Υ_{mn} . An edge-coefficient is defined as the area of the bounding surface of a particular edge in a control volume multiplied by the outward pointing unit-vector normal to its face; therefore

$$C_{J:mn} = \sum_{\mathcal{A}_{mn_t} \in \mathcal{A}_{mn}} n_{J:mn_t} \mathcal{A}_{mn_t} \quad (3.45)$$

where \mathcal{A}_{mn_t} is a segment of the surface \mathcal{A}_{mn} and $n_{J:mn_t}$ is the unit-vector normal to \mathcal{A}_{mn_t} . For the edge Υ_{mn} shown in Figure 3.5, the edge-coefficient is comprised of two surfaces $t = 1$ and $t = 2$.

The surfaces of some control volumes of the dual-mesh may lie on the boundary of the domain, denoted by \mathcal{A}_{m_B} in Figure 3.5.

Equation (3.44) is therefore updated to include the domain boundary edges

$$\rho_o \frac{d}{dt} \int_{\mathcal{V}_m} v_i d\mathcal{V}_o = \sum_{\Upsilon_{mn} \cap \mathcal{V}_m} P_{iJ} \cdot C_{J:mn} + \sum_{\Upsilon_{mn}^B \cap \mathcal{V}_m} P_{iJ} \cdot B_{J:mn}. \quad (3.46)$$

Boundary edge-coefficients are computed in a similar way to their internal edge counterparts:

$$B_{J:mn} = \sum_{\mathcal{A}_{mn_{Bt}} \in \mathcal{A}_{mn_B}} n_{J:mn_{Bt}} \mathcal{A}_{mn_{Bt}} \quad (3.47)$$

where $n_{J:mn_{Bq}}$ is the outward pointing unit-vector normal to the boundary surface segment $\mathcal{A}_{mn_{Bq}}$. For the case shown in Figure 3.5, Υ_{mp} is a boundary edge

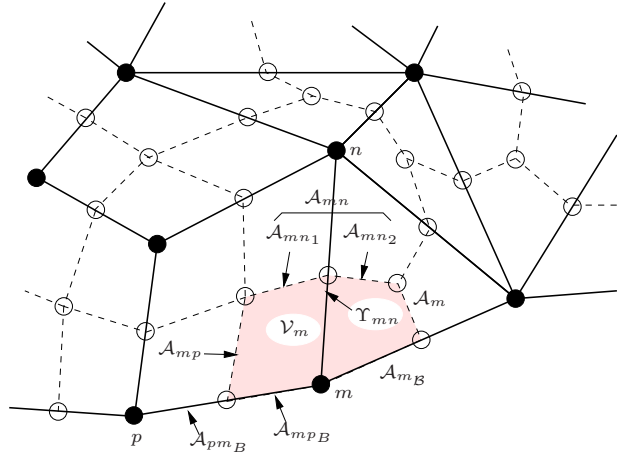


Figure 3.5: Schematic of the construction of a dual-mesh

and \mathcal{A}_{mpB} is the domain boundary surface associated with this edge. Therefore, for a 2D domain as above, t is always equal to 1 in Equation (3.47).

Displacement gradients are evaluated numerically at the nodes or vertices. Therefore, referring to Figure 3.5 and following from Gauss's divergence theorem, the displacement gradients for node m are given by:

$$\left. \frac{\partial u_i}{\partial X_J} \right|_m = \frac{1}{V_m} \oint_{\mathcal{A}_m} u_i \cdot n_J d\mathcal{A}_m = \frac{1}{V_m} \sum_{\Upsilon_{mn} \cap \mathcal{V}_m} \left(u_{i:mn} \cdot C_{J:mn} \right) \quad (3.48)$$

where $u_{i:mn}$ is the linearly-interpolated displacement at the face:

$$u_{i:mn} \approx \frac{1}{2}(u_{i:m} + u_{i:n}). \quad (3.49)$$

In the edge-based procedure, the stresses are calculated at the faces of the dual-cells using a compact stencil [58, 59]. The displacement gradients at the faces are therefore given by:

$$\left. \frac{\partial u_i}{\partial X_J} \right|_{mn} \approx \frac{u_{i:n} - u_{i:m}}{|\bar{l}|} \frac{l_j}{|\bar{l}|} + \frac{1}{2} \left(\left. \frac{\partial u_i}{\partial X_J} \right|_m + \left. \frac{\partial u_i}{\partial X_J} \right|_n \right) \Big|_{\text{normal}} \quad (3.50)$$

where \bar{l} is the edge-length and $|_{\text{normal}}$ indicates the component in the direction normal to the edge.

The strains evaluated using Equations (2.32) and (2.33) and these displacement gradients are referred to as node-based strains. Finally, the stresses, required to evaluate the integrals in Equation (3.46), are computed using Equations (2.26) and (2.31).

3.5.2 Hybrid Finite Volume Method

In the vertex-centred finite volume method described above, displacement gradients are evaluated at the nodes or vertices. This is different to the conventional finite element method, where stresses are evaluated at integration points within the element [29]. An alternative to the finite volume method just described where displacement gradients are evaluated at element centres, as proposed in [14], is considered. This is equivalent to the finite element method with one integration point.

Referring to Figure 3.6, the displacement gradients for element M are given by:

$$\left. \frac{\partial u_i}{\partial X_J} \right|_M = \frac{1}{V_M} \sum_{\Upsilon_M \cap \mathcal{V}_M} \left(u_{i:MN} \cdot n_{J:MN} \mathcal{A}_{MN} \right) \quad (3.51)$$

where \mathcal{A}_{MN} is the surface segment between elements M and N and $u_{i:MN}$ is the linearly-interpolated displacement of this surface (note that in 2D $u_{i:mn}$ and $u_{i:MN}$ are identical):

$$u_{i:MN} \approx \frac{1}{2}(u_{i:m} + u_{i:n}). \quad (3.52)$$

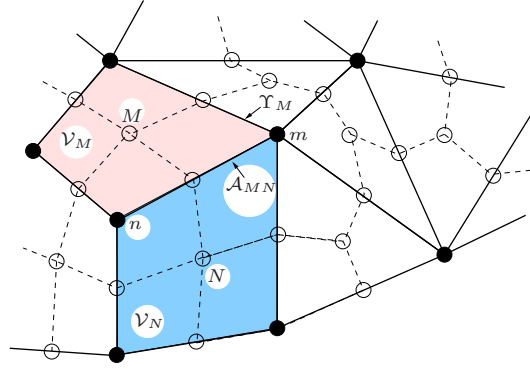


Figure 3.6: Schematic of a mesh showing the calculation of element-based gradients

The displacement gradients at the faces are obtained by averaging their values between the two connecting elements:

$$\frac{\partial u_i}{\partial X_J} \Big|_{mn} \approx \frac{1}{2} \left(\frac{\partial u_i}{\partial X_J} \Big|_M + \frac{\partial u_i}{\partial X_J} \Big|_N \right). \quad (3.53)$$

The strains evaluated using these displacement gradients are referred to as element-based strains.

A finite volume approach using only element-based strains suffers from odd-even decoupling as displacements appear only in the combination $(u_{i:m} + u_{i:n})$. A hybrid finite volume method to remedy the odd-even decoupling was proposed in [17, 20]. This method uses element-based strains for the shear components, but node-based strains for the normal components. Therefore, Equation (3.53) is used for the displacement gradients in E_{ij} with $i \neq j$ and Equation (3.50) in E_{ij} with $i = j$. This is similar to the selective integration approach [29] used in the finite element method to eliminate spurious modes, where different Gauss quadrature integration rules are used for the shear and normal strain contributions to the stiffness matrix.

Consequently, both the vertex-centred FVM, which uses only node-based strains, and the hybrid FVM, which uses a combination of node- and element-based strains, were implemented in this work.

3.5.3 Proposed Higher-Order Finite Volume Method

As discussed above, higher-order methods are common with the finite element method by using higher-order polynomials for the shape functions. However, with the finite volume method the weighting function is set equal to unity and the same approach to develop a higher-order finite volume method cannot be used. Instead, an error analysis is conducted on the vertex-centred and hy-

brid finite volume formulations and using this information, a higher-order finite volume formulation is then developed.

Error Analysis: Analytical Approach

In this section, a detailed error analysis is conducted analytically on both the vertex-centred and hybrid finite volume formulations (the detailed derivations are included in Appendix A). To simplify the error analysis, we limit the problem to the small displacement case. Consider again the governing equation, Equation (2.25):

$$\rho a_i = \frac{\partial \sigma_{ij}}{\partial x_j} + b_i \quad (3.54)$$

where σ_{ij} is the stress. Note that in the small displacement case the Cauchy and Piola-Kirchoff stress are identical and will simply be denoted by σ_{ij} .

Since we are only interested in the spatial accuracy, we neglect the temporal term and consider only the steady-state problem, i.e. $a_i = 0$. With body forces, b_i , negligible, the equation simplifies to:

$$\frac{\partial \sigma_{ij}}{\partial x_j} = 0. \quad (3.55)$$

Numerical error is introduced by discretisation, which can be expressed by:

$$\sum_{\Upsilon_{mn} \cap \mathcal{V}_m} \sigma_{ij} \cdot C_{j:mn} + \sum_{\Upsilon_{mn}^B \cap \mathcal{V}_m} \sigma_{ij} \cdot B_{j:mn} = \left. \frac{\partial \sigma_{ij}}{\partial x_j} \right|_m + \text{Error}_{i:m}. \quad (3.56)$$

The exact form of this $\text{Error}_{i:m}$ term may be determined analytically. Assuming a Poisson's ratio of zero, which simplifies the mathematical analysis by eliminating the effect of a loading in the perpendicular or transverse direction yet still provides a qualitative representation of the error terms, the stress-strain relationship, Equation (2.26), simplifies to:

$$\sigma_{ij} = E \varepsilon_{ij}. \quad (3.57)$$

The strain-displacement relationship for the small displacement case is:

$$\varepsilon_{ij} = \frac{1}{2} \left(\frac{\partial u_i}{\partial x_j} + \frac{\partial u_j}{\partial x_i} \right). \quad (3.58)$$

Substituting Equation (3.57) and Equation (3.58) into Equation (3.56) gives an equation expressed in terms of displacements, from which the numerical errors can be determined.

In this work only structured equi-spaced meshes are considered for the solid, which further simplifies the analysis. Consider first the standard vertex-centred formulation for the case of an internal node (Figure 3.7(a)). Substituting the expressions for the displacement gradients, Equation (3.50), and expanding each term using Taylor series expansions about the node, the discrete expression for

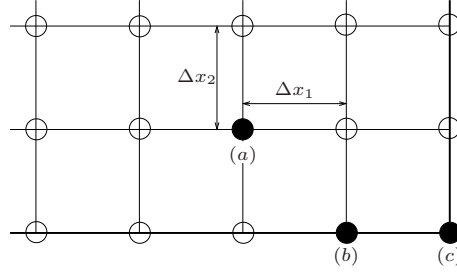


Figure 3.7: Schematic of the mesh indicating an internal, boundary and corner node

the leading error-term at an internal node (see Appendix A for the details of this derivation) is given by:

$$\text{Error}_i = \frac{E}{2} \left(\frac{1}{6} \frac{\partial^4 u_i}{\partial x_i^4} \Delta x_i^2 + \frac{1}{12} \frac{\partial^4 u_i}{\partial x_k^4} \Delta x_k^2 + \frac{1}{6} \frac{\partial^4 u_k}{\partial x_i^3 \partial x_k} \Delta x_i^2 + \frac{1}{6} \frac{\partial^4 u_k}{\partial x_i \partial x_k^3} \Delta x_k^2 \right) \quad (3.59)$$

with

$$\begin{aligned} i = 1; k = 2 & \quad \text{for the } x_1\text{-momentum equation} \\ i = 2; k = 1 & \quad \text{for the } x_2\text{-momentum equation.} \end{aligned}$$

Similarly, for a boundary node (Figure 3.7(b)) the leading-order error terms for the tangential and normal components of the momentum equations, respectively, are (see Appendix A for the detailed derivation):

$$\text{Error}_t = \frac{E}{2} \left(\frac{1}{6} \frac{\partial^4 u_t}{\partial x_t^4} \Delta x_t^2 + \frac{1}{3} \frac{\partial^3 u_t}{\partial x_n^3} \Delta x_n + (-1)^p \frac{1}{2} \frac{\partial^3 u_n}{\partial x_t \partial x_n^2} \Delta x_n + (-1)^p \frac{1}{3} \frac{\partial^3 u_n}{\partial x_t^3} \frac{\Delta x_t^2}{\Delta x_n} \right) \quad (3.60)$$

$$\text{Error}_n = \frac{E}{2} \left((-1)^p \frac{1}{2} \frac{\partial^3 u_t}{\partial x_t \partial x_n^2} \Delta x_n \right) \quad (3.61)$$

where subscripts n and t denote coordinates normal and tangential to the boundary respectively, $p = 1$ for the top and right boundaries and $p = 2$ for the bottom and left boundaries.

Finally, for a corner node (Figure 3.7(c)) the leading-order error term is (see Appendix A for the detailed derivation):

$$\text{Error}_i = \frac{E}{2} \left((-1)^p \frac{\partial^2 u_k}{\partial x_i^2} \frac{\Delta x_i}{\Delta x_k} \right) \quad (3.62)$$

with

$$\begin{aligned}
 i = 1; k = 2 & \quad \text{for the } x_1\text{-momentum equation} \\
 i = 2; k = 1 & \quad \text{for the } x_2\text{-momentum equation} \\
 p = 1 & \quad \text{for the top-left and bottom-right corners} \\
 p = 2 & \quad \text{for the top-right and bottom-left corners.}
 \end{aligned}$$

Two important conclusions can be derived from the leading-order error terms for the standard vertex-centred formulation above. Firstly, the truncation error is of order $O(\Delta x_i^2) + O(\Delta x_k^2)$ at internal nodes, $O(\Delta x_n) + O(\frac{\Delta x_t^2}{\Delta x_n})$ at boundary nodes and $O(\frac{\Delta x_i}{\Delta x_k})$ at corner nodes. Therefore, second-order rate of convergence is expected for internal nodes but only first-order for boundary nodes and zero-order for corner nodes. In addition, since the coefficients of the leading-order error terms at internal nodes are fourth-order derivatives, the formulation will be exact at internal nodes for a displacement field described by a cubic polynomial. However, at boundary nodes the formulation can only represent quadratic fields exactly and similarly only linear fields at corner nodes.

Using the same approach for the hybrid formulation, but substituting Equation (3.53) for the displacement gradients in E_{ij} with $i \neq j$ and Equation (3.50) in E_{ij} with $i = j$, the leading-order error term at the internal node (Figure 3.7(a)) is (see Appendix A for the detailed derivation):

$$\begin{aligned}
 \text{Error}_i = \frac{E}{2} \left(\frac{1}{6} \frac{\partial^4 u_i}{\partial x_i^4} \Delta x_i^2 + \frac{1}{12} \frac{\partial^4 u_i}{\partial x_k^4} \Delta x_k^2 + \frac{1}{6} \frac{\partial^4 u_k}{\partial x_i^2 \partial x_k} \Delta x_i^2 + \right. \\
 \left. \frac{1}{6} \frac{\partial^4 u_k}{\partial x_i \partial x_k^3} \Delta x_k^2 + \frac{1}{4} \frac{\partial^4 u_i}{\partial x_i^2 \partial x_k^2} \Delta x_i^2 \right) \quad (3.63)
 \end{aligned}$$

where the nomenclature is as previously defined.

For a boundary node (Figure 3.7(b)) (see Appendix A for the detailed derivation):

$$\begin{aligned}
 \text{Error}_t = \frac{E}{2} \left(\frac{1}{6} \frac{\partial^4 u_t}{\partial x_t^4} \Delta x_t^2 + \frac{1}{3} \frac{\partial^3 u_t}{\partial x_n^3} \Delta x_n + (-1)^p \frac{1}{2} \frac{\partial^3 u_n}{\partial x_t \partial x_n^2} \Delta x_n + \right. \\
 \left. (-1)^p \frac{1}{3} \frac{\partial^3 u_n}{\partial x_i^3} \frac{\Delta x_i^2}{\Delta x_n} + (-1)^q \frac{\partial^3 u_t}{\partial x_t^2 \partial x_n} \frac{\Delta x_t^2}{\Delta x_n} \right) \quad (3.64)
 \end{aligned}$$

$$\text{Error}_n = \frac{E}{2} \left((-1)^p \frac{1}{2} \frac{\partial^3 u_t}{\partial x_t \partial x_n^2} \Delta x_n + (-1)^q \frac{1}{2} \frac{\partial^3 u_n}{\partial x_t^2 \partial x_n} \Delta x_n \right) \quad (3.65)$$

where $q = 1$ for the left and right boundaries and $q = 2$ for the bottom and left boundaries and the rest of the symbols are as previously defined.

Finally, for a corner node (Figure 3.7(c)) the leading-order error term is (see Appendix A for the detailed derivation):

$$\text{Error}_i = \frac{E}{2} \left((-1)^p \frac{\partial^2 u_k}{\partial x_i^2} \frac{\Delta x_i}{\Delta x_k} - \frac{\partial^2 u_i}{\partial x_i \partial x_k} \frac{\Delta x_i}{\Delta x_k} \right). \quad (3.66)$$

	Vertex-centred FVM		Hybrid FVM	
Internal node	$O(\Delta x_i^2) + O(\Delta x_k^2)$	2nd-order	$O(\Delta x_i^2) + O(\Delta x_k^2)$	2nd-order
Boundary node	$O(\Delta x_n) + O(\frac{\Delta x_i^2}{\Delta x_n})$	1st-order	$O(\Delta x_n) + O(\frac{\Delta x_i^2}{\Delta x_n})$	1st-order
Corner node	$O(\frac{\Delta x_i}{\Delta x_k})$	zero-order	$O(\frac{\Delta x_i}{\Delta x_k})$	zero-order

Table 3.1: Order of accuracy of the vertex-centred and hybrid formulations

The truncation errors of the hybrid formulation are compared with that of the vertex-centred formulation in Table 3.1. As can be seen in the table, these errors are of the same order for both formulations. Furthermore, based on the coefficients of the leading-order error terms, the hybrid formulation indicates the same order of accuracy as that of the vertex-centred formulation. However, additional terms are present in the error expressions for the hybrid formulation that may cancel out for specific displacement fields. These will be analysed on specific test-cases in Chapter 4.

Higher-Order Finite Volume Method

In the previous section, it was shown that both the vertex-centred and hybrid finite volume formulations can represent cubic displacement fields exactly at internal nodes. However, only quadratic and linear fields are exact at boundary and corner nodes respectively. For thin structures under linear bending, it is known that at the least cubic displacement fields result. In this section, we develop a higher-order finite volume formulation for the small displacement case that does not suffer from a deterioration in accuracy along the boundaries, i.e. it can represent a third-order displacement field exactly at internal as well as boundary and corner nodes.

With the standard finite volume method the displacement gradients are computed in an edge-based manner (see Appendix A for details). A first attempt at developing a higher-order method involved computing these displacement gradients using third-order approximations. However, with the edge-based procedure the derivatives of stress in the momentum equations are computed using an equivalent forward-difference method at boundary nodes, as opposed to a central-difference method at internal nodes, hence the formulation always remains first-order accurate. Therefore, an approach that uses the traction boundary condition explicitly to solve for the displacements along the boundaries was used.

The traction boundary condition is stated as:

$$\boldsymbol{\sigma} \mathbf{n} = \mathbf{t}^p \quad (3.67)$$

or in indicial notation in terms of force:

$$F_i = \sigma_{ij} C_{j:mn} \quad (3.68)$$

where the nomenclature is as previously defined.

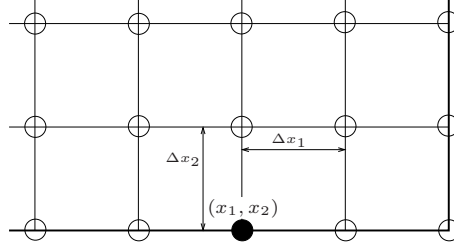


Figure 3.8: Schematic of the mesh indicating a boundary node

Consider a node along a boundary at the bottom of the beam as shown in Figure 3.8.

Expanding Equation (3.68) for this node gives:

$$F_1 = \sigma_{11}(\mathcal{A}n_1) + \sigma_{12}(\mathcal{A}n_2) = 0 \quad (3.69)$$

and

$$F_2 = \sigma_{21}(\mathcal{A}n_1) + \sigma_{22}(\mathcal{A}n_2) = 0 \quad (3.70)$$

with

$$(n_1, n_2) = (0, -1). \quad (3.71)$$

Substituting the stress-strain and strain-displacement relationships gives two equations from which the two displacements at the boundary node are solved:

$$\left. \frac{\partial u_1}{\partial x_2} \right|_{(x_1, x_2)} + \left. \frac{\partial u_2}{\partial x_1} \right|_{(x_1, x_2)} = 0 \quad (3.72)$$

$$\left. \frac{\partial u_2}{\partial x_2} \right|_{(x_1, x_2)} = 0. \quad (3.73)$$

Now, the displacement gradients above are discretised using third-order approximations, e.g. (see Appendix B for details of this derivation):

$$\left. \frac{\partial u_1}{\partial x_2} \right|_{(x_1, x_2)} \approx \frac{-11u_1(x_1, x_2) + 18u_1(x_1, x_2 + \Delta x_2) - 9u_1(x_1, x_2 + 2\Delta x_2) + 2u_1(x_1, x_2 + 3\Delta x_2)}{6\Delta x_2} \quad (3.74)$$

where it can be shown that the leading-order error term for this approximation is:

$$\text{Error} = -\frac{1}{4} \frac{\partial^4 u_1}{\partial x_2^4} \Delta x_2^3. \quad (3.75)$$

Therefore, this approximation is third-order accurate. Similarly:

$$\left. \frac{\partial u_2}{\partial x_1} \right|_{(x_1, x_2)} \approx \frac{-3u_2(x_1, x_2) + 6u_2(x_1 + \Delta x_1, x_2) - u_2(x_1 + 2\Delta x_1, x_2) - 2u_2(x_1 - \Delta x_1, x_2)}{6\Delta x_1} \quad (3.76)$$

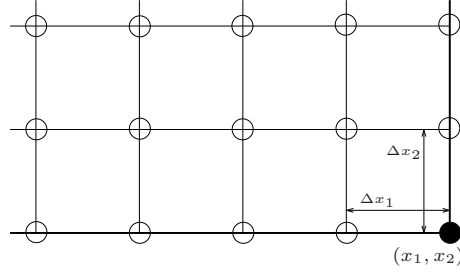


Figure 3.9: Schematic of the mesh indicating a corner node

$$\left. \frac{\partial u_2}{\partial x_2} \right|_{(x_1, x_2)} \approx \frac{-11u_2(x_1, x_2) + 18u_2(x_1, x_2 + \Delta x_2) - 9u_2(x_1, x_2 + 2\Delta x_2) + 2u_2(x_1, x_2 + 3\Delta x_2)}{6\Delta x_2}. \quad (3.77)$$

Equations (3.74), (3.76) and (3.77) are substituted into Equations (3.72) and (3.73) and the two equations are solved for displacements u_1 and u_2 .

Similarly, for a corner node as shown in Figure 3.9, the displacement gradients are given by:

$$\left. \frac{\partial u_1}{\partial x_1} \right|_{(x_1, x_2)} \approx \frac{11u_1(x_1, x_2) - 18u_1(x_1 - \Delta x_1, x_2) + 9u_1(x_1 - 2\Delta x_1, x_2) - 2u_1(x_1 - 3\Delta x_1, x_2)}{6\Delta x_1} \quad (3.78)$$

$$\left. \frac{\partial u_2}{\partial x_2} \right|_{(x_1, x_2)} \approx \frac{-11u_2(x_1, x_2) + 18u_2(x_1, x_2 + \Delta x_2) - 9u_2(x_1, x_2 + 2\Delta x_2) + 2u_2(x_1, x_2 + 3\Delta x_2)}{6\Delta x_2}. \quad (3.79)$$

A similar approach is followed for the remaining boundaries and corners giving a higher-order finite volume formulation that can model a third-order displacement field exactly.

3.6 Temporal Discretisation and Solution Procedure

The temporal term in Equations (3.43) and (3.23) is discretised using a dual-timestepping solution procedure [60, 61], such that second-order temporal accuracy is achieved and the equations are solved in a matrix-free iterative process.

The dual-timestepping procedure is independent of the spatial discretisation strategy employed, viz. finite volume or finite element. For the finite volume method, Equation (3.46), the spatial terms are grouped together and the equation re-written as follows:

$$\rho_o \frac{d}{dt} \int_{\mathcal{V}_m} v_i d\mathcal{V}_o = \sum_{\Upsilon_{mn} \cap \mathcal{V}_m} P_{iJ} \cdot C_{J:mn} + \sum_{\Upsilon_{mn}^B \cap \mathcal{V}_m} P_{iJ} \cdot B_{J:mn} \quad (3.80)$$

$$\rho_o \mathcal{V}_m \frac{dv_i}{dt} = RHS_i \quad (3.81)$$

where the subscript m indicates the node number and i the component in the x_1 - or x_2 -direction.

Now, a pseudo-time temporal term is added to the left-hand-side of the equation and the real-time temporal term added as a source term to the right-hand-side of the equation. Equation (3.81) becomes

$$\rho_o \frac{dv_i}{d\tau} \mathcal{V}_m = RHS_i - \rho_o \frac{dv_i}{dt} \mathcal{V}_m. \quad (3.82)$$

The solution is driven to pseudo-steady state, i.e. $\frac{dv_i}{d\tau} = 0$, which makes Equations (3.81) and (3.82) equivalent and also implies that the actual governing equations are solved in an implicit fashion.

Since the accuracy of the pseudo-time temporal term is of little consequence, as it becomes zero upon convergence, it is discretised to first-order accuracy while the real-time temporal term is discretised to second-order accuracy, giving

$$\rho_o \frac{v_i^{\tau+\Delta\tau} - v_i^\tau}{\Delta\tau} \mathcal{V}_m \approx RHS_i - \rho_o \frac{3v_i^{\tau+\Delta\tau} - 4v_i^\tau + v_i^{\tau-\Delta\tau}}{2\Delta t} \mathcal{V}_m \quad (3.83)$$

where Δt is the real-timestep size and $\Delta\tau$ the pseudo-timestep size.

For the finite element method, applying the same dual-timestepping procedure as above to Equation (3.36) gives

$$\sum_e \rho_o \int_{\mathcal{V}_e} [N]^T [N] d\mathcal{V}_o \frac{d\{v_i\}}{dt} = \sum_e \{F_{\text{ext}}\} - \sum_e \left(\sum_{\text{Gauss pts}} [B]^T [P] \det(\mathbf{J}) W_{GP} \right) \quad (3.84)$$

$$\sum_e [M_e]_{\text{cons}} \frac{d\{v_i\}}{dt} = RHS_i, \quad (3.85)$$

where $[M_e]_{\text{cons}} = \rho_o \int_{\mathcal{V}_e} [N]^T [N] d\mathcal{V}_o$ is the element consistent mass matrix. Therefore, the nodal mass in the finite volume method, Equation (3.81), is now replaced by an element mass matrix in the finite element method, Equation (3.85).

For the bilinear Q4 element the shape functions are given by Equation (3.24), therefore using 2×2 Gauss quadrature integration yields the following element consistent mass matrix:

$$[M_e]_{Q4_{\text{cons}}} = \frac{\rho_o \mathcal{V}_e}{36} \begin{bmatrix} 4 & 2 & 1 & 2 \\ 2 & 4 & 2 & 1 \\ 1 & 2 & 4 & 2 \\ 2 & 1 & 2 & 4 \end{bmatrix}. \quad (3.86)$$

Similarly, the Q8 element consistent mass matrix is:

$$[M_e]_{Q8_{\text{cons}}} = \frac{\rho_o \mathcal{V}_e}{108} \begin{bmatrix} 2 & 0 & 1 & 0 & -2 & -4 & -4 & -2 \\ 0 & 2 & 0 & 1 & -2 & -2 & -4 & -4 \\ 1 & 0 & 2 & 0 & -4 & -2 & -2 & -4 \\ 0 & 1 & 0 & 2 & -4 & -4 & -2 & -2 \\ -2 & -2 & -4 & -4 & 16 & 12 & 8 & 12 \\ -4 & -2 & -2 & -4 & 12 & 16 & 12 & 8 \\ -4 & -4 & -2 & -2 & 8 & 12 & 16 & 12 \\ -2 & -4 & -4 & -2 & 12 & 8 & 12 & 16 \end{bmatrix}. \quad (3.87)$$

Adding a pseudo-time temporal term and treating the real-time temporal term as a source term gives

$$\sum_e [M_e]_{\text{lumped}} \frac{d\{v_i\}}{d\tau} = RHS_i - \sum_e [M_e]_{\text{cons}} \frac{d\{v_i\}}{dt}, \quad (3.88)$$

where $[M_e]_{\text{lumped}}$ is the diagonal element lumped mass matrix, obtained by placing particle masses on the diagonals or at nodes. The advantage of using the lumped mass matrix for the pseudo-time temporal term is less computational storage and processing time, as the equations are uncoupled and solved in an explicit matrix-free manner.

To obtain the lumped mass matrix for the Q4 element, a simple row summation method was used [21], where contributions of the consistent mass matrix are summed over all the columns and lumped on the diagonal of the lumped mass matrix:

$$[M_e]_{Q4_{\text{lumped}}} = \frac{\rho_o \mathcal{V}_e}{36} \begin{bmatrix} 9 & 0 & 0 & 0 \\ 0 & 9 & 0 & 0 \\ 0 & 0 & 9 & 0 \\ 0 & 0 & 0 & 9 \end{bmatrix}. \quad (3.89)$$

However, for the Q8 element, a lumped mass matrix using the row summation method proved to be unstable for certain cases and the HRZ lumping approach [29] was required:

$$[M_e]_{Q8_{\text{lumped}}} = \frac{\rho_o \mathcal{V}_e}{36} \begin{bmatrix} 1 & 0 & 0 & 0 & 0 & 0 & 0 & 0 \\ 0 & 1 & 0 & 0 & 0 & 0 & 0 & 0 \\ 0 & 0 & 1 & 0 & 0 & 0 & 0 & 0 \\ 0 & 0 & 0 & 1 & 0 & 0 & 0 & 0 \\ 0 & 0 & 0 & 0 & 8 & 0 & 0 & 0 \\ 0 & 0 & 0 & 0 & 0 & 8 & 0 & 0 \\ 0 & 0 & 0 & 0 & 0 & 0 & 8 & 0 \\ 0 & 0 & 0 & 0 & 0 & 0 & 0 & 8 \end{bmatrix}. \quad (3.90)$$

To introduce the primary variable, displacement, into the equation, we simply note that velocity is the temporal rate of change of displacement, u_i ,

$$\frac{du_i}{dt} = v_i. \quad (3.91)$$

Discretising the displacement equation using the same approach as for velocity above, gives

$$\frac{u_i^{\tau+\Delta\tau} - u_i^\tau}{\Delta\tau} \approx v_i^{\tau+\Delta\tau} - \frac{3u_i^{\tau+\Delta\tau} - 4u_i^\tau + u_i^{\tau-\Delta\tau}}{2\Delta\tau}. \quad (3.92)$$

The solution procedure involves solving for velocity v_i and displacement u_i in an iterative fashion. In order to ensure stability for all cases, a second-order accurate single-step procedure [21] is employed as follows:

1. At timestep $n + 1$, loop over all nodes i and set $u_i^\tau = u_i^n$ and $v_i^\tau = v_i^n$.
2. Calculate a projected displacement by discretising Equation (3.91) as follows:

$$\bar{u}_i^\tau = u_i^\tau + \Delta\tau \left(v_i^\tau - \frac{3u_i^{\tau+\Delta\tau} - 4u_i^\tau + u_i^{\tau-\Delta\tau}}{2\Delta\tau} \right). \quad (3.93)$$

3. Using \bar{u}_i^τ , compute the strain field using Equations (2.32) and (2.33) and the stress field using Equations (2.26) and (2.31).
4. Solve for $v_i^{\tau+\Delta\tau}$ explicitly using the discretised form of the equilibrium equations, Equation (3.83) for the finite volume method and Equation (3.88) for the finite element method.
5. Update the displacement at $\tau + \Delta\tau$ using the latest velocity $v_i^{\tau+\Delta\tau}$ and the acceleration, calculated in step 3, i.e.

$$u_i^{\tau+\Delta\tau} = u_i^\tau + \Delta\tau \left(v_i^{\tau+\Delta\tau} - \frac{3u_i^{\tau+\Delta\tau} - 4u_i^\tau + u_i^{\tau-\Delta\tau}}{2\Delta\tau} \right) + \frac{1}{2} \Delta\tau^2 \frac{1}{\rho_o \mathcal{V}_m} \left(RHS_i |_{\bar{u}_i^\tau} - \rho_o \frac{3v_i^{\tau+\Delta\tau} - 4v_i^\tau + v_i^{\tau-\Delta\tau}}{2\Delta\tau} \mathcal{V}_m \right). \quad (3.94)$$

6. The residuals of the equilibrium equation are calculated, $Res_i = v_i^{\tau+\Delta\tau} - v_i^\tau$.
7. The overall residual is calculated from the root mean square of that at each node, therefore $Res = \sqrt{\sum_i^n (Res_i)^2 / n}$, where n is the number of nodes.
8. If the residuals are greater than the convergence tolerance, Steps 2 to 5 are repeated.
9. If the residuals are less than the convergence tolerance, $v_i^{\tau+\Delta\tau} \approx v_i^\tau$, and the real-timestep is terminated. Therefore, $v_i^{n+1} = v_i^{\tau+\Delta\tau}$ and $u_i^{n+1} = u_i^{\tau+\Delta\tau}$. The next timestep is entered by proceeding to Step 1.

The dual-timestepping procedure, described above for both the finite volume and finite element methods, is explicit in pseudo-time, which means it is a conditionally stable scheme and a limit exists on the pseudo-timestep size $\Delta\tau$.

The procedure is implicit in real-time, thus the scheme is stable for any choice of the real-timestep size Δt .

A stable solution process exists if $\Delta\tau < \Delta\tau_{\text{cr}}$, where $\Delta\tau_{\text{cr}}$ is the critical timestep size [21] defined by the following expression:

$$\frac{\Delta x_i}{\Delta\tau_{\text{cr}}} > \sqrt{\frac{K}{\rho_o}} + \sqrt{\frac{G}{\rho_o}} \quad (3.95)$$

where Δx_i is the effective mesh spacing in the i -direction and K and G are the bulk and shear modulus,

$$K = \frac{E}{3(1 - 2\nu)}, \quad (3.96)$$

$$G = \frac{E}{2(1 + \nu)}. \quad (3.97)$$

A further limitation exists in that $\Delta\tau$ must be less than Δt , therefore the actual pseudo-timestep size is chosen such that:

$$\Delta\tau_{\text{actual}} = \Delta\tau_{\text{cr}} \left[1 + \frac{3}{2} \frac{\Delta\tau_{\text{cr}}}{\Delta t} \right]^{-1}, \quad (3.98)$$

where the nomenclature is as previously defined.

3.7 Conclusion

In this chapter, the method of weighted residuals was discussed. Although the finite element method (FEM) is more common for computational solid mechanics (CSM), the finite volume method (FVM) is receiving increased attention for this purpose. However, not much work has been done with the FVM for structures undergoing geometrically non-linear deformations. Furthermore, no rigorous comparison between the FVM and FEM is available in the literature.

In this work, both the FVM and FEM of discretisation, and variants thereof, were employed to spatially discretise the governing equations. In particular, a linear Q4 FEM and higher-order Q8 FEM, as well as a vertex-centred FVM and hybrid FVM were implemented. A detailed error analysis was conducted on the finite volume methods and a higher-order FVM developed. An implicit matrix-free second-order accurate dual-timestepping temporal discretisation procedure was employed. The accuracy of all these schemes is evaluated in the next chapter, via application to a number of test problems.

Chapter 4

Numerical Results and Evaluation

4.1 Introduction

The previous chapter detailed the mathematical description of the finite volume (FVM) and finite element (FEM) methods for discretising the equations governing geometrically non-linear solid mechanics. Three finite volume methods were described: a vertex-centred or nodal method, a recently developed hybrid method and a newly developed higher-order method. With regards to finite element methods, standard linear Q4 elements and higher-order Q8 elements were detailed. In this chapter, the accuracy of the schemes are evaluated in a rigorous manner via application to 2D test problems with increasing degree of complexity. This serves to identify the preferred method for modelling thin geometrically non-linear structures, which will be used for fluid-structure interaction modelling.

4.2 Uniaxial Tension

The first test problem considered was that of a 2D body in uniaxial tension, shown in Figure 4.1. The solid has a Young's modulus of $E = 210$ GPa, Poisson's ratio $\nu = 0.3$ and a length and width of 1 mm. Plane strain was assumed in the analysis. The mesh consisted of a single cell.

The normal stress, σ_{11} , from the finite volume and finite element formulations are plotted against tip displacement, c , in Figure 4.2. The formulations give exactly the same results. Furthermore, it can be seen that the geometrically non-linear formulation was implemented correctly, since the σ_{11} stress increases linearly with an increase in c for small displacements, but deviates from the linear elasticity behaviour at larger displacements. This is expected since at large displacements there is a geometric decrease in cross-section that results in

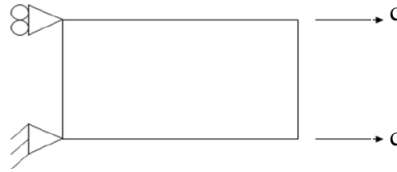


Figure 4.1: Solid body in uniaxial tension

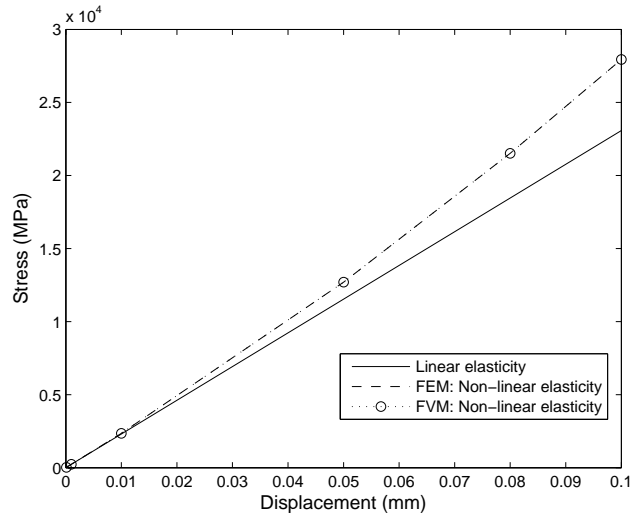


Figure 4.2: Comparison of σ_{11} stress for uniaxial tension

an increase in stress.

4.3 Simple Shear

A 2D body subjected to the deformation

$$x_1 = X_1 + cX_2 \tag{4.1}$$

$$x_2 = X_2, \tag{4.2}$$

which results in the body undergoing simple shear as shown in Figure 4.3, was considered next. The same geometry, mesh and material properties as the previous case, were used.

Both the σ_{11} and σ_{12} stress components are plotted against tip displacement, c , in Figure 4.4. Again, the finite volume and finite element non-linear elasticity formulations give exactly the same results. The linear elasticity formulation predicts zero normal stress components and the shear stress, σ_{12} , increases linearly

with an increase in c . Using the non-linear formulations, all the stress terms are non-zero. The reason for this is due to the overly constrained structure, which wants to contract in the x_1 -direction due to the shear stress but the constraints, however, do not allow for this contraction. This results in a strain in the x_2 -direction and because of the Poisson effect this strain results in normal stress components, σ_{11} and σ_{22} .

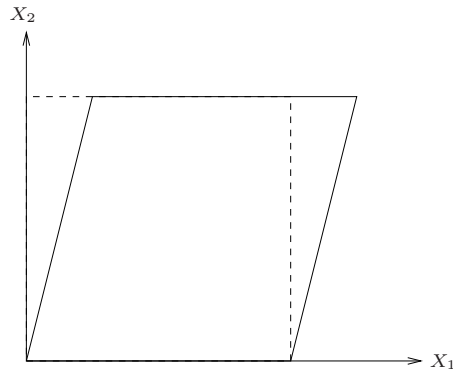


Figure 4.3: Solid body in simple shear

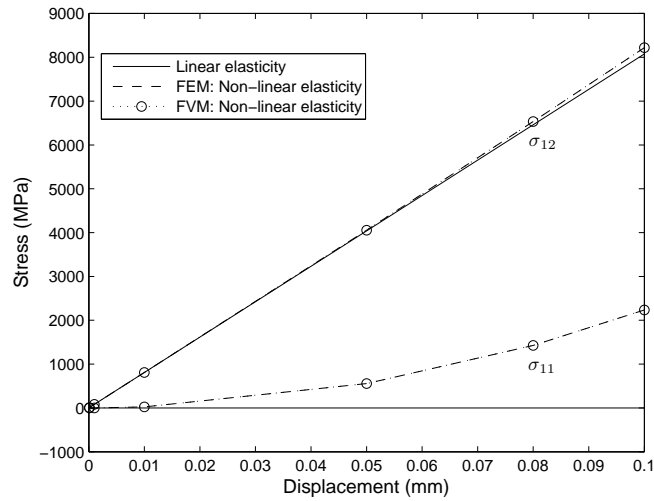


Figure 4.4: Comparison of σ_{11} and σ_{12} stress for simple shear

4.4 Pure Bending

The next test-case considered was that of a thin beam in pure bending, Figure 4.5. The beam was clamped at one end and subjected to a moment at the free end. The material properties used were a Young's modulus $E = 210$ GPa and Poisson's ratio $\nu = 0$. The length $l = 6$ mm, height $h = 1$ mm and the plane stress assumption were used.



Figure 4.5: Cantilever beam in pure bending

A linear elastic solid model was used for this problem. The analytical solution for the displacement of the beam can be derived from first principles and is given by

$$u_1 = \frac{Mx_1x_2}{EI} \quad (4.3)$$

$$u_2 = -\frac{Mx_1^2}{2EI}, \quad (4.4)$$

where u_1 and u_2 are the displacements in the x_1 - and x_2 -directions respectively, M is the bending-moment at the free end and I is the moment of inertia of the cross-section of the beam.

Meshes with varying element aspect ratios, as shown in Figure 4.6, were used to analyse this problem. The element aspect ratio is defined as the ratio of the element length to its height. Note that the number of elements in each mesh were chosen so that by keeping the total number of elements constant, varying aspect ratios could be obtained.

The resulting tip displacements when using the linear four-node (Q4) and higher-order eight-node (Q8) finite element formulations are shown in Figure 4.7(a), together with the analytical solution. While the Q8 FEM is exact, the well known shear locking phenomenon [29] is evident with the Q4 FEM. When subjected to pure bending, Q4 elements produce a shear strain contribution in addition to the expected bending strain. This parasitic shear strain absorbs strain energy and to compensate the displacements decrease or the structure stiffens or locks. This shear locking effect is magnified when the aspect ratio is increased, i.e. as the elements become long and thin, the structure becomes stiffer and results in decreasing displacements. This effect can clearly be seen in Figure 4.7(a).

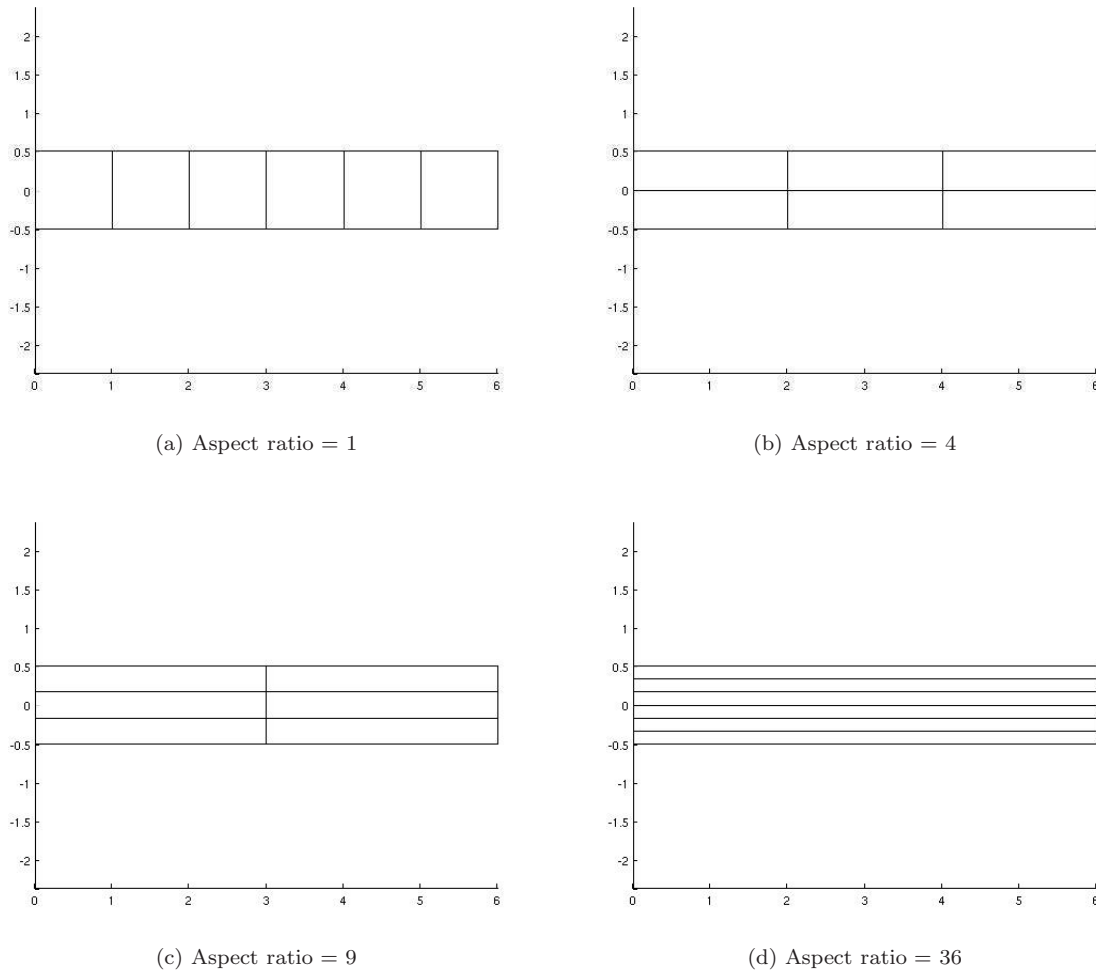


Figure 4.6: Meshes with varying element aspect ratios used for analysing a beam in pure bending

The results from the three finite volume formulations are shown in Figure 4.7(b). The vertex-centred FVM also suffers from shear locking. The hybrid and higher-order FVM are, however, locking-free, with both predicting the exact tip displacement for this problem.

4.4.1 Error Analysis: Application to Beam in Pure Bending

The analytical solution for the displacement of a beam in pure bending is given by Equations (4.3) and (4.4). Since it is a quadratic displacement field, it is ex-

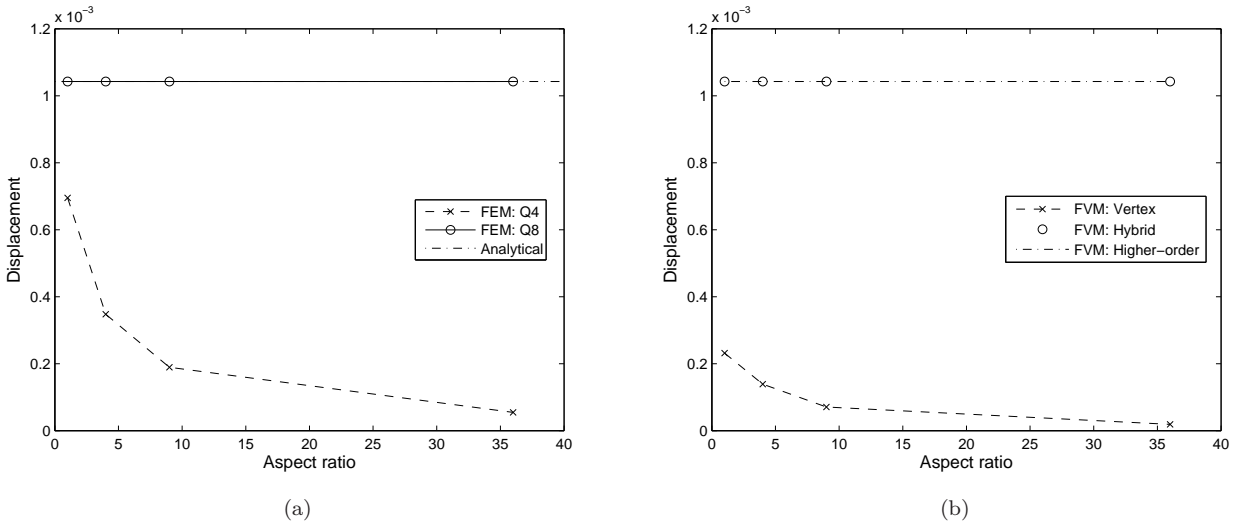


Figure 4.7: Tip displacement as a function of element aspect ratio: (a) Q4 and Q8 FEM; (b) vertex-centred, hybrid and higher-order FVM

pected that the Q8 FEM and higher-order FVM are exact. The hybrid FVM's superiority over the Q4 FEM and vertex-centred FVM is an interesting finding. As shown in Chapter 3, both the hybrid and vertex-centred formulation should contain error terms at the corners. To understand the difference in accuracy between the two formulations, the exact errors can be obtained by substituting the analytical solution into the expressions for the errors, Equations (3.59) to (3.66). These are summarised in Table 4.1.

The error expressions in Table 4.1 confirm the numerical results obtained (Figure 4.7(b)). The errors for the hybrid formulation cancel out and the exact solution is obtained. However, with the vertex-centred formulation there is an error at the corner nodes that scales as $\frac{\Delta x_1}{\Delta x_2}$, i.e. the error increases with an increase in aspect ratio. This explains the shear locking effect observed above.

	Vertex-centred FVM	Hybrid FVM
Internal node	0	0
Boundary node	0	0
Corner node	$\frac{M}{2I} \frac{\Delta x_1}{\Delta x_2}$	0

Table 4.1: Errors of vertex-centred and hybrid formulations for a beam in pure bending

4.5 Thin Cantilever Beam in Non-linear Bending

The final steady-state test-case analysed was that of a thin cantilever beam subjected to a tip load at the free end, undergoing geometrically non-linear bending (Figure 4.8). The beam has a Young's modulus of 0.2 MPa and Poisson's ratio of 0.35. The tip load, F , of 3.3×10^{-5} N was chosen to result in large tip displacements.

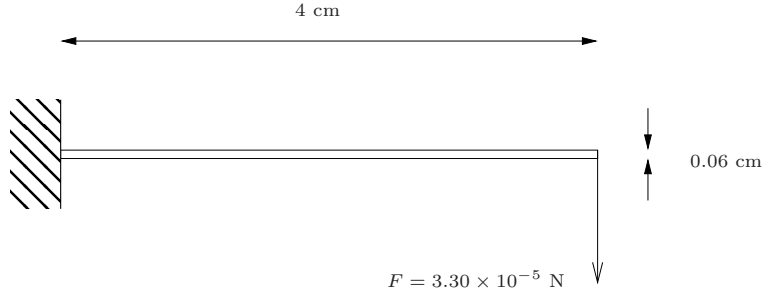


Figure 4.8: Thin cantilever beam undergoing large non-linear displacements

This test-case is of particular importance as it contains all the stress components of the FSI system considered in this work. A combination of both bending and shear deformation effects are present. Ignoring thickness effects, an analytical solution of the Euler-Bernoulli beam equation for geometrically non-linear deflections is given by [62]:

$$u_1 = \sqrt{\frac{2EI}{F}} \left(\sqrt{\sin\varphi_0} - \sqrt{\sin\varphi_0 - \sin\varphi} \right) \quad (4.5)$$

$$u_2 = \sqrt{\frac{EI}{2F}} \int_0^\varphi \frac{\sin\varphi d\varphi}{\sqrt{\sin\varphi_0 - \sin\varphi}} \quad (4.6)$$

where u_1 and u_2 are the horizontal and vertical deflections at any point along the beam and φ is the slope of the beam, which varies between 0 and its value at the end of the beam, φ_0 . The slope at the end of the beam φ_0 is computed from the implicit equation

$$L = \sqrt{\frac{EI}{2F}} \int_0^{\varphi_0} \frac{d\varphi}{\sqrt{\sin\varphi_0 - \sin\varphi}}, \quad (4.7)$$

where L is the known length of the beam.

In evaluating each numerical scheme, the results are plotted vs. the analytical solution for various mesh densities. The results for the standard vertex-centred FVM are shown in Figure 4.9(a), in which the locking effect, as previously discussed, is evident. This is not seen in the case of the hybrid FVM (Figure 4.9(b)).

However, many elements are required through the thickness (in excess of 10) in order to achieve a certain amount of accuracy. This had a negative effect on computational cost as the small edge-lengths require that the pseudo-timestep sizes are small for stable solution (refer to Equation 3.95).

Using the newly developed higher-order FVM on the other hand, a relatively coarse mesh requiring only three elements through the thickness of the structure offered an accurate solution, as shown in Figure 4.9(c). However, the use of more elements through the thickness yielded an unstable solution process, the resolution of which falls beyond the scope of this work.

The results for the Q4 FEM and Q8 FEM are shown in Figures 4.9(d) and 4.9(e). As expected, the Q4 elements suffer from locking when the aspect ratios are large. The Q8 elements produced the most desirable results and a 40×1 mesh gives the analytical result.

4.5.1 Error Analysis: Application to Thin Beam in Bending

The error analysis for the vertex-centred and hybrid finite volume formulations done in Chapter 3 can again be quantified by applying it to this problem of a thin cantilever beam subjected to a concentrated tip load (Figure 4.8). For comparison with the error analysis, the problem was limited to the small displacement case and a Poisson's ratio of zero was used. The analytical solution, derived from first principles, for the small displacement case is given by:

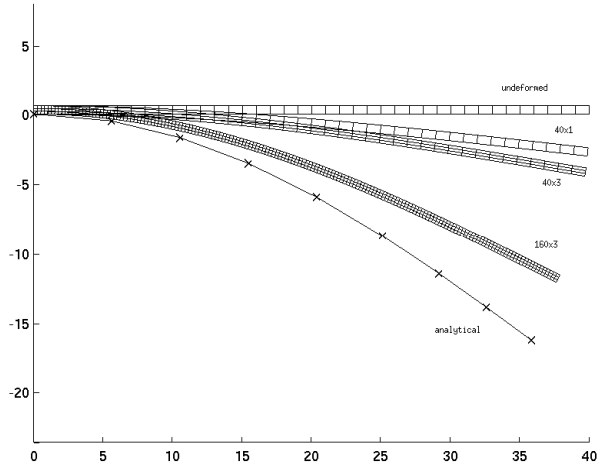
$$u_1 = \frac{F}{EI} \left(-Lx_1x_2 + c^2x_2 + \frac{1}{2}x_1^2x_2 - \frac{1}{3}x_2^3 \right) \quad (4.8)$$

$$u_2 = \frac{F}{EI} \left(\frac{1}{2}Lx_1^2 - \frac{1}{6}x_1^3 \right) \quad (4.9)$$

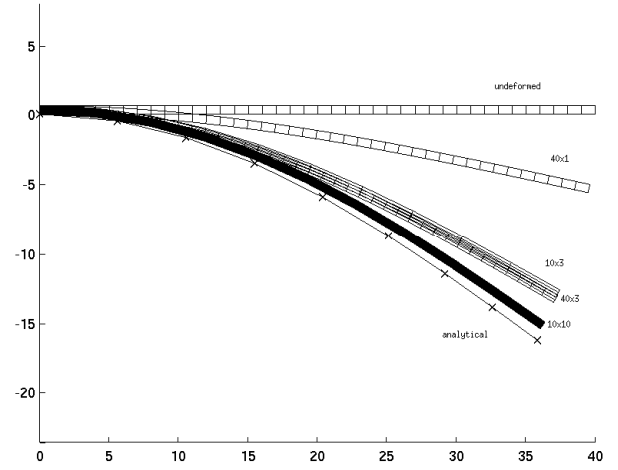
where F is the magnitude of the tip load, L is the length of the beam and $2c$ is the thickness of the beam. Substituting the analytical equations into the error expressions, Equations (3.59) to (3.66), yields the leading-order error terms as shown in Table 4.2, with the nomenclature as previously defined.

The results in Table 4.2 show that for this test-case, the difference between the two formulations is in the x_1 -momentum equation at the left corners of the beam. The vertex-centred formulation contains an error term that scales as $\frac{\Delta x_1}{\Delta x_2}$. This, again, explains the sensitivity to aspect ratio or shear locking effect present with the formulation. The corresponding error term for the hybrid formulation is zero. These analytical expressions correspond with the numerical results for the small displacement case as shown in Figure 4.10; the hybrid finite volume method is not sensitive to the element aspect ratio, which results in more accurate solutions.

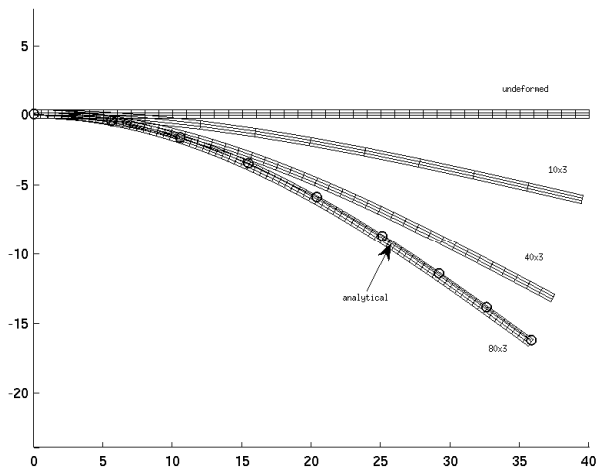
The rates of convergence of displacements for the vertex-centred and hybrid finite volume formulations, as discussed in Chapter 3, were investigated numerically on this problem. A constant element aspect ratio of 20/3 was used and meshes of increasing refinedness were generated by repeatedly halving the



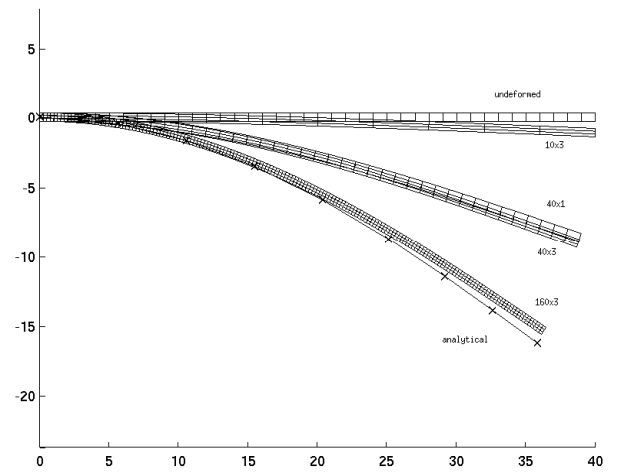
(a) Vertex-centred FVM



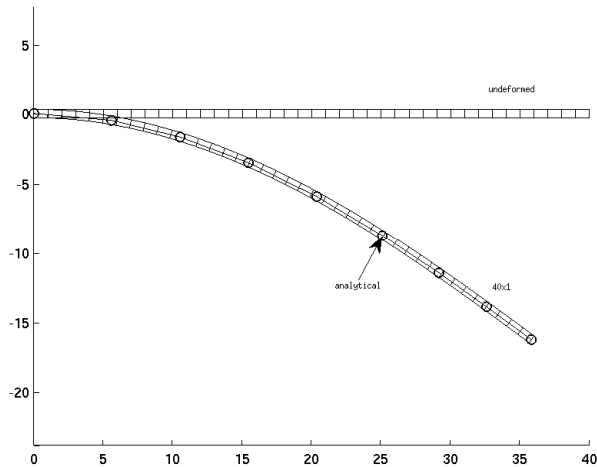
(b) Hybrid FVM



(c) Higher-order FVM



(d) Q4 FEM



(e) Q8 FEM

Figure 4.9: Calculated beam deflection for various meshes: (a) Vertex-centred FVM; (b) Hybrid FVM; (c) Higher-order FVM; (d) Q4 FEM; (e) Q8 FEM

	Vertex-centred FVM	Hybrid FVM
Internal node	0	0
Boundary node (top/bottom):		
x_1 -momentum	$(-1)^{p+1} \left(\frac{1}{3} \frac{F}{T} \Delta x_2 + \frac{1}{6} \frac{F}{T} \frac{\Delta x_1^2}{\Delta x_2} \right)$	$(-1)^{p+1} \left(\frac{1}{3} \frac{F}{T} \Delta x_2 + \frac{1}{6} \frac{F}{T} \frac{\Delta x_1^2}{\Delta x_2} \right) + (-1)^p \frac{1}{4} \frac{F}{T} \frac{\Delta x_1^2}{\Delta x_2}$
x_2 -momentum	0	0
Boundary node (right):		
x_1 -momentum	0	0
x_2 -momentum	$-\frac{1}{12} \frac{F}{T} \Delta x_1 + \frac{1}{3} \frac{F}{T} \frac{\Delta x_2^2}{\Delta x_1}$	$-\frac{1}{12} \frac{F}{T} \Delta x_1 + \frac{1}{3} \frac{F}{T} \frac{\Delta x_2^2}{\Delta x_1}$
Corner node (right):		
x_1 -momentum	0	0
x_2 -momentum	$(-1)^p \frac{Fc}{T} \frac{\Delta x_2}{\Delta x_1}$	$(-1)^p \frac{Fc}{T} \frac{\Delta x_2}{\Delta x_1}$
Corner node (left):		
x_1 -momentum	$(-1)^p \frac{FL}{2T} \frac{\Delta x_1}{\Delta x_2}$	0
x_2 -momentum	$(-1)^p \frac{Fc}{T} \frac{\Delta x_2}{\Delta x_1}$	$(-1)^p \frac{Fc}{T} \frac{\Delta x_2}{\Delta x_1}$

Table 4.2: Errors of vertex-centred and hybrid formulations for a cantilever beam subjected to a tip load

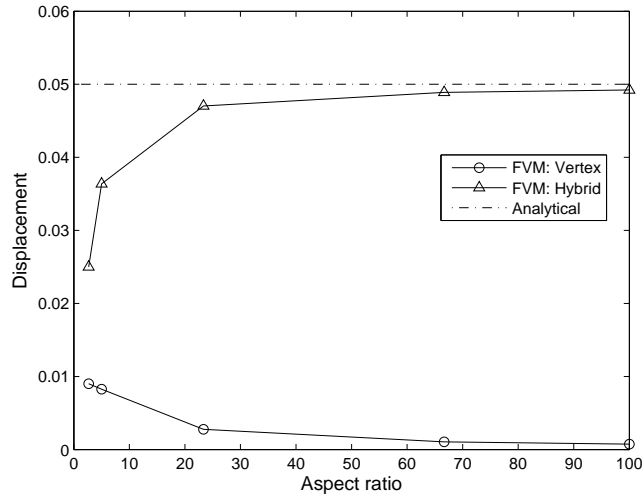


Figure 4.10: Tip displacement as a function of element aspect ratio for a thin cantilever beam subjected to a concentrated tip load

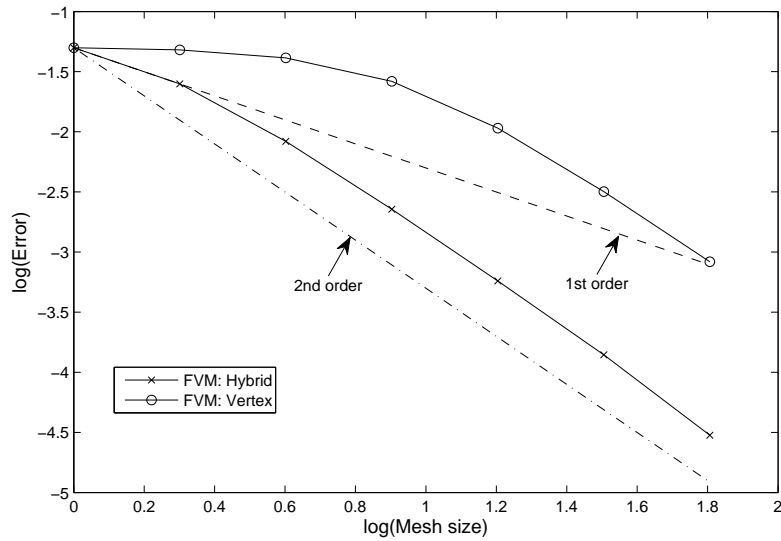


Figure 4.11: Convergence rate of displacements

element size in both directions. A plot of the logarithm of the error of tip displacements vs. the logarithm of the mesh size is shown in Figure 4.11. The negative of the gradient of this curve gives the rate of convergence: 2.0 for the hybrid formulation and 1.9 for the vertex-formulation. Therefore, both formulations tend towards second-order accuracy. However, it is clearly evident in Figure 4.11 that for a given mesh spacing the hybrid formulation is more accurate than the vertex-centred formulation. These results correlate with those obtained from the analytical analysis (Table 3.1): as the meshes get finer, the number of internal nodes is significantly more than boundary and corner nodes and the schemes tend towards second-order accuracy.

4.6 Dynamic 2D Beam

The test-cases above assessed the spatial accuracy of the different formulations. It was shown that the Q8 FEM produced the most desirable results. In order to assess temporal accuracy when applied to transient problems, the 2D dynamic beam test-case (see Figure 4.12) was considered.

The beam has a Young's modulus $E = 0.2$ MPa, Poisson's ratio $\nu = 0.49$, density $\rho = 2000$ kg m⁻³, length $l = 40$ mm and a cross-section of 0.6 mm \times 10 mm. One end of the beam was clamped while a shear traction $\tau = 0.1$ Pa is suddenly applied at the free end at time $t = 0$. Analytical solutions which include temporal behaviour are only available for the small displacement case, thus the test-case was subjected to this constraint. A 40×1 Q8 FEM mesh was



Figure 4.12: Dynamic beam with applied shear

used in this analysis.

The analytical solution in the small displacement limit is a sinusoidal oscillation given by [11]:

$$u = \frac{4\tau}{E} \frac{l^3}{h^2} (1 - \nu^2) \left[1 + \frac{3}{4}(1 + \nu) \frac{h^2}{l^2} \right] [\cos(\omega_1 t) - 1] \quad (4.10)$$

at a frequency of

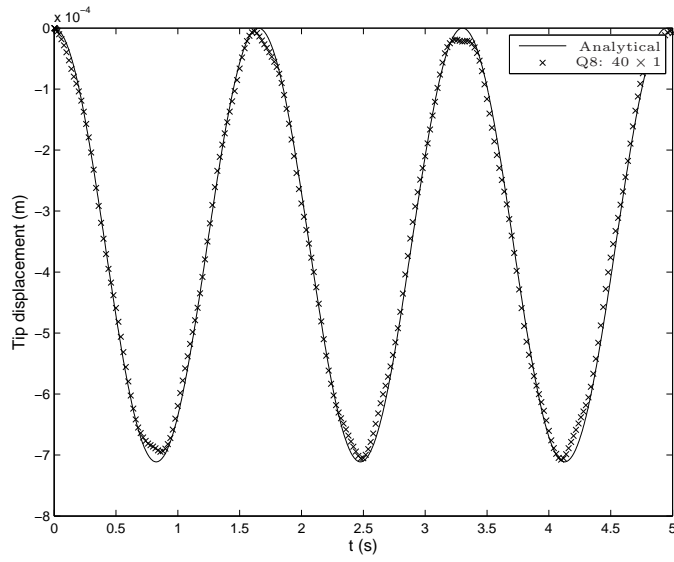
$$\omega_1 = \lambda_1^2 \sqrt{\frac{E}{12\rho} \frac{h}{l^2}}, \quad (4.11)$$

where λ_1 is the eigenvalue of the first mode of oscillation viz. $\lambda_1 = 1.875$ in this test-case.

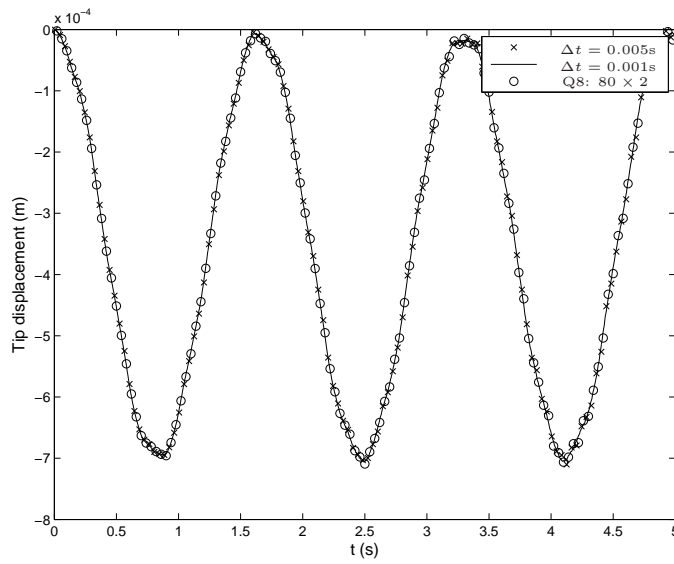
In Figure 4.13(a), the predicted dynamic response of the centre of the beam tip is compared with the analytical solution. The calculated results are plotted every two timesteps, where the timestep size is 0.005 s. An accurate solution is obtained with a relatively coarse mesh, the slight difference at the peaks is due to higher-order modes that are excited in the beam whereas the analytical solution only takes into account the first mode of vibration. Using a finer mesh and smaller timestep size produces exactly the same results, as shown in Figure 4.13(b), which validates the temporal accuracy of the developed technology.

4.7 Conclusion

The three finite volume methods: vertex-centred FVM, hybrid FVM and higher-order FVM; as well as the two finite element schemes: Q4 FEM and Q8 FEM developed in Chapter 3 were rigorously evaluated on representative test problems of increasing complexity. It was shown that both the vertex-centred FVM and Q4 FEM suffer from shear locking or sensitivity to element aspect ratio. The hybrid FVM is locking-free but many elements are required through the thickness of the structure to obtain accurate results. The higher-order FVM produced close to exact results for thin structures in bending, when using three elements through the thickness. However, the Q8 FEM needed only a single element through its thickness to produce accurate results for the steady-state



(a)



(b)

Figure 4.13: Transient response of a cantilever beam when a shear traction of 0.1 Pa is suddenly applied at the free end: (a) Q8 40×1 mesh; (b) using different timesteps and mesh sizes

bending analysis, as well as for the transient analysis. In addition, inherent in the Q8 FEM formulation is the automatic capability of handling problems with unstructured meshes. Overall, the Q8 FEM is the preferred method for modelling thin geometrically non-linear structures.

Part II

Fluid-Structure Interaction

Chapter 5

Fluid-Structure Interaction: Implementation

5.1 Introduction

In this chapter a hybrid finite volume–finite element fluid-structure interaction formulation is developed by coupling the Q8 finite element formulation for the solid with the existing finite volume fluid solver within the *Elemental* framework. Many recent FSI efforts have made use of a single discretisation scheme, either finite volume [11, 13, 14, 35] or finite element [1, 10, 36–39], to solve the entire domain, which simplifies the treatment at the interface of the fluid and solid domain. However, each discretisation method contains certain inherent advantages and should be used as such. Since the framework within *Elemental* is independent of discretisation strategy employed, it allows for the development of a hybrid finite volume–finite element FSI formulation. To the author’s knowledge, this is the first instance in which such a hybrid formulation is applied to strongly-coupled FSI problems. The coupling of a higher-order finite element formulation for the structure and a linear finite volume formulation for the fluid leads to non-matching nodes at the solid interface and the transfer of information at these nodes will also be addressed in this chapter.

The solution of FSI systems range from single or monolithic methods that are inherently strongly-coupled to separate or partitioned methods that can be strongly- or weakly-coupled. This work focusses on FSI systems where there is a strong interaction between the fluid and structural domains and weakly-coupled methods are, therefore, not considered as they may diverge or result in inaccurate solutions [1, 10, 11]. For strongly-coupled methods, the advantage of a monolithic over a partitioned approach is that all the equations are considered simultaneously and a single system of equations solved, which ensures stability and convergence. However, this approach may suffer from ill conditioning and convergence is generally slow [1]. The advantage of a partitioned approach is that it allows the use of two independent solution techniques for the

fluid and solid equations in isolation. The drawback of partitioned approaches is that they generally require a separate coupling algorithm or additional outer iterations between the fluid and solid to achieve strong-coupling, which places an additional computational cost on the scheme [1, 40, 41]. The most popular partitioned coupling algorithms use fixed-point iteration methods or interface Newton-Krylov methods [40, 42]. Fixed-point methods generally make use of Gauss-Seidel iterations which are slow to converge and methods to accelerate convergence, including Aitken and steepest descent relaxation and coarse-grid preconditioning, have been used [41–45]. The Newton-Raphson methods require the computation of Jacobians, which may be difficult to compute exactly and various methods have been developed that use approximate Jacobians [46–48]. In this work the fluid and structural domains are to be solved in a strongly-coupled partitioned manner, where the transfer of information occurs at solver sub-iteration level negating the need for a separate coupling algorithm. To ensure solver stability and computational speed, a simple interface coupling algorithm implemented at sub-iteration level is to be used. Finally, for scalability to large problems the scheme is to be implemented in a matrix-free approach and in such a manner that makes it particularly well-suited for distributed memory parallel hardware architectures.

In this chapter, we introduce the set of governing equations and constitutive relations that describe the fluid domain. The transfer of information at the interface of the fluid and solid domains is detailed. Parallelisation of the solver is discussed. Finally, the solution procedure and dynamic mesh movement are explained.

5.2 Fluid Governing Equation Set

The fluid flow is governed by the Navier-Stokes equations. In general, these equations are expressed in an Eulerian or spatial frame of reference, as opposed to a Lagrangian or material description for the solid, which entails a fixed spatial region with fluid flowing through it. For fluid-structure interaction problems the solid deforms and displaces the fluid domain and a mixture or combination of the two reference frames, referred to as an arbitrary-Lagrangian-Eulerian (ALE) reference frame, results for the motion of the FSI interface. This approach was first described by Hirt et al. [63] and later adopted by many others and is now widely used for FSI applications [12]. A dynamic mesh movement algorithm that deforms the fluid mesh is therefore required and is described later.

Assuming a viscous, incompressible and isothermal fluid, the equations governing the fluid flow are given by the continuity and Navier-Stokes equations:

$$\frac{\partial v_i}{\partial x_i} = 0 \quad (5.1)$$

$$\rho \frac{\partial v_i}{\partial t} + \rho(v_j - v_j^*) \frac{\partial v_i}{\partial x_j} + \frac{\partial p}{\partial x_i} - \frac{\partial \sigma_{ij}}{\partial x_j} - \rho b_i = 0 \quad (5.2)$$

where ρ , v_i , p , σ_{ij} and b_i are the fluid density, fluid velocity, pressure, stress and body forces respectively, x_i are the fixed Eulerian coordinates and v^* is the mesh velocity. The term $(v_j - v_j^*)$ is an ALE convective velocity that results from a difference between the fluid velocity and the mesh velocity.

5.3 Fluid Constitutive Equations

To close the governing equations, a constitutive relation for the stress is required. Assuming a Newtonian fluid, the relationship between stress and rate of strain is given by

$$\sigma_{ij} = \mu \left(\frac{\partial v_i}{\partial x_j} + \frac{\partial v_j}{\partial x_i} \right), \quad (5.3)$$

where μ is the fluid viscosity.

The equations governing the motion of the fluid, Equations (5.1) to (5.3), are discretised via a second-order accurate edge-based hybrid-unstructured finite volume methodology. The incompressibility of the fluid is dealt with using an artificial-compressibility fractional-step algorithm. The details of this fall beyond the scope of this work and the reader is referred to [18, 64] for further details. The coupling between the fluid and solid domain is described in the next section.

5.4 Fluid-Solid Interface Treatment

The fluid-structure interaction system can be described in general or broad terms as follows: the fluid flow provides a traction or load onto the structure. This results in a dynamic response or deformation of the structure which in turn affects the geometry of the fluid domain and the fluid flow. In order to solve this intimately coupled system, the following coupling conditions for the traction, displacement and velocity need to be satisfied at the fluid-solid interface:

$$t_i^s = pn_i - \sigma_{ij}^f n_j \quad (5.4)$$

$$u_i^f = u_i^s \quad (5.5)$$

$$v_i^f = v_i^* = v_i^s \quad (5.6)$$

where n_i is the related unit vector pointing outward from the fluid domain and the superscripts f and s refer to the fluid and solid respectively. Equation (5.4) represents momentum conservation or force equilibrium at the interface, while Equations (5.5) and (5.6) enforce the kinematic or geometric continuity and no-slip conditions respectively.

5.4.1 Consistent Nodal Loads

In this work the fluid and solid elements coincide at the interface, which simplifies the transfer of information between the fluid and solid domains. However,

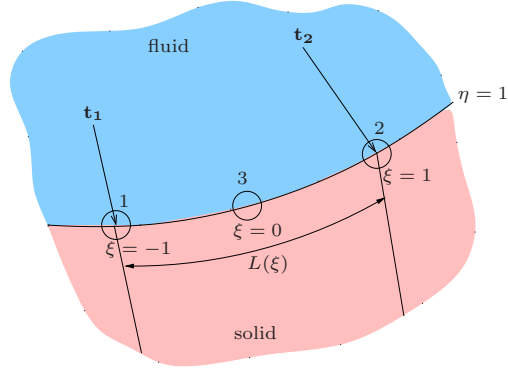


Figure 5.1: Arbitrary solid edge along the FSI interface

the Q8 element contains an additional node at the mid-point of every edge, which means there is an unconnected solid node for every element along the interface. Therefore, the transfer of traction from the fluid to the solid domain has to be evaluated in terms of conservation of momentum and accuracy on the overall solution [65,66]. Two options exist: the traction from every fluid node on the interface is transferred to the corresponding solid node and the mid-nodes are ignored, which satisfies a global conservation of forces, or the traction from the fluid nodes are redistributed to every solid node, which locally is consistent with the finite element method. For the latter approach, the consistent FEM nodal loads are calculated as follows: the finite element representation for nodal loads $\{F\}$ induced by body forces \mathbf{b} , traction \mathbf{t} and point loads $\{P\}$ is

$$\{F\} = \int_{\mathcal{V}} [N]^T \mathbf{b} d\mathcal{V} + \int_S [N]^T \mathbf{t} dS + \{P\}. \quad (5.7)$$

Referring to Figure 5.1, which shows the traction imposed on an arbitrary solid edge along the FSI interface due to the fluid pressure and stress fields, the consistent nodal loads are given by:

$$\{F\} = b \int_0^L [N]^T \mathbf{t} dL \quad (5.8)$$

where $[N]$ contains the shape functions associated with each node along the edge, L is the length of the edge and b is the depth of the element.

Assuming the traction \mathbf{t} varies linearly between \mathbf{t}_1 and \mathbf{t}_2 (which is the case

with the fluid discretisation [34]), Equation (5.8) can be expanded as

$$\begin{Bmatrix} F_{1x_1} \\ F_{1x_2} \\ F_{2x_1} \\ F_{2x_2} \\ F_{3x_1} \\ F_{3x_2} \end{Bmatrix} = b \int_{-1}^1 \begin{bmatrix} N_1 & 0 \\ 0 & N_1 \\ N_2 & 0 \\ 0 & N_2 \\ N_3 & 0 \\ 0 & N_3 \end{bmatrix} \left[S_1 \begin{Bmatrix} t_{1x_1} \\ t_{1x_2} \end{Bmatrix} + S_2 \begin{Bmatrix} t_{2x_1} \\ t_{2x_2} \end{Bmatrix} \right] \frac{dL}{d\xi} d\xi, \quad (5.9)$$

where the integral is transformed to the natural coordinate system and S_i are the linear shape functions assumed for the traction, i.e.

$$S_1 = \frac{1}{2}(1 - \xi) \quad S_2 = \frac{1}{2}(1 + \xi) . \quad (5.10)$$

Since the solid elements are Q8 elements, the quadratic shape functions associated with each node along the edge are

$$N_1 = -\frac{1}{2}\xi(1 - \xi) \quad N_2 = \frac{1}{2}\xi(1 + \xi) \quad N_3 = (1 - \xi^2) . \quad (5.11)$$

Assuming straight edges in the undeformed configuration, which is valid for problems considered in this work, the length of the edge can be expressed in the natural coordinate system as

$$L(\xi) = N_1 L_1 + N_2 L_2 + N_3 L_3, \quad (5.12)$$

therefore the derivative of L with respect to ξ , used in Equation (5.9), is

$$\frac{dL}{d\xi} = \frac{dN_1}{d\xi} L_1 + \frac{dN_2}{d\xi} L_2 + \frac{dN_3}{d\xi} L_3 \quad (5.13)$$

$$= -\frac{1}{2}(1 - 2\xi)L_1 + \frac{1}{2}(1 + 2\xi)L_2 - 2\xi L_3. \quad (5.14)$$

Substituting Equations (5.10) to (5.14) into Equation (5.9) gives

$$\begin{Bmatrix} F_{1x_1} \\ F_{1x_2} \\ F_{2x_1} \\ F_{2x_2} \\ F_{3x_1} \\ F_{3x_2} \end{Bmatrix} = b \int_{-1}^1 \begin{bmatrix} -\frac{1}{2}\xi(1 - \xi) & 0 \\ 0 & -\frac{1}{2}\xi(1 - \xi) \\ \frac{1}{2}\xi(1 + \xi) & 0 \\ 0 & \frac{1}{2}\xi(1 + \xi) \\ (1 - \xi^2) & 0 \\ 0 & (1 - \xi^2) \end{bmatrix} \left\{ \begin{array}{l} \frac{1}{2}(1 - \xi)t_{1x_1} + \frac{1}{2}(1 + \xi)t_{2x_1} \\ \frac{1}{2}(1 - \xi)t_{1x_2} + \frac{1}{2}(1 + \xi)t_{2x_2} \end{array} \right\} \left(-\frac{1}{2}(1 - 2\xi)L_1 + \frac{1}{2}(1 + 2\xi)L_2 - 2\xi L_3 \right) d\xi. \quad (5.15)$$

The integrand is a fourth-order polynomial. Analytical integration gives the

closed form expressions:

$$\left\{ \begin{array}{l} F_{1x_1} \\ F_{1x_2} \\ F_{2x_1} \\ F_{2x_2} \\ F_{3x_1} \\ F_{3x_2} \end{array} \right\} = \left\{ \begin{array}{l} -\frac{b}{30}(13L_1t_{1x_1} + 2L_1t_{2x_1} + 3L_2t_{1x_1} + 2L_2t_{2x_1} - 16L_3t_{1x_1} - 4L_3t_{2x_1}) \\ -\frac{b}{30}(13L_1t_{1x_2} + 2L_1t_{2x_2} + 3L_2t_{1x_2} + 2L_2t_{2x_2} - 16L_3t_{1x_2} - 4L_3t_{2x_2}) \\ \frac{b}{30}(2L_1t_{1x_1} + 3L_1t_{2x_1} + 2L_2t_{1x_1} + 13L_2t_{2x_1} - 4L_3t_{1x_1} - 16L_3t_{2x_1}) \\ \frac{b}{30}(2L_1t_{1x_2} + 3L_1t_{2x_2} + 2L_2t_{1x_2} + 13L_2t_{2x_2} - 4L_3t_{1x_2} - 16L_3t_{2x_2}) \\ -\frac{b}{15}(7L_1t_{1x_1} + 3L_1t_{2x_1} - 3L_2t_{1x_1} - 7L_2t_{2x_1} - 4L_3t_{1x_1} + 4L_3t_{2x_1}) \\ -\frac{b}{15}(7L_1t_{1x_2} + 3L_1t_{2x_2} - 3L_2t_{1x_2} - 7L_2t_{2x_2} - 4L_3t_{1x_2} + 4L_3t_{2x_2}) \end{array} \right\}. \quad (5.16)$$

The expressions above give the consistent FEM nodal loads for each node along the FSI interface as a function of the tractions imposed by the fluid domain.

5.4.2 FSI Interface Coupling Scheme

It is known that partitioned FSI system solvers may be unstable for certain strongly-coupled problems [12]. The 1D piston-channel problem described in the next chapter constitutes a good example of such a case [1,12]. To ensure stability without any additional computational overhead, a new interface coupling scheme is therefore proposed. The scheme is based on the fact that within each iteration in pseudo-time, the fluid passes forces to the solid which causes it to displace or deform based on the solid governing equations and without any consideration of the fluid domain. If the forces are large or the density of the solid low, this may render the system unstable. If instead the forces from the fluid domain are projected forward based on the inertia of the fluid, the solid will deform accordingly and the fluid-solid system remains stable. The projection of the fluid force in pseudo-time is stated mathematically as

$$F_i^{\tau+\Delta\tau} = F_i^\tau + \left. \frac{dF}{da} \right|_i^\tau \Delta a_i, \quad (5.17)$$

where F_i is the applied force on any arbitrary solid node along the FSI interface and a_i is the acceleration. Note that since the solution is driven to pseudo-steady state, $F_i^{\tau+\Delta\tau} = F_i^\tau$ upon convergence and the projected term is nullified.

The term $\left. \frac{dF}{da} \right|_i$ represents the inertia of the fluid and can be approximated numerically as

$$\left. \frac{dF}{da} \right|_i^\tau \approx \frac{F_i^{\tau-\Delta\tau} - F_i^{\tau-2\Delta\tau}}{a_i^{\tau-\Delta\tau} - a_i^{\tau-2\Delta\tau}}. \quad (5.18)$$

Substituting Equation (5.18) into Equation (5.17) and expanding gives:

$$F_i^{\tau+\Delta\tau} \approx F_i^\tau + \frac{F_i^{\tau-\Delta\tau} - F_i^{\tau-2\Delta\tau}}{a_i^{\tau-\Delta\tau} - a_i^{\tau-2\Delta\tau}} (a_i^{\tau+\Delta\tau} - a_i^\tau) \quad (5.19)$$

$$\approx F_i^\tau + \frac{F_i^{\tau-\Delta\tau} - F_i^{\tau-2\Delta\tau}}{a_i^{\tau-\Delta\tau} - a_i^{\tau-2\Delta\tau}} \left(\frac{v_i^{\tau+\Delta\tau} - v_i^n}{\Delta t} - \frac{v_i^\tau - v_i^n}{\Delta t} \right) \quad (5.20)$$

where v_i is the velocity of the node in the i -direction.

The velocity $v_i^{\tau+\Delta\tau}$ in Equation (5.20) is the value being solved for in the current pseudo-timestep. Therefore, following from Equation (3.88):

$$\sum_e [M_e]_{Q8_{\text{lumped}}} \frac{\{v_i\}^{\tau+\Delta\tau} - \{v_i\}^\tau}{\Delta\tau} \approx \{F_i\}^{\tau+\Delta\tau} - \sum_e \left(\sum_{\text{Gauss pts}} [B]^T \{P\} \det(\mathbf{J}) W_{GP} \right) - \sum_e [M_e]_{Q8_{\text{cons}}} \frac{3\{v_i\}^{\tau+\Delta\tau} - 4\{v_i\}^n + \{v_i\}^{n-1}}{2\Delta t}. \quad (5.21)$$

Now, substituting Equation (5.20) for the force gives:

$$\sum_e [M_e]_{Q8_{\text{lumped}}} \frac{\{v_i\}^{\tau+\Delta\tau} - \{v_i\}^\tau}{\Delta\tau} \approx \{F_i\}^\tau + \frac{\{F_i\}^{\tau-\Delta\tau} - \{F_i\}^{\tau-2\Delta\tau}}{\{a_i\}^{\tau-\Delta\tau} - \{a_i\}^{\tau-2\Delta\tau}} \left(\frac{\{v_i\}^{\tau+\Delta\tau} - \{v_i\}^\tau}{\Delta t} \right) - \sum_e \left(\sum_{\text{Gauss pts}} [B]^T \{P\} \det(\mathbf{J}) W_{GP} \right) - \sum_e [M_e]_{Q8_{\text{cons}}} \frac{3\{v_i\}^{\tau+\Delta\tau} - 4\{v_i\}^n + \{v_i\}^{n-1}}{2\Delta t}, \quad (5.22)$$

where $\{\bullet\}$ indicates a vector containing components of that variable within an element.

Equation (5.22) is re-arranged to solve for the velocity $v_i^{\tau+\Delta\tau}$ in an explicit fashion. This proposed interface coupling scheme requires little additional computational overhead, and is evaluated on the 1D piston-channel system in Chapter 6.

5.5 Parallelisation

The edge-based matrix-free numerical method lends itself easily to the use of distributed memory parallel hardware architectures. For this purpose, the mesh is decomposed into a number of subdomains for parallel operation. Since the solution procedure is an edge-based one, the number of edges in each subdomain is of a similar magnitude. The METIS library [67] is used for domain decomposition. One layer of overlapping or ghost nodes is needed for transferring information between subdomains. For edges that lie on the boundaries of the subdomains, the ghost nodes are treated as slave nodes, the values on which are updated from their corresponding master nodes in the neighbouring domain. Message Passing Interface (MPI) is used to communicate data between domains.

5.6 Mesh Movement and Solution Procedure

The movement of the fluid mesh is handled via an interpolation procedure. In this approach the closest internal and external boundary nodes for every internal fluid node are identified and the distances between the boundary nodes and the

internal node computed at the beginning of the analysis. The movement of internal fluid nodes is then determined by means of an interpolation function that uses the displacements of the closest boundary nodes. The reader is referred to [17] for further details.

The solution procedure for the coupled FSI problem involves solving the discretised fluid and solid governing equations and updating the mesh in an iterative manner that effects strong coupling, as follows:

1. The fluid governing equations, Equations (5.1) to (5.3), are solved for an iteration. This solution provides tractions that are applied to the solid domain.
2. The solid discrete equations, Equations (3.84) and (3.92), are then solved for an iteration, which provides velocities and displacements at the boundary of the FSI interface. The boundary velocities are applied to the fluid mesh, which results in an ALE convective velocity in the fluid domain.
3. The mesh is moved if the displacement of a solid mesh boundary node exceeds 30% of the element size or the residuals of the fluid and solid discrete equations have decreased by at least four orders of magnitude.
4. The steps above are repeated until convergence, i.e. the residuals of fluid and solid discrete equations are calculated and if greater than the convergence tolerance, Steps 1 to 3 are repeated. If the residuals have decreased by at least five orders of magnitude, the real-timestep is terminated and the next timestep is entered by proceeding to Step 1.

5.7 Conclusion

In this chapter, a partitioned hybrid finite volume–finite element fluid-structure interaction scheme for strongly-coupled problems was developed. The governing equation set and constitutive relations that describe a viscous, incompressible fluid were presented. The transfer of information between the fluid and solid domains, including the coupling of the Q8 solid elements with the finite volume fluid elements, was described in detail. Parallelisation of the solver was explained. Finally, mesh movement and a solution procedure that effects strong coupling between the fluid and solid domains were detailed.

Chapter 6

Fluid-Structure Interaction: Validation and Verification

6.1 Introduction

In this chapter, the developed FSI technology is evaluated on three strongly-coupled benchmark problems. In the first example, a 1D piston-channel system with a varying fluid domain is studied. The second example considers an elastic beam in the wake of a square block undergoing vortex-induced vibration in its second mode. Finally, the same block-tail geometry as the previous case but with the beam oscillating in its first mode of vibration is analysed. Solutions are considered converged if the residuals decrease by at least five orders of magnitude. Results are compared with those published in literature as well as analytical solutions where available.

6.2 Dynamic Piston-channel System

The first test-case considered was that of a piston-channel system with a varying fluid domain. The system geometry and boundary conditions are described in Figure 6.1. The channel is 11 m long and is partially filled with an inviscid incompressible fluid with an elastic piston situated to its left. A prescribed velocity, $v(t)$, was imposed on the piston, which pushes the fluid out of the domain. A zero pressure boundary condition was imposed at the outflow boundary and slip boundary conditions were imposed along all the channel walls. The piston has a Young's modulus of $E = 10$ Pa and density and Poisson's ratio of zero. A linear elastic solid model was used for this problem for comparison with others [1]. The fluid has a density $\rho_f = 1$ kg m⁻³.

This problem was chosen as the coupling between the fluid and solid domain is strong and partitioned FSI solution schemes usually diverge for such a problem, even with large under-relaxation [1, 12]. This would test the partitioned

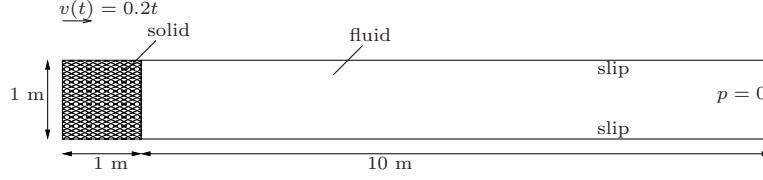


Figure 6.1: Geometry and boundary conditions for the piston-channel system

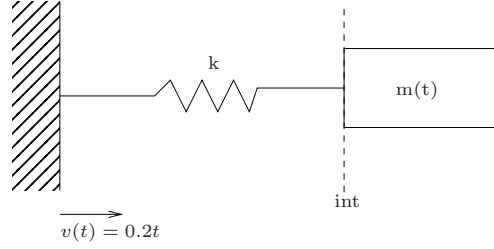


Figure 6.2: Representative spring-mass system for the piston-channel configuration

FSI interface coupling scheme proposed in the previous chapter. An analytical solution exists for this system, which can be considered as a simple 1D problem.

To obtain an analytical expression for the displacement and velocity of the interface, the system can be treated as a 1D spring-mass system, as shown in Figure 6.2. The elastic piston acts as a linear spring and the incompressible fluid as a variable mass [1]. Applying a balance of forces at the interface gives:

$$F_{\text{spring}} + F_{\text{mass}} = 0 \quad (6.1)$$

therefore,

$$k(u_{\text{int}} - u(t)) = -m \frac{dv_{\text{int}}}{dt} \quad (6.2)$$

where F_{spring} and F_{mass} are the forces exerted by the spring and mass, u_{int} and v_{int} are the displacement and velocity of the interface, $u(t)$ is the prescribed displacement of the left wall, k is the equivalent spring constant and m is the mass of the fluid. Substituting the properties of the piston and fluid for the spring and mass respectively, yield the following expressions for the velocity and displacement at the interface of the system:

$$\frac{dv_{\text{int}}}{dt} = \frac{10(u_{\text{int}} - 0.1t^2)}{(u_{\text{int}} - 10)} \quad (6.3)$$

$$\frac{du_{\text{int}}}{dt} = v_{\text{int}}. \quad (6.4)$$

The solid domain is discretised using a single Q8 element and the fluid domain using three cells. The resulting computed time history of the displacement and velocity of the interface are shown in Figure 6.3. As can be seen, the FSI scheme was able to predict the exact solution. Figure 6.4 shows the results obtained using different meshes for the fluid and solid domain, i.e. one solid and ten fluid cells (1×10), one solid and twenty fluid cells (1×20), and five solid and ten fluid cells (5×10). This demonstrates stability and robustness in the scheme.

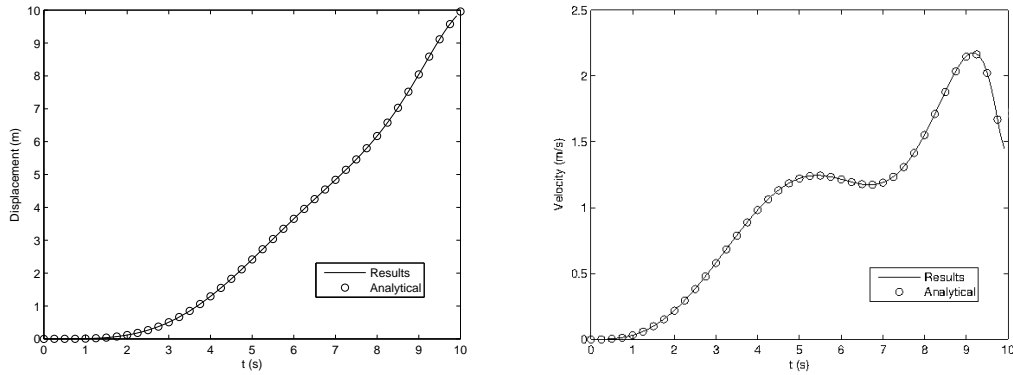


Figure 6.3: Displacement (left) and velocity (right) of the interface of the piston and channel

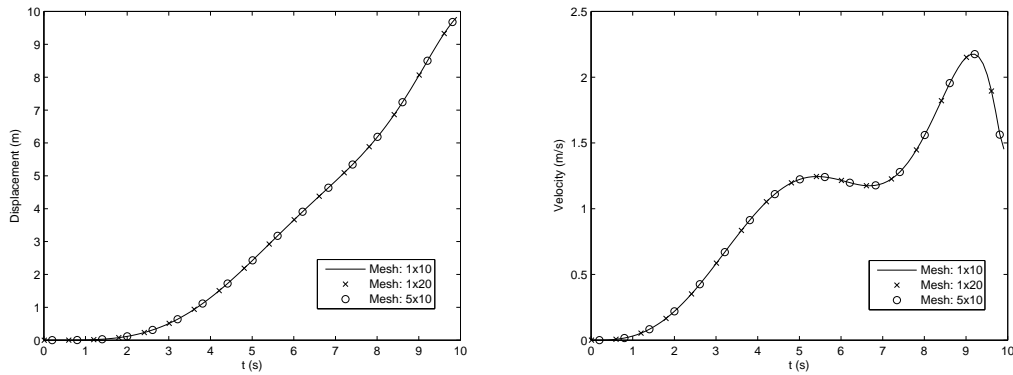


Figure 6.4: Displacement (left) and velocity (right) of the interface of the piston-channel using various meshes

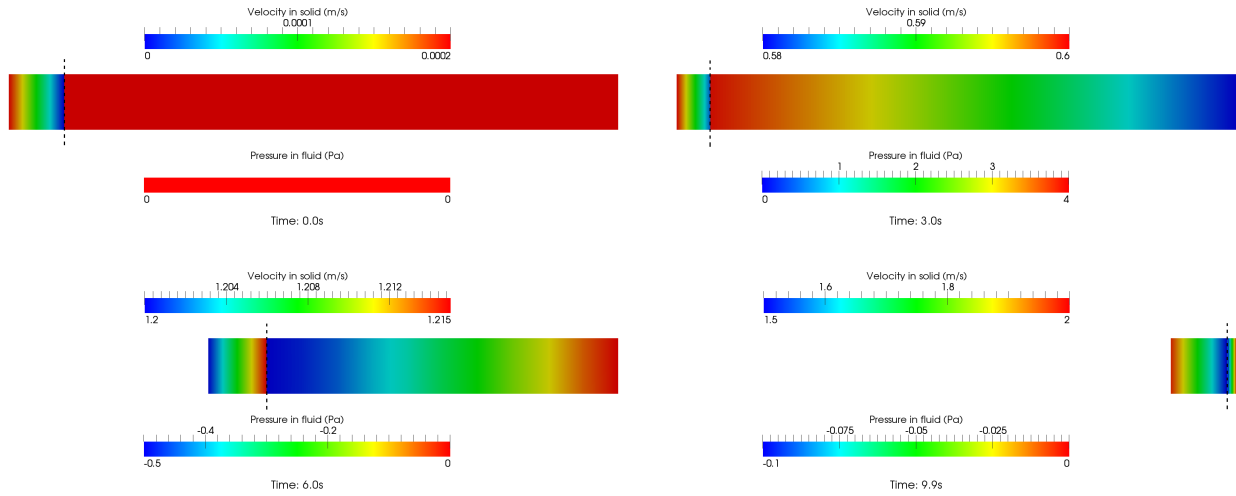


Figure 6.5: Velocity contours of the piston and pressure contours of the fluid at various times

Velocity contours of the solid and pressure contours of the fluid at various times are shown in Figure 6.5. The velocity field is linear in the solid, while the pressure field is linear in the fluid. A second-order accurate scheme is thus able to predict the solution exactly.

6.3 Block-tail in Second Mode of Vibration

The second test-case considered was that of an elastic beam in the wake of a rigid square block. This is a popular FSI benchmark test-case that was first proposed by Wall [68] and studied by many other researchers [1, 10, 14, 39]. The geometry and boundary conditions are shown in Figure 6.6. The properties of the incompressible fluid are: density $\rho_f = 1.18 \times 10^{-3} \text{ g cm}^{-3}$ and viscosity $\mu_f = 1.82 \times 10^{-4} \text{ g cm}^{-1} \text{ s}^{-1}$, while that of the beam are: density $\rho_s = 2.0 \text{ g cm}^{-3}$, Young's modulus $E = 2.0 \times 10^6 \text{ g cm}^{-1} \text{ s}^{-2}$ and Poisson's ratio $\nu = 0.35$. The plane stress assumption was used. A uniform constant fluid velocity, $v_{in} = 31.5 \text{ cm s}^{-1}$, or Reynolds number, $Re = \frac{\rho_f L v_{in}}{\mu_f} = 204$, was applied at the inlet while at the exit the pressure was set to zero. The artificial projection term, as described in the previous chapter, was not necessary for this problem.

The fluid domain was discretised into an unstructured triangular mesh consisting of approximately 6 000 elements as shown in Figures 6.7(a) and 6.7(b). The solid was discretised using a single layer of 40 Q8 elements. Plots of the deformed mesh that results from the oscillations of the beam are shown in Figures 6.7(c) and 6.7(d).

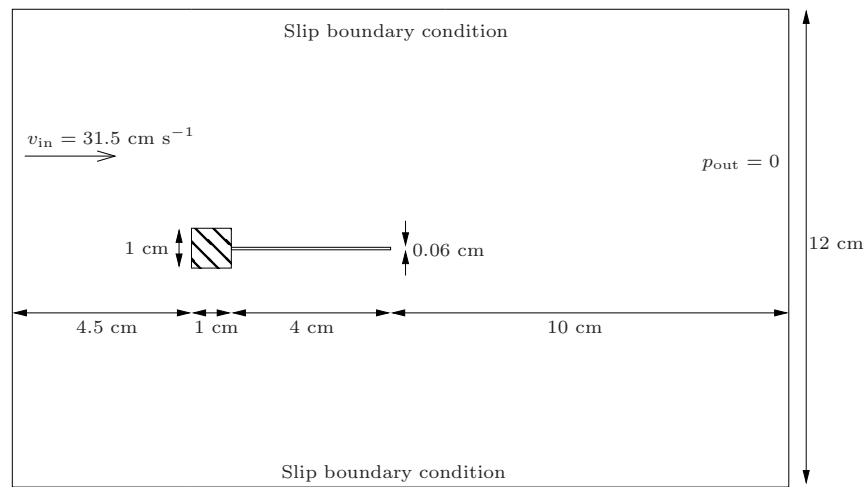


Figure 6.6: Geometry and boundary conditions for the block-tail FSI test-case

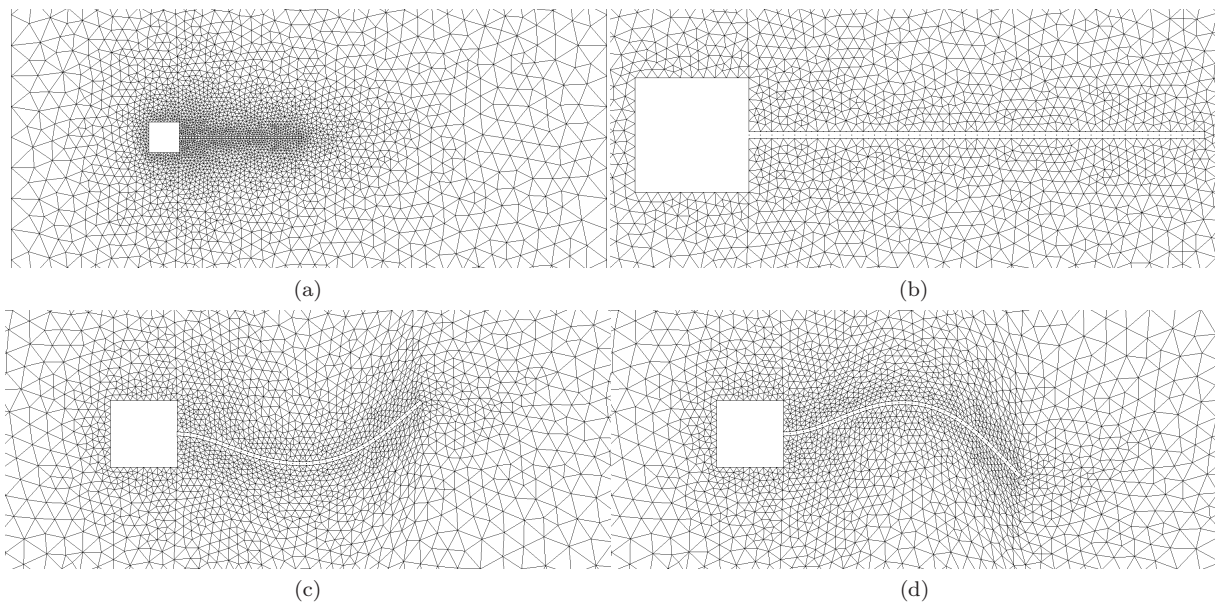


Figure 6.7: Block-tail test-case: (a) and (b) 6 000 element fluid mesh. (c) and (d) Plots of the deformed mesh

The inlet velocity results in vortices that are shed from the corners of the block periodically at a frequency of 3.7 Hz, which is close to the second natural frequency of the beam of 3.8 Hz. The fluid passes over the beam as symmetric vortices develop on either side of it. The symmetry of the vortices breaks, which results in uneven forces on the beam inducing vibrations of small amplitude. The oscillation of the beam results in further disturbance of the flow, which in turn induces larger displacements of the beam. Within each period, two vortices develop on one side of the beam while a larger vortex develops on the other side, as shown in Figure 6.8. The system builds up to large oscillations of the beam in its second mode of vibration as vortices are shed periodically from either side of it.

The time history of the tip displacement of the beam is plotted in Figure 6.9(a), together with the results of Hubner et al. [1]. There is a good

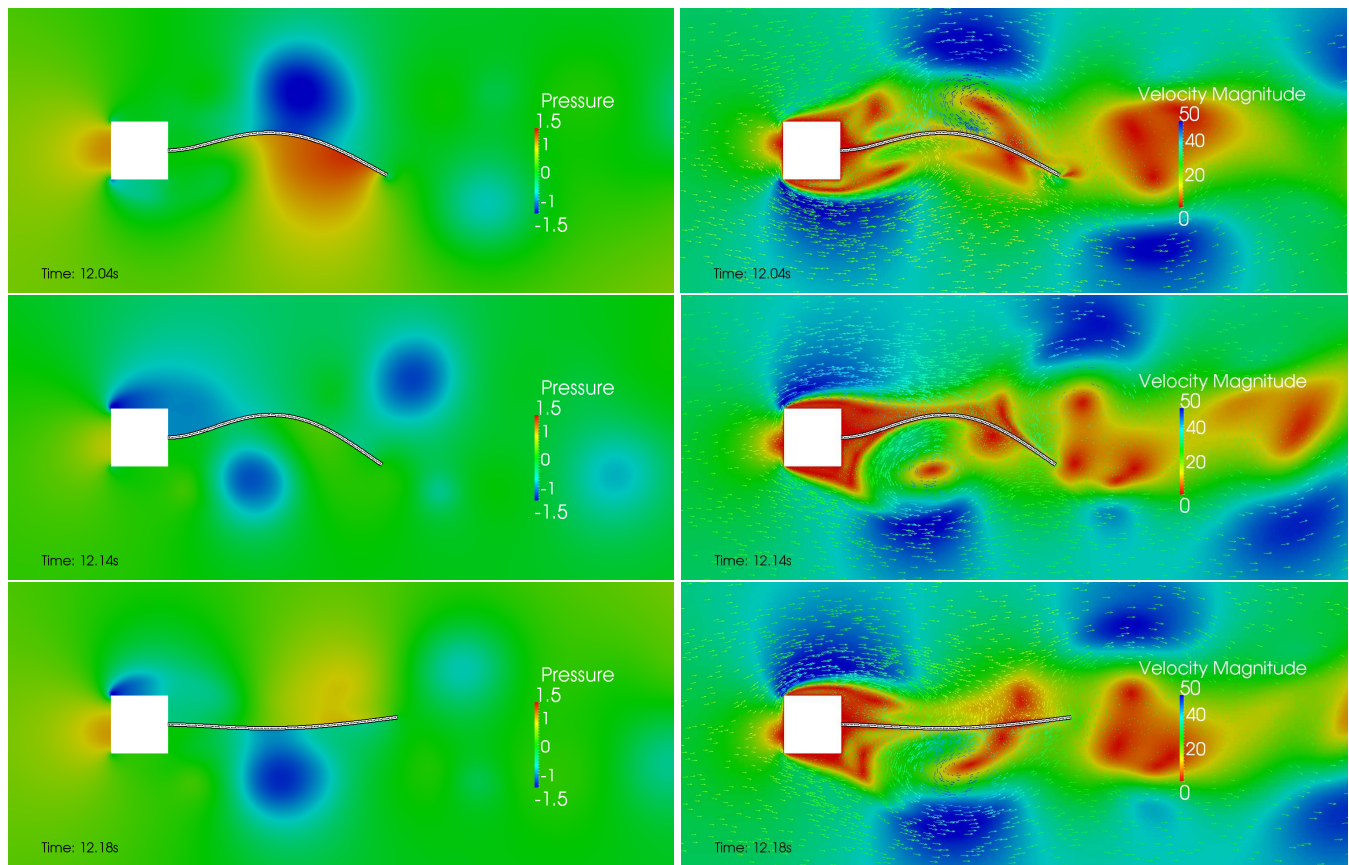


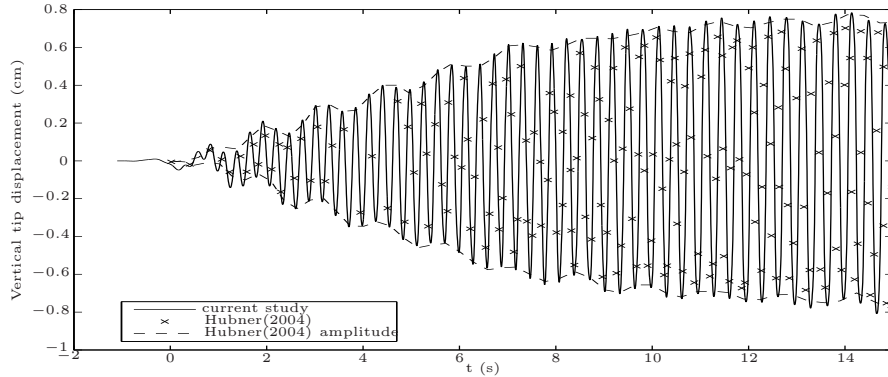
Figure 6.8: Pressure (left) and velocity contours (right) for the block-tail test-case with the beam oscillating in its second mode of vibration

correlation between the two sets of results, with the amplitude and frequency differing by less than 3% and 4% respectively as shown in Table 6.1. A rigorous mesh and temporal independence study was conducted. To evaluate mesh independence of the fluid two finer meshes of 25 000 and 50 000 fluid elements were generated (shown in Figure 6.10). As can be seen in Figure 6.9(b) and Table 6.1, a small change in solution is observed from the 6 000 to the 25 000 element mesh, but a further doubling of the number of elements results in a negligible difference. Next, to evaluate mesh independence of the solid a finer solid mesh of 80×2 Q8 elements was used and it was found that the results are identical to the 40×1 solid mesh case (see Figure 6.9(c) and Table 6.1). Finally, temporal independence was evaluated by using four different timestep sizes varying from 0.005s to 0.0005s. The time history in Figure 6.9(d) as well as the result in Table 6.1 show good convergence and independence in the results.

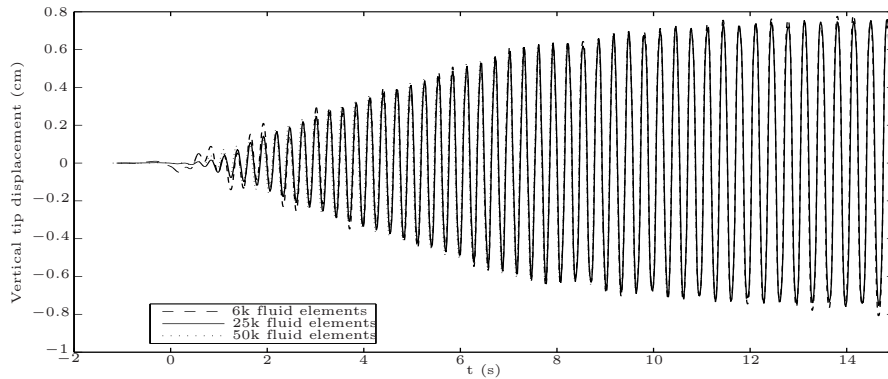
An evaluation of the transfer of traction forces from the fluid to the solid domain was conducted. The fluid and solid elements line up at the fluid-structure interface. However, since the Q8 element contains an additional node at the mid-point of every edge there is an additional unconnected solid node at the FSI interface. This complicates the transfer of the traction forces: either the traction at every fluid node on the interface is transferred to the corresponding solid node, which will satisfy a global balance of force, or FEM nodal loads, as described in the previous chapter and which are consistent with the finite element method, are calculated and the traction distributed to every solid node at the interface. Both approaches were implemented and a comparison of the tip displacement is shown in Figure 6.11. There is a negligible change in result and for practical purposes a simple transfer of traction from every fluid node to the corresponding solid node on the interface is sufficient, if structural stresses on the interface are not of primary concern.

Fluid mesh	Solid mesh	Timestep (s)	Amplitude (cm)	Frequency (Hz)
6 000	40×1	0.001	0.78	2.98
6 000	80×2	0.001	0.78	2.98
25 000	120×1	0.001	0.76	2.97
50 000	160×1	0.001	0.76	2.97
6 000	40×1	0.0005	0.78	2.97
Hubner et al. [1]			0.8	3.1
Xia et al. [14]			0.81	3.3

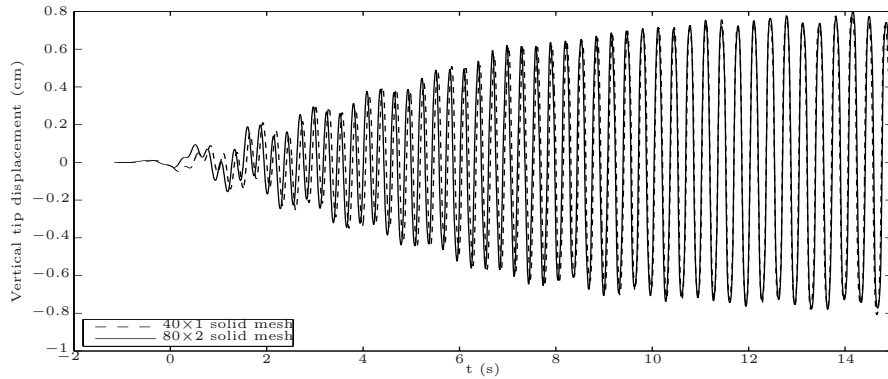
Table 6.1: Comparison of amplitude and frequency for the block-tail test-case in second mode of vibration with various meshes and timestep sizes



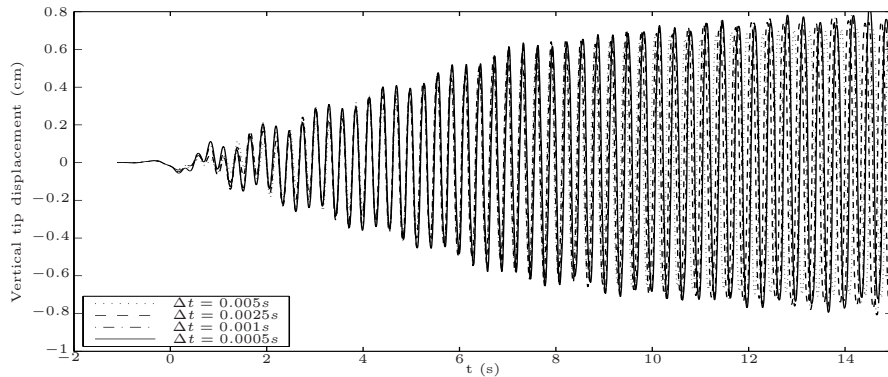
(a)



(b)



(c)



(d)

Figure 6.9: Tip displacement for the block-tail test-case in second mode of vibration with various meshes and timestep sizes

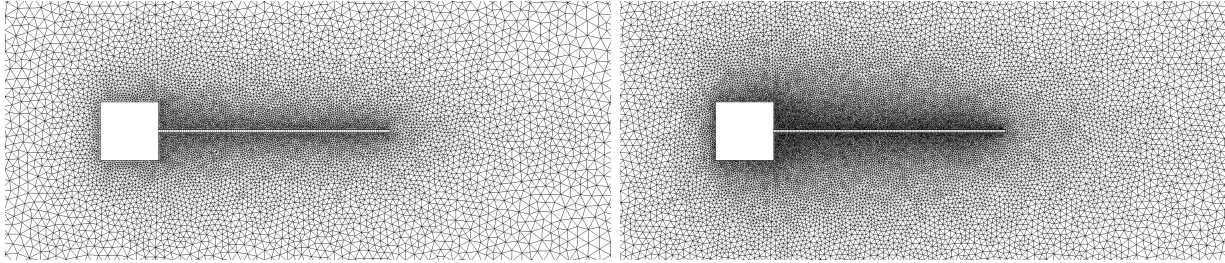


Figure 6.10: Block-tail test-case: 25 000 (left) and 50 000 cell (right) fluid mesh

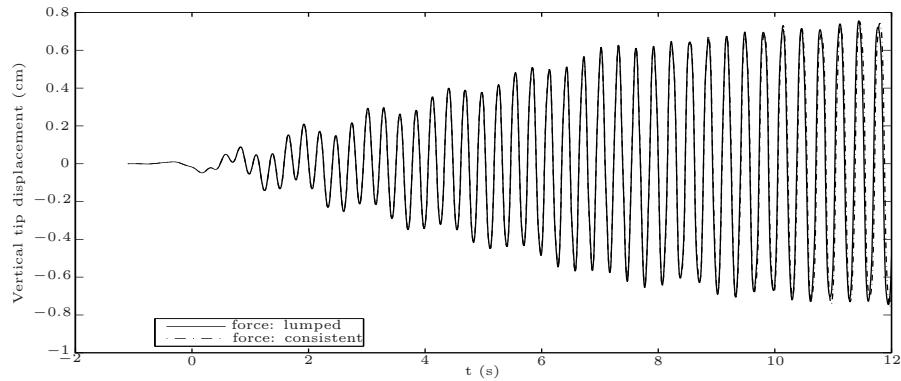


Figure 6.11: Tip displacement for the block-tail test-case in second mode of vibration using consistent and lumped traction forces at the interface

6.4 Block-tail in First Mode of Vibration

In the final test-case, the same block-tail geometry as above was considered but the beam was given an initial deflection due to a temporary load and the plane strain assumption was used. This problem was considered by Hubner et al. [1]. In order to fit the initial deflection of the beam as shown in [1], the piecewise-constant tip-load as a function of time was determined empirically and is shown in Table 6.2. The behaviour of the system changes significantly as large-amplitude oscillations of the beam occur in its first mode of vibration. The amplitude is more than twice that of the previous example and plots of the deformed mesh are shown in Figure 6.12.

The large deflection of the beam causes a vortex to develop on the opposite side of the deflection. This vortex moves along the beam and breaks away as the beam reaches its maximum deflection. As the beam moves in the other direction, a smaller vortex of opposite rotation develops at its tip and also breaks away. Plots of the pressure and velocity contours are shown in Figure 6.13.

The tip displacement of the beam is compared with the results of Hubner et al. [1] in Figure 6.14(a). There is a difference in the initial response, but the results compare well as the limit-cycle is reached. A comparison of the results using three fluid meshes of 6 000, 25 000 and 50 000 elements is shown in Figure 6.14(b). There is a significant change in the solution from the 6 000 to the 25 000 element mesh, but negligible change between the 25 000 and 50 000 element mesh. A refinement in the solid mesh has no effect on the result, as shown in Figure 6.14(c). An evaluation of the results using four different timestep sizes again shows good temporal independence of the solution (see Figure 6.14(d)). A comparison of the frequency and amplitude for different meshes and timestep sizes is shown in Table 6.3.

Time (s):	0–0.1	0.1–0.15	0.15–0.2	0.2–0.3	0.3–0.4	0.4–0.5	0.5–0.6
Force (g cm s ⁻²):	0	0.35	1.5	2.3	3.1	4.2	6.5
Time (s):	0.6–0.7	0.7–0.8	0.8–0.9	0.9–1.0	1.0–1.1	1.1–1.2	1.2–1.3
Force (g cm s ⁻²):	6.5	5.5	5.0	4.0	3.0	2.0	1.0

Table 6.2: Piecewise-constant force as a function of time applied to tip of beam to reproduce initial deflection in results of [1].

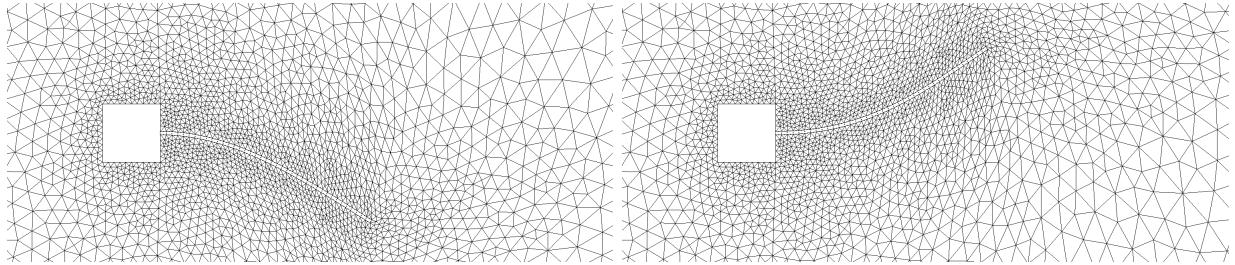


Figure 6.12: Block-tail test-case: Plots of the deformed mesh with the beam oscillating in its first mode of vibration

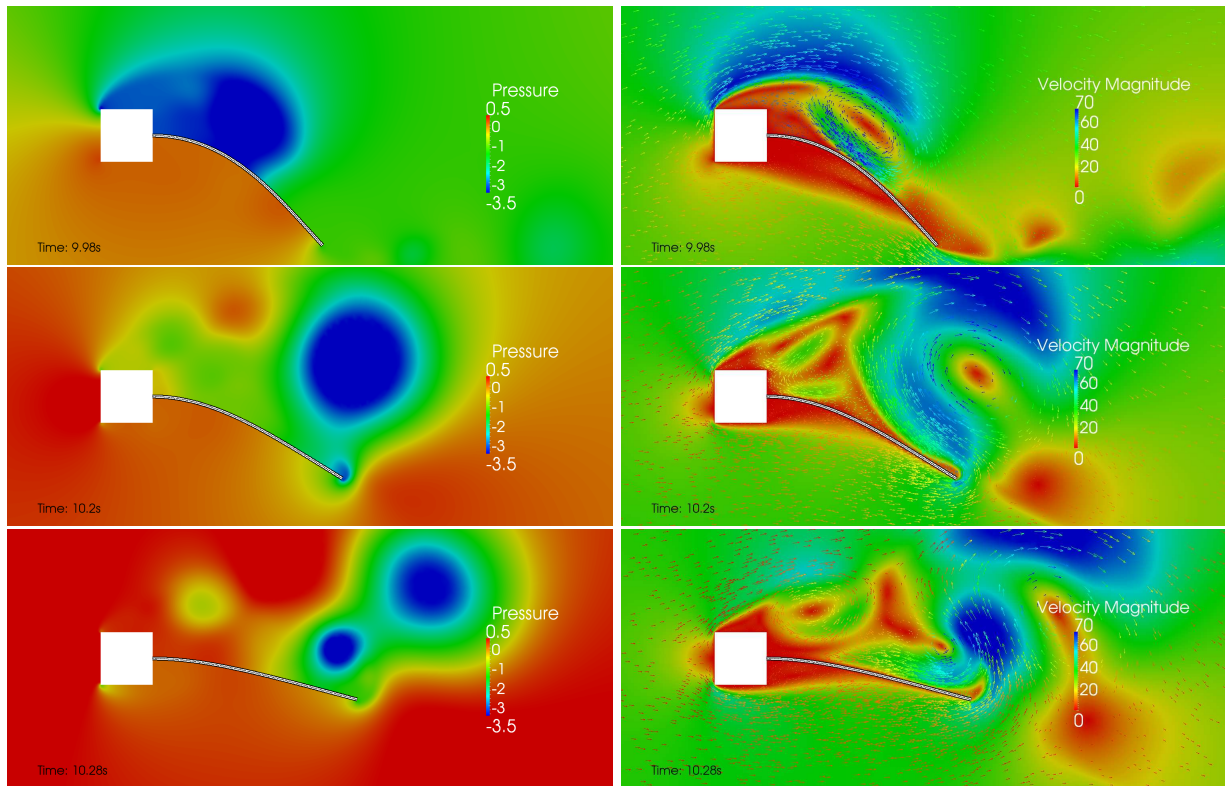


Figure 6.13: Pressure (left) and velocity contours (right) for the block-tail test-case with the beam oscillating in its first mode of vibration

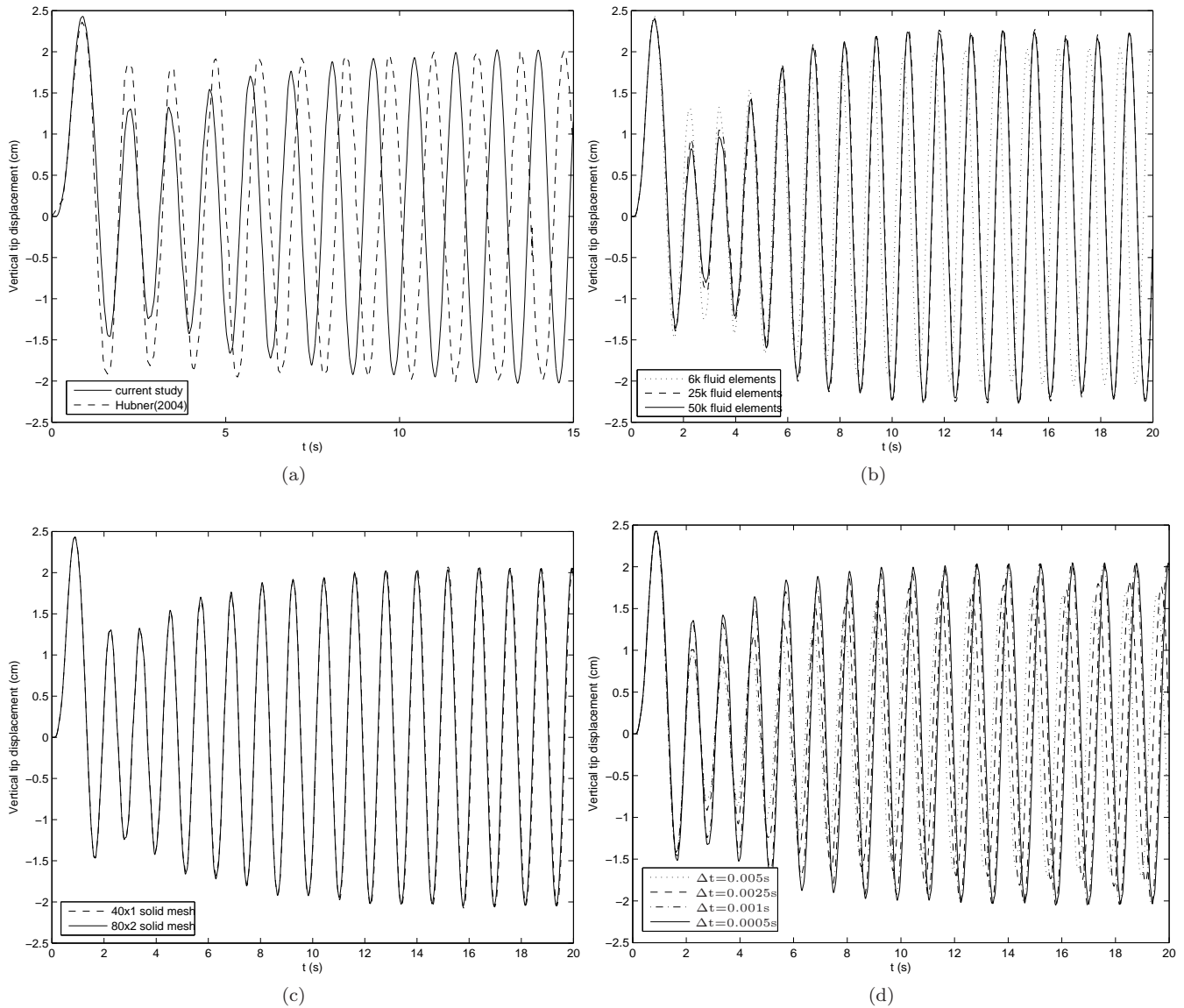


Figure 6.14: Tip displacement for the block-tail test-case in first mode of vibration with various meshes and timestep sizes

Fluid mesh	Solid mesh	Timestep (s)	Amplitude (cm)	Frequency (Hz)
6 000	40×1	0.001	2.04	0.84
6 000	80×2	0.001	2.04	0.84
25 000	120×1	0.001	2.17	0.83
50 000	160×1	0.001	2.18	0.82
6 000	40×1	0.0005	2.04	0.84
Hubner et al. [1]			2.0	0.8

Table 6.3: Comparison of amplitude and frequency for the block-tail test-case in first mode of vibration with various meshes and timestep sizes

6.5 Conclusion

The hybrid finite volume-finite element FSI scheme was tested on three strongly-coupled benchmark FSI test-cases. In all cases the scheme produced accurate results that compared well with that published in literature. Temporal and mesh independence were evaluated and demonstrated stability and robustness in the scheme.

Chapter 7

Conclusions and Future Work

7.1 Consolidation of Work Performed

The aim of this project was to develop an in-house computational tool that can accurately model strongly-coupled fluid-structure interaction problems, with a particular focus on thin-walled structures undergoing large, non-linear deformations.

The first objective was to improve the efficiency with which *Elemental* models thin structures in bending. The finite element method of discretisation is traditionally more common for computational solid mechanics, but the finite volume method is receiving increased attention for this purpose and both methods were evaluated for this purpose. With regards to the former, linear Q4 and higher-order Q8 finite element methods were implemented. For the latter, a standard vertex-centred and recently developed hybrid finite volume method were implemented. An in-depth error analysis was conducted on these two formulations from which a new higher-order finite volume method was developed. The accuracy of each formulation was compared via application to a number of test problems. It was shown that both the vertex-centred finite volume method and Q4 finite element method suffer from shear locking or sensitivity to element aspect ratio. The structure becomes stiffer as the aspect ratio is increased. The shear locking mechanism is overcome by the hybrid approach, but many elements are required through the thickness to ensure accuracy. The higher-order finite volume method provided accurate results with relatively coarse meshes, but the Q8 finite element method produced the most desirable results and was chosen as the preferred method for modelling the structural domain.

In the second part of this work, a partitioned hybrid finite volume–finite element fluid-structure interaction scheme for strongly-coupled problems was developed. The physical domain consisted of a homogeneous isotropic elastic solid region and a viscous incompressible isothermal fluid domain, the former

discretised using an isoparametric Q8 finite element methodology and the latter using an edge-based hybrid-unstructured vertex-centred finite volume methodology. A dual-timestepping procedure was employed in a way that both the fluid and structural domain are fully or strongly-coupled at solver sub-iteration level. The transfer of information between the fluid and solid domains, including the coupling of the Q8 solid elements with the finite volume fluid elements and a fluid-solid interface coupling algorithm, was described in detail. The solver was parallelised for distributed memory parallel hardware architectures and movement of the fluid mesh was handled via an interpolation procedure. The developed hybrid finite volume-finite element FSI scheme was validated successfully on three strongly-coupled benchmark FSI test-cases. In all cases the scheme produced accurate results that compared well with that published in literature. Temporal and mesh independence were evaluated and demonstrated stability and robustness in the scheme.

7.2 Future Work

The scope of this study was limited to isotropic elastic structures and incompressible flows and applied to two-dimensional problems. Further work, building on this, is required to furnish a comprehensive industrial fluid-structure interaction code. Aspects meriting further investigation include:

- The application to 3D problems, which requires the extension of both the fluid and structural solver to a third spatial dimension.
- A stability analysis on the higher-order finite volume method and the establishment of higher-order finite volume techniques.
- An investigation into the use of shell theory for modelling the structural domain and its applicability to a certain class of problems.
- The extension of the fluid-structure interaction solver for a broader range of problems. This could include incorporating triangular and mixed finite elements to handle incompressibility or material non-linearity such as in biomedical applications. In addition, an extension of the fluid solver to handle transonic and compressible flows would extend its capability to capture shocks and increase its use in aerospace applications.

Appendix A

Error Analysis: Analytical Approach

In order to develop a higher-order finite volume formulation, a detailed error analysis was conducted analytically on both the vertex-centred and hybrid formulations. The detailed derivations are shown in this section.

To simplify the mathematical analysis yet still obtain a qualitative description of the error terms, the problem was limited to the small displacement case and a Poisson's ratio of zero was assumed. The governing equation is given by Equation (3.55):

$$\frac{\partial \sigma_{ij}}{\partial x_j} = 0. \quad (\text{A.1})$$

The stress-strain relationship is given by Equation (3.57):

$$\sigma_{ij} = E \varepsilon_{ij}. \quad (\text{A.2})$$

The strain-displacement relationship for the small displacement case is:

$$\varepsilon_{ij} = \frac{1}{2} \left(\frac{\partial u_i}{\partial x_j} + \frac{\partial u_j}{\partial x_i} \right). \quad (\text{A.3})$$

Substituting Equation (A.2) and Equation (A.3) into Equation (A.1) gives the governing equation expressed in terms of displacements:

$$\frac{E}{2} \left(\frac{\partial^2 u_i}{\partial x_j^2} + \frac{\partial^2 u_j}{\partial x_i \partial x_j} \right) = 0. \quad (\text{A.4})$$

The analytical expressions for the x_1 - and x_2 -momentum equations are therefore, respectively:

$$\frac{\partial \sigma_{11}}{\partial x_1} + \frac{\partial \sigma_{12}}{\partial x_2} = E \frac{\partial^2 u_1}{\partial x_1^2} + \frac{E}{2} \left(\frac{\partial^2 u_1}{\partial x_2^2} + \frac{\partial^2 u_2}{\partial x_1 \partial x_2} \right) = 0 \quad (\text{A.5})$$

$$\frac{\partial \sigma_{21}}{\partial x_1} + \frac{\partial \sigma_{22}}{\partial x_2} = E \frac{\partial^2 u_2}{\partial x_2^2} + \frac{E}{2} \left(\frac{\partial^2 u_2}{\partial x_1^2} + \frac{\partial^2 u_1}{\partial x_1 \partial x_2} \right) = 0 \quad (\text{A.6})$$

where the nomenclature is as previously defined.

We now develop the discrete expressions for the x_1 - and x_2 -momentum equations and expand each using Taylor series expansions. By comparing the analytical and expanded discrete expressions, the leading-order error terms are obtained. The discrete expressions differ for an internal, boundary and corner node and each case is considered separately below.

Internal Node - Vertex-centred FVM

Considering first the vertex-centred finite volume formulation for an internal node, Figure A.1.

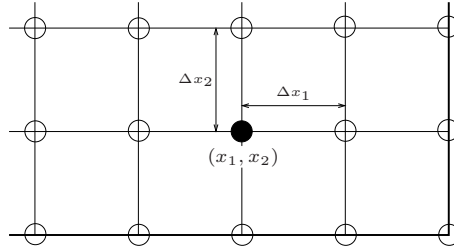


Figure A.1: Schematic of the mesh indicating an internal node

The partial derivatives of stress in the momentum equations, Equations (A.5) and (A.6), are computed as follows:

$$\frac{\partial \sigma_{11}}{\partial x_1} \approx \frac{\sigma_{11}(x_1 + \frac{1}{2}\Delta x_1, x_2) - \sigma_{11}(x_1 - \frac{1}{2}\Delta x_1, x_2)}{\Delta x_1} \quad (\text{A.7})$$

$$\frac{\partial \sigma_{12}}{\partial x_2} \approx \frac{\sigma_{12}(x_1, x_2 + \frac{1}{2}\Delta x_2) - \sigma_{12}(x_1, x_2 - \frac{1}{2}\Delta x_2)}{\Delta x_2} \quad (\text{A.8})$$

$$\frac{\partial \sigma_{21}}{\partial x_1} \approx \frac{\sigma_{21}(x_1 + \frac{1}{2}\Delta x_1, x_2) - \sigma_{21}(x_1 - \frac{1}{2}\Delta x_1, x_2)}{\Delta x_1} \quad (\text{A.9})$$

$$\frac{\partial \sigma_{22}}{\partial x_2} \approx \frac{\sigma_{22}(x_1, x_2 + \frac{1}{2}\Delta x_2) - \sigma_{22}(x_1, x_2 - \frac{1}{2}\Delta x_2)}{\Delta x_2}. \quad (\text{A.10})$$

Using the stress-strain relation, Equation (A.2), and the strain-displacement relationship, Equation (A.3), the stress terms are given by:

$$\sigma_{11}(x_1 + \frac{1}{2}\Delta x_1, x_2) = E \frac{\partial u_1}{\partial x_1} \Big|_{(x_1 + \frac{1}{2}\Delta x_1, x_2)} \quad (\text{A.11})$$

$$\sigma_{22}(x_1, x_2 + \frac{1}{2}\Delta x_2) = E \frac{\partial u_2}{\partial x_2} \Big|_{(x_1, x_2 + \frac{1}{2}\Delta x_2)} \quad (\text{A.12})$$

$$\sigma_{12}(x_1, x_2 + \frac{1}{2}\Delta x_2) = \frac{E}{2} \left(\frac{\partial u_1}{\partial x_2} + \frac{\partial u_2}{\partial x_1} \right) \Big|_{(x_1, x_2 + \frac{1}{2}\Delta x_2)} \quad (\text{A.13})$$

$$\sigma_{21}(x_1 + \frac{1}{2}\Delta x_1, x_2) = \frac{E}{2} \left(\frac{\partial u_2}{\partial x_1} + \frac{\partial u_1}{\partial x_2} \right) \Big|_{(x_1 + \frac{1}{2}\Delta x_1, x_2)} \quad (\text{A.14})$$

Finally, the displacement gradients for the vertex-centred finite volume formulation are computed from Equation (3.50) as:

$$\frac{\partial u_1}{\partial x_1} \Big|_{(x_1 + \frac{1}{2}\Delta x_1, x_2)} \approx \frac{u_1(x_1 + \Delta x_1, x_2) - u_1(x_1, x_2)}{\Delta x_1} \quad (\text{A.15})$$

$$\frac{\partial u_2}{\partial x_2} \Big|_{(x_1, x_2 + \frac{1}{2}\Delta x_2)} \approx \frac{u_2(x_1, x_2 + \Delta x_2) - u_2(x_1, x_2)}{\Delta x_2} \quad (\text{A.16})$$

$$\frac{\partial u_1}{\partial x_2} \Big|_{(x_1, x_2 + \frac{1}{2}\Delta x_2)} \approx \frac{u_1(x_1, x_2 + \Delta x_2) - u_1(x_1, x_2)}{\Delta x_2} \quad (\text{A.17})$$

$$\begin{aligned} \frac{\partial u_2}{\partial x_1} \Big|_{(x_1, x_2 + \frac{1}{2}\Delta x_2)} &\approx \frac{1}{2} \left(\frac{\partial u_2}{\partial x_1} \Big|_{(x_1, x_2 + \Delta x_2)} + \frac{\partial u_2}{\partial x_1} \Big|_{(x_1, x_2)} \right) \\ &\approx \frac{1}{4\Delta x_1} \left[u_2(x_1 + \Delta x_1, x_2 + \Delta x_2) + u_2(x_1 + \Delta x_1, x_2) \right. \\ &\quad \left. - u_2(x_1 - \Delta x_1, x_2 + \Delta x_2) - u_2(x_1 - \Delta x_1, x_2) \right] \quad (\text{A.18}) \end{aligned}$$

$$\begin{aligned} \frac{\partial u_1}{\partial x_2} \Big|_{(x_1 + \frac{1}{2}\Delta x_1, x_2)} &\approx \frac{1}{2} \left(\frac{\partial u_1}{\partial x_2} \Big|_{(x_1 + \Delta x_1, x_2)} + \frac{\partial u_1}{\partial x_2} \Big|_{(x_1, x_2)} \right) \\ &\approx \frac{1}{4\Delta x_2} \left[u_1(x_1 + \Delta x_1, x_2 + \Delta x_2) + u_1(x_1, x_2 + \Delta x_2) \right. \\ &\quad \left. - u_1(x_1 + \Delta x_1, x_2 - \Delta x_2) - u_1(x_1, x_2 - \Delta x_2) \right] \quad (\text{A.19}) \end{aligned}$$

$$\frac{\partial u_2}{\partial x_1} \Big|_{(x_1 + \frac{1}{2}\Delta x_1, x_2)} \approx \frac{u_2(x_1 + \Delta x_1, x_2) - u_2(x_1, x_2)}{\Delta x_1} \quad (\text{A.20})$$

Using the above expressions for the displacement gradients and stress terms, the discrete expressions for the x_1 - and x_2 -momentum equations are:

$$\begin{aligned} \frac{\partial \sigma_{11}}{\partial x_1} + \frac{\partial \sigma_{12}}{\partial x_2} \approx & \frac{E}{\Delta x_1} \left\{ \frac{u_1(x_1 + \Delta x_1, x_2) - 2u_1(x_1, x_2) + u_1(x_1 - \Delta x_1, x_2)}{\Delta x_1} \right\} \\ & + \frac{E}{2\Delta x_2} \left\{ \frac{u_1(x_1, x_2 + \Delta x_2) - 2u_1(x_1, x_2) + u_1(x_1, x_2 - \Delta x_2)}{\Delta x_2} \right. \\ & + \frac{u_2(x_1 + \Delta x_1, x_2 + \Delta x_2) - u_2(x_1 + \Delta x_1, x_2 - \Delta x_2)}{4\Delta x_1} \\ & \left. - \frac{u_2(x_1 - \Delta x_1, x_2 + \Delta x_2) + u_2(x_1 - \Delta x_1, x_2 - \Delta x_2)}{4\Delta x_1} \right\} \quad (\text{A.21}) \end{aligned}$$

$$\begin{aligned} \frac{\partial \sigma_{21}}{\partial x_1} + \frac{\partial \sigma_{22}}{\partial x_2} \approx & \frac{E}{\Delta x_2} \left\{ \frac{u_2(x_1, x_2 + \Delta x_2) - 2u_2(x_1, x_2) + u_2(x_1, x_2 - \Delta x_2)}{\Delta x_2} \right\} \\ & + \frac{E}{2\Delta x_1} \left\{ \frac{u_2(x_1 + \Delta x_1, x_2) - 2u_2(x_1, x_2) + u_2(x_1 - \Delta x_1, x_2)}{\Delta x_1} \right. \\ & + \frac{u_1(x_1 + \Delta x_1, x_2 + \Delta x_2) - u_1(x_1 + \Delta x_1, x_2 - \Delta x_2)}{4\Delta x_2} \\ & \left. - \frac{u_1(x_1 - \Delta x_1, x_2 + \Delta x_2) + u_1(x_1 - \Delta x_1, x_2 - \Delta x_2)}{4\Delta x_2} \right\}. \quad (\text{A.22}) \end{aligned}$$

Each of the displacement terms can be expanded using Taylor series expansions of u_1 and u_2 about the point (x_1, x_2) , for example for $u_1(x_1 + \Delta x_1, x_2 + \Delta x_2)$:

$$\begin{aligned} u_1(x_1 + \Delta x_1, x_2 + \Delta x_2) = & u_1 + \frac{\partial u_1}{\partial x_1} \Delta x_1 + \frac{\partial u_1}{\partial x_2} \Delta x_2 + \frac{1}{2} \frac{\partial^2 u_1}{\partial x_1^2} \Delta x_1^2 + \frac{1}{2} \frac{\partial^2 u_1}{\partial x_2^2} \Delta x_2^2 + \frac{\partial^2 u_1}{\partial x_1 \partial x_2} \Delta x_1 \Delta x_2 \\ & + \frac{1}{6} \frac{\partial^3 u_1}{\partial x_1^3} \Delta x_1^3 + \frac{1}{6} \frac{\partial^3 u_1}{\partial x_2^3} \Delta x_2^3 + \frac{1}{2} \frac{\partial^3 u_1}{\partial x_1^2 \partial x_2} \Delta x_1^2 \Delta x_2 + \frac{1}{2} \frac{\partial^3 u_1}{\partial x_1 \partial x_2^2} \Delta x_1 \Delta x_2^2 \\ & + \frac{1}{24} \frac{\partial^4 u_1}{\partial x_1^4} \Delta x_1^4 + \frac{1}{24} \frac{\partial^4 u_1}{\partial x_2^4} \Delta x_2^4 + \frac{1}{6} \frac{\partial^4 u_1}{\partial x_1^3 \partial x_2} \Delta x_1^3 \Delta x_2 \\ & + \frac{1}{4} \frac{\partial^4 u_1}{\partial x_1^2 \partial x_2^2} \Delta x_1^2 \Delta x_2^2 + \frac{1}{6} \frac{\partial^4 u_1}{\partial x_1 \partial x_2^3} \Delta x_1 \Delta x_2^3 + \dots \quad (\text{A.23}) \end{aligned}$$

Similarly, expanding all the displacement terms, substituting into the dis-

crete expressions for the x_1 - and x_2 -momentum equations and simplifying gives:

$$\begin{aligned} \frac{\partial \sigma_{11}}{\partial x_1} + \frac{\partial \sigma_{12}}{\partial x_2} &= E \left(\frac{\partial^2 u_1}{\partial x_1^2} + \frac{1}{12} \frac{\partial^4 u_1}{\partial x_1^4} \Delta x_1^2 \right) \\ &+ \frac{E}{2} \left(\frac{\partial^2 u_1}{\partial x_2^2} + \frac{\partial^2 u_2}{\partial x_1 \partial x_2} + \frac{1}{12} \frac{\partial^4 u_1}{\partial x_2^4} \Delta x_2^2 + \frac{1}{6} \frac{\partial^4 u_2}{\partial x_1^3 \partial x_2} \Delta x_1^2 + \frac{1}{6} \frac{\partial^4 u_2}{\partial x_1 \partial x_2^3} \Delta x_2^2 \right) + \dots \end{aligned} \quad (\text{A.24})$$

$$\begin{aligned} \frac{\partial \sigma_{21}}{\partial x_1} + \frac{\partial \sigma_{22}}{\partial x_2} &= E \left(\frac{\partial^2 u_2}{\partial x_2^2} + \frac{1}{12} \frac{\partial^4 u_2}{\partial x_2^4} \Delta x_2^2 \right) \\ &+ \frac{E}{2} \left(\frac{\partial^2 u_2}{\partial x_1^2} + \frac{\partial^2 u_1}{\partial x_1 \partial x_2} + \frac{1}{12} \frac{\partial^4 u_2}{\partial x_1^4} \Delta x_1^2 + \frac{1}{6} \frac{\partial^4 u_1}{\partial x_1^3 \partial x_2} \Delta x_1^2 + \frac{1}{6} \frac{\partial^4 u_1}{\partial x_1 \partial x_2^3} \Delta x_2^2 \right) + \dots \end{aligned} \quad (\text{A.25})$$

Comparing the discrete expressions for the x_1 - and x_2 -momentum equations, Equations (A.24) and (A.25), with the analytical expressions, Equations (A.5) and (A.6), gives the leading-order error term for the vertex-centred finite volume method at an internal node:

$$Error_i = \frac{E}{2} \left(\frac{1}{6} \frac{\partial^4 u_i}{\partial x_i^4} \Delta x_i^2 + \frac{1}{12} \frac{\partial^4 u_i}{\partial x_k^4} \Delta x_k^2 + \frac{1}{6} \frac{\partial^4 u_k}{\partial x_i^3 \partial x_k} \Delta x_i^2 + \frac{1}{6} \frac{\partial^4 u_k}{\partial x_i \partial x_k^3} \Delta x_k^2 \right) \quad (\text{A.26})$$

with

$$i = 1; k = 2 \quad \text{for the } x_1\text{-momentum equation}$$

$$i = 2; k = 1 \quad \text{for the } x_2\text{-momentum equation.}$$

Internal Node - Hybrid FVM

Consider again an internal node (Figure A.1), but with the hybrid finite volume formulation. This method uses the same node-based gradients as the vertex-centred formulation for the normal components of stress, but elemental-based gradients for the shear components. These elemental-based gradients are computed using Equation (3.53) as:

$$\begin{aligned} \left. \frac{\partial u_1}{\partial x_2} \right|_{(x_1, x_2 + \frac{1}{2} \Delta x_2)} &\approx \frac{1}{2} \left(\left. \frac{\partial u_1}{\partial x_2} \right|_{(x_1 + \frac{1}{2} \Delta x_1, x_2 + \frac{1}{2} \Delta x_2)} + \left. \frac{\partial u_1}{\partial x_2} \right|_{(x_1 - \frac{1}{2} \Delta x_1, x_2 + \frac{1}{2} \Delta x_2)} \right) \\ &\approx \frac{1}{4 \Delta x_2} \left[u_1(x_1 + \Delta x_1, x_2 + \Delta x_2) - u_1(x_1 + \Delta x_1, x_2) \right. \\ &\quad \left. + 2u_1(x_1, x_2 + \Delta x_2) - 2u_1(x_1, x_2) \right. \\ &\quad \left. + u_1(x_1 - \Delta x_1, x_2 + \Delta x_2) - u_1(x_1 - \Delta x_1, x_2) \right] \quad (\text{A.27}) \end{aligned}$$

$$\begin{aligned}
\left. \frac{\partial u_2}{\partial x_1} \right|_{(x_1, x_2 + \frac{1}{2}\Delta x_2)} &\approx \frac{1}{2} \left(\left. \frac{\partial u_2}{\partial x_1} \right|_{(x_1 + \frac{1}{2}\Delta x_1, x_2 + \frac{1}{2}\Delta x_2)} + \left. \frac{\partial u_2}{\partial x_1} \right|_{(x_1 - \frac{1}{2}\Delta x_1, x_2 + \frac{1}{2}\Delta x_2)} \right) \\
&\approx \frac{1}{4\Delta x_1} \left[u_2(x_1 + \Delta x_1, x_2 + \Delta x_2) + u_2(x_1 + \Delta x_1, x_2) \right. \\
&\quad \left. - u_2(x_1 - \Delta x_1, x_2 + \Delta x_2) - u_2(x_1 - \Delta x_1, x_2) \right] \quad (\text{A.28})
\end{aligned}$$

$$\begin{aligned}
\left. \frac{\partial u_1}{\partial x_2} \right|_{(x_1 + \frac{1}{2}\Delta x_1, x_2)} &\approx \frac{1}{2} \left(\left. \frac{\partial u_1}{\partial x_2} \right|_{(x_1 + \frac{1}{2}\Delta x_1, x_2 + \frac{1}{2}\Delta x_2)} + \left. \frac{\partial u_1}{\partial x_2} \right|_{(x_1 + \frac{1}{2}\Delta x_1, x_2 - \frac{1}{2}\Delta x_2)} \right) \\
&\approx \frac{1}{4\Delta x_2} \left[u_1(x_1 + \Delta x_1, x_2 + \Delta x_2) + u_1(x_1, x_2 + \Delta x_2) \right. \\
&\quad \left. - u_1(x_1 + \Delta x_1, x_2 - \Delta x_2) - u_1(x_1, x_2 - \Delta x_2) \right] \quad (\text{A.29})
\end{aligned}$$

$$\begin{aligned}
\left. \frac{\partial u_2}{\partial x_1} \right|_{(x_1 + \frac{1}{2}\Delta x_1, x_2)} &\approx \frac{1}{2} \left(\left. \frac{\partial u_2}{\partial x_1} \right|_{(x_1 + \frac{1}{2}\Delta x_1, x_2 + \frac{1}{2}\Delta x_2)} + \left. \frac{\partial u_2}{\partial x_1} \right|_{(x_1 + \frac{1}{2}\Delta x_1, x_2 - \frac{1}{2}\Delta x_2)} \right) \\
&\approx \frac{1}{4\Delta x_1} \left[u_2(x_1 + \Delta x_1, x_2 + \Delta x_2) - u_2(x_1, x_2 + \Delta x_2) \right. \\
&\quad + 2u_2(x_1 + \Delta x_1, x_2) - 2u_2(x_1, x_2) \\
&\quad \left. + u_2(x_1 + \Delta x_1, x_2 - \Delta x_2) - u_2(x_1, x_2 - \Delta x_2) \right]. \quad (\text{A.30})
\end{aligned}$$

Substituting these expressions for the displacement gradients gives the following discrete expressions for the for the x_1 - and x_2 -momentum equations:

$$\begin{aligned}
\frac{\partial \sigma_{11}}{\partial x_1} + \frac{\partial \sigma_{12}}{\partial x_2} &\approx \frac{E}{\Delta x_1} \left\{ \frac{u_1(x_1 + \Delta x_1, x_2) - 2u_1(x_1, x_2) + u_1(x_1 - \Delta x_1, x_2)}{\Delta x_1} \right\} + \\
\frac{E}{4\Delta x_2} &\left\{ \frac{u_1(x_1 + \Delta x_1, x_2 + \Delta x_2) + 2u_1(x_1, x_2 + \Delta x_2) + u_1(x_1 - \Delta x_1, x_2 + \Delta x_2)}{2\Delta x_2} \right. \\
&- \frac{2u_1(x_1 + \Delta x_1, x_2) - 4u_1(x_1, x_2) - 2u_1(x_1 - \Delta x_1, x_2) + 2u_1(x_1, x_2 - \Delta x_2)}{2\Delta x_2} \\
&+ \frac{u_1(x_1 + \Delta x_1, x_2 - \Delta x_2) + u_1(x_1 - \Delta x_1, x_2 - \Delta x_2)}{2\Delta x_2} \\
&+ \frac{u_2(x_1 + \Delta x_1, x_2 + \Delta x_2) - u_2(x_1 - \Delta x_1, x_2 + \Delta x_2)}{2\Delta x_1} \\
&\left. - \frac{u_2(x_1 + \Delta x_1, x_2 - \Delta x_2) + u_2(x_1 - \Delta x_1, x_2 - \Delta x_2)}{2\Delta x_1} \right\} \quad (\text{A.31})
\end{aligned}$$

$$\begin{aligned}
\frac{\partial \sigma_{21}}{\partial x_1} + \frac{\partial \sigma_{22}}{\partial x_2} &\approx \frac{E}{\Delta x_2} \left\{ \frac{u_2(x_1, x_2 + \Delta x_2) - 2u_2(x_1, x_2) + u_2(x_1, x_2 - \Delta x_2)}{\Delta x_2} \right\} + \\
\frac{E}{4\Delta x_1} &\left\{ \frac{u_2(x_1 + \Delta x_1, x_2 + \Delta x_2) + 2u_2(x_1, x_2 + \Delta x_2) + u_2(x_1 + \Delta x_1, x_2 - \Delta x_2)}{2\Delta x_2} \right. \\
&- \frac{2u_2(x_1, x_2 + \Delta x_2) - 4u_2(x_1, x_2) - 2u_2(x_1, x_2 - \Delta x_2) + 2u_2(x_1 - \Delta x_1, x_2)}{2\Delta x_2} \\
&+ \frac{u_2(x_1 - \Delta x_1, x_2 + \Delta x_2) + u_2(x_1 - \Delta x_1, x_2 - \Delta x_2)}{2\Delta x_2} \\
&+ \frac{u_1(x_1 + \Delta x_1, x_2 + \Delta x_2) - u_1(x_1 + \Delta x_1, x_2 - \Delta x_2)}{2\Delta x_1} \\
&\left. - \frac{u_1(x_1 - \Delta x_1, x_2 + \Delta x_2) + u_1(x_1 - \Delta x_1, x_2 - \Delta x_2)}{2\Delta x_1} \right\}. \quad (\text{A.32})
\end{aligned}$$

Expanding using Taylor series expansions about the point (x_1, x_2) and simplifying gives:

$$\begin{aligned}
\frac{\partial \sigma_{11}}{\partial x_1} + \frac{\partial \sigma_{12}}{\partial x_2} &= E \left(\frac{\partial^2 u_1}{\partial x_1^2} + \frac{1}{12} \frac{\partial^4 u_1}{\partial x_1^4} \Delta x_1^2 \right) + \frac{E}{2} \left(\frac{\partial^2 u_1}{\partial x_2^2} + \frac{\partial^2 u_2}{\partial x_1 \partial x_2} \right. \\
&+ \left. \frac{1}{12} \frac{\partial^4 u_1}{\partial x_2^4} \Delta x_2^2 + \frac{1}{6} \frac{\partial^4 u_2}{\partial x_1^3 \partial x_2} \Delta x_1^2 + \frac{1}{6} \frac{\partial^4 u_2}{\partial x_1 \partial x_2^3} \Delta x_2^2 + \frac{1}{4} \frac{\partial^4 u_1}{\partial x_1^2 \partial x_2^2} \Delta x_1^2 \right) + \dots \quad (\text{A.33})
\end{aligned}$$

$$\begin{aligned}
\frac{\partial \sigma_{21}}{\partial x_1} + \frac{\partial \sigma_{22}}{\partial x_2} &= E \left(\frac{\partial^2 u_2}{\partial x_2^2} + \frac{1}{12} \frac{\partial^4 u_2}{\partial x_2^4} \Delta x_2^2 \right) + \frac{E}{2} \left(\frac{\partial^2 u_2}{\partial x_1^2} + \frac{\partial^2 u_1}{\partial x_1 \partial x_2} \right. \\
&+ \left. \frac{1}{12} \frac{\partial^4 u_2}{\partial x_1^4} \Delta x_1^2 + \frac{1}{6} \frac{\partial^4 u_1}{\partial x_1^3 \partial x_2} \Delta x_1^2 + \frac{1}{6} \frac{\partial^4 u_1}{\partial x_1 \partial x_2^3} \Delta x_2^2 + \frac{1}{4} \frac{\partial^4 u_2}{\partial x_1^2 \partial x_2^2} \Delta x_2^2 \right) + \dots \quad (\text{A.34})
\end{aligned}$$

Comparing the discrete expressions for the x_1 - and x_2 -momentum equations, Equations (A.33) and (A.34), with the analytical expressions, Equations (A.5) and (A.6), gives the leading-order error term for the hybrid finite volume method at an internal node:

$$\begin{aligned}
Error_i &= \frac{E}{2} \left(\frac{1}{6} \frac{\partial^4 u_i}{\partial x_i^4} \Delta x_i^2 + \frac{1}{12} \frac{\partial^4 u_i}{\partial x_k^4} \Delta x_k^2 + \frac{1}{6} \frac{\partial^4 u_k}{\partial x_i^3 \partial x_k} \Delta x_i^2 + \right. \\
&\quad \left. \frac{1}{6} \frac{\partial^4 u_k}{\partial x_i \partial x_k^3} \Delta x_k^2 + \frac{1}{4} \frac{\partial^4 u_i}{\partial x_i^2 \partial x_k^2} \Delta x_i^2 \right) \quad (\text{A.35})
\end{aligned}$$

where the nomenclature is as previously defined.

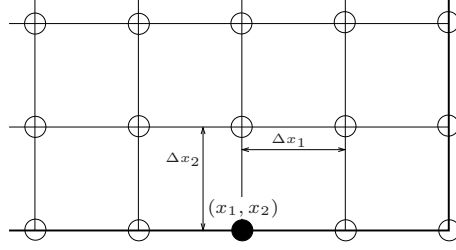


Figure A.2: Schematic of the mesh indicating a boundary node

Boundary Node - Vertex-centred FVM

Considering next a boundary node, shown in Figure A.2, with the vertex-centred finite volume formulation.

The partial derivatives of stress in the momentum equations are computed as follows:

$$\frac{\partial \sigma_{11}}{\partial x_1} \approx \frac{\sigma_{11}(x_1 + \frac{1}{2}\Delta x_1, x_2) - \sigma_{11}(x_1 - \frac{1}{2}\Delta x_1, x_2)}{\Delta x_1} \quad (\text{A.36})$$

$$\frac{\partial \sigma_{12}}{\partial x_2} \approx \frac{\sigma_{12}(x_1, x_2 + \frac{1}{2}\Delta x_2) - \sigma_{12}(x_1, x_2)}{\frac{1}{2}\Delta x_2} \quad (\text{A.37})$$

$$\frac{\partial \sigma_{21}}{\partial x_1} \approx \frac{\sigma_{21}(x_1 + \frac{1}{2}\Delta x_1, x_2) - \sigma_{21}(x_1 - \frac{1}{2}\Delta x_1, x_2)}{\Delta x_1} \quad (\text{A.38})$$

$$\frac{\partial \sigma_{22}}{\partial x_2} \approx \frac{\sigma_{22}(x_1, x_2 + \frac{1}{2}\Delta x_2) - \sigma_{22}(x_1, x_2)}{\frac{1}{2}\Delta x_2}. \quad (\text{A.39})$$

Using the stress-strain relation, Equation (A.2), and the strain-displacement relationship, Equation (A.3), the stress terms are given by:

$$\sigma_{11}(x_1 + \frac{1}{2}\Delta x_1, x_2) = E \frac{\partial u_1}{\partial x_1} \Big|_{(x_1 + \frac{1}{2}\Delta x_1, x_2)} \quad (\text{A.40})$$

$$\sigma_{22}(x_1, x_2 + \frac{1}{2}\Delta x_2) = E \frac{\partial u_2}{\partial x_2} \Big|_{(x_1, x_2 + \frac{1}{2}\Delta x_2)} \quad (\text{A.41})$$

$$\sigma_{12}(x_1, x_2 + \frac{1}{2}\Delta x_2) = \frac{E}{2} \left(\frac{\partial u_1}{\partial x_2} + \frac{\partial u_2}{\partial x_1} \right) \Big|_{(x_1, x_2 + \frac{1}{2}\Delta x_2)} \quad (\text{A.42})$$

$$\sigma_{21}(x_1 + \frac{1}{2}\Delta x_1, x_2) = \frac{E}{2} \left(\frac{\partial u_2}{\partial x_1} + \frac{\partial u_1}{\partial x_2} \right) \Big|_{(x_1 + \frac{1}{2}\Delta x_1, x_2)}. \quad (\text{A.43})$$

Along the boundary of the domain either the displacement or the traction is prescribed. For the boundary node along the bottom of the beam, as shown in Figure A.2, the traction is specified as zero, which renders $\sigma_{12}(x_1, x_2) = \sigma_{22}(x_1, x_2) = 0$.

The displacement gradients for the vertex-centred finite volume formulation are computed from Equation (3.50) as:

$$\left. \frac{\partial u_1}{\partial x_1} \right|_{(x_1 + \frac{1}{2}\Delta x_1, x_2)} \approx \frac{u_1(x_1 + \Delta x_1, x_2) - u_1(x_1, x_2)}{\Delta x_1} \quad (\text{A.44})$$

$$\left. \frac{\partial u_2}{\partial x_2} \right|_{(x_1, x_2 + \frac{1}{2}\Delta x_2)} \approx \frac{u_2(x_1, x_2 + \Delta x_2) - u_2(x_1, x_2)}{\Delta x_2} \quad (\text{A.45})$$

$$\left. \frac{\partial u_1}{\partial x_2} \right|_{(x_1, x_2 + \frac{1}{2}\Delta x_2)} \approx \frac{u_1(x_1, x_2 + \Delta x_2) - u_1(x_1, x_2)}{\Delta x_2} \quad (\text{A.46})$$

$$\begin{aligned} \left. \frac{\partial u_2}{\partial x_1} \right|_{(x_1, x_2 + \frac{1}{2}\Delta x_2)} &\approx \frac{1}{2} \left(\left. \frac{\partial u_2}{\partial x_1} \right|_{(x_1, x_2 + \Delta x_2)} + \left. \frac{\partial u_2}{\partial x_1} \right|_{(x_1, x_2)} \right) \\ &\approx \frac{1}{4\Delta x_1} \left[u_2(x_1 + \Delta x_1, x_2 + \Delta x_2) + u_2(x_1 + \Delta x_1, x_2) \right. \\ &\quad \left. - u_2(x_1 - \Delta x_1, x_2 + \Delta x_2) - u_2(x_1 - \Delta x_1, x_2) \right] \quad (\text{A.47}) \end{aligned}$$

$$\begin{aligned} \left. \frac{\partial u_1}{\partial x_2} \right|_{(x_1 + \frac{1}{2}\Delta x_1, x_2)} &\approx \frac{1}{2} \left(\left. \frac{\partial u_1}{\partial x_2} \right|_{(x_1 + \Delta x_1, x_2)} + \left. \frac{\partial u_1}{\partial x_2} \right|_{(x_1, x_2)} \right) \\ &\approx \frac{1}{2\Delta x_2} \left[u_1(x_1 + \Delta x_1, x_2 + \Delta x_2) + u_1(x_1, x_2 + \Delta x_2) \right. \\ &\quad \left. - u_1(x_1 + \Delta x_1, x_2) - u_1(x_1, x_2) \right] \quad (\text{A.48}) \end{aligned}$$

$$\left. \frac{\partial u_2}{\partial x_1} \right|_{(x_1 + \frac{1}{2}\Delta x_1, x_2)} \approx \frac{u_2(x_1 + \Delta x_1, x_2) - u_2(x_1, x_2)}{\Delta x_1}. \quad (\text{A.49})$$

Using the above expressions for the displacement gradients and stress terms, the discrete expressions for the x_1 - and x_2 -momentum equations are:

$$\begin{aligned} \frac{\partial \sigma_{11}}{\partial x_1} + \frac{\partial \sigma_{12}}{\partial x_2} &\approx \frac{E}{\Delta x_1} \left\{ \frac{u_1(x_1 + \Delta x_1, x_2) - 2u_1(x_1, x_2) + u_1(x_1 - \Delta x_1, x_2)}{\Delta x_1} \right\} \\ &\quad + \frac{E}{\Delta x_2} \left\{ \frac{u_1(x_1, x_2 + \Delta x_2) - u_1(x_1, x_2)}{\Delta x_2} + \frac{u_2(x_1 + \Delta x_1, x_2 + \Delta x_2)}{4\Delta x_1} \right. \\ &\quad \left. + \frac{u_2(x_1 + \Delta x_1, x_2) - u_2(x_1 - \Delta x_1, x_2 + \Delta x_2) - u_2(x_1 - \Delta x_1, x_2)}{4\Delta x_1} \right\} \quad (\text{A.50}) \end{aligned}$$

$$\begin{aligned}
\frac{\partial \sigma_{21}}{\partial x_1} + \frac{\partial \sigma_{22}}{\partial x_2} &\approx \frac{E}{\Delta x_2} \left\{ \frac{u_2(x_1, x_2 + \Delta x_2) - u_2(x_1, x_2)}{\frac{1}{2} \Delta x_2} \right\} \\
&+ \frac{E}{2\Delta x_1} \left\{ \frac{u_2(x_1 + \Delta x_1, x_2) - 2u_2(x_1, x_2) + u_2(x_1 - \Delta x_1, x_2)}{\Delta x_1} \right. \\
&+ \frac{u_1(x_1 + \Delta x_1, x_2 + \Delta x_2) - u_1(x_1 + \Delta x_1, x_2)}{2\Delta x_2} \\
&\left. - \frac{u_1(x_1 - \Delta x_1, x_2 + \Delta x_2) + u_1(x_1 - \Delta x_1, x_2)}{2\Delta x_2} \right\}. \quad (\text{A.51})
\end{aligned}$$

Expanding using Taylor series expansions about the point (x_1, x_2) and simplifying gives:

$$\begin{aligned}
\frac{\partial \sigma_{11}}{\partial x_1} + \frac{\partial \sigma_{12}}{\partial x_2} &= E \left(\frac{\partial^2 u_1}{\partial x_1^2} + \frac{1}{12} \frac{\partial^4 u_1}{\partial x_1^4} \Delta x_1^2 \right) + \frac{E}{2} \left(\frac{\partial^2 u_1}{\partial x_2^2} + \frac{\partial^2 u_2}{\partial x_1 \partial x_2} \right. \\
&\left. + \frac{1}{3} \frac{\partial^3 u_1}{\partial x_2^3} \Delta x_2 + \frac{1}{2} \frac{\partial^3 u_2}{\partial x_1 \partial x_2^2} \Delta x_2 + \frac{1}{3} \frac{\partial^3 u_2}{\partial x_1^3} \frac{\Delta x_1^2}{\Delta x_2} \right) + \dots \quad (\text{A.52})
\end{aligned}$$

$$\begin{aligned}
\frac{\partial \sigma_{21}}{\partial x_1} + \frac{\partial \sigma_{22}}{\partial x_2} &= E \left(\frac{\partial^2 u_2}{\partial x_2^2} \right) + \frac{E}{2} \left(\frac{\partial^2 u_2}{\partial x_1^2} + \frac{\partial^2 u_1}{\partial x_1 \partial x_2} + \frac{1}{2} \frac{\partial^3 u_1}{\partial x_1 \partial x_2^2} \Delta x_2 \right) + \dots \\
&\quad (\text{A.53})
\end{aligned}$$

By comparing the discrete expressions for the x_1 - and x_2 -momentum equations, Equations (A.52) and (A.53), with the analytical expressions, Equations (A.5) and (A.6), the leading-order error terms for the tangential and normal components of the momentum equations, respectively, are:

$$\begin{aligned}
Error_t &= \frac{E}{2} \left(\frac{1}{6} \frac{\partial^4 u_t}{\partial x_t^4} \Delta x_t^2 + \frac{1}{3} \frac{\partial^3 u_t}{\partial x_n^3} \Delta x_n + (-1)^p \frac{1}{2} \frac{\partial^3 u_n}{\partial x_t \partial x_n^2} \Delta x_n + \right. \\
&\quad \left. (-1)^p \frac{1}{3} \frac{\partial^3 u_n}{\partial x_t^3} \frac{\Delta x_t^2}{\Delta x_n} \right) \quad (\text{A.54})
\end{aligned}$$

$$Error_n = \frac{E}{2} \left((-1)^p \frac{1}{2} \frac{\partial^3 u_t}{\partial x_t \partial x_n^2} \Delta x_n \right) \quad (\text{A.55})$$

where subscripts n and t denote coordinates normal and tangential to the boundary respectively, $p = 1$ for the top and right boundaries and $p = 2$ for the bottom and left boundaries.

Boundary Node - Hybrid FVM

For a boundary node (Figure A.2) with the hybrid FVM, the elemental-based gradients are computed using Equation (3.53) as:

$$\begin{aligned} \left. \frac{\partial u_1}{\partial x_2} \right|_{(x_1, x_2 + \frac{1}{2}\Delta x_2)} &\approx \frac{1}{2} \left(\left. \frac{\partial u_1}{\partial x_2} \right|_{(x_1 + \frac{1}{2}\Delta x_1, x_2 + \frac{1}{2}\Delta x_2)} + \left. \frac{\partial u_1}{\partial x_2} \right|_{(x_1 - \frac{1}{2}\Delta x_1, x_2 + \frac{1}{2}\Delta x_2)} \right) \\ &\approx \frac{1}{4\Delta x_2} \left[u_1(x_1 + \Delta x_1, x_2 + \Delta x_2) - u_1(x_1 + \Delta x_1, x_2) \right. \\ &\quad + 2u_1(x_1, x_2 + \Delta x_2) - 2u_1(x_1, x_2) \\ &\quad \left. + u_1(x_1 - \Delta x_1, x_2 + \Delta x_2) - u_1(x_1 - \Delta x_1, x_2) \right] \quad (\text{A.56}) \end{aligned}$$

$$\begin{aligned} \left. \frac{\partial u_2}{\partial x_1} \right|_{(x_1, x_2 + \frac{1}{2}\Delta x_2)} &\approx \frac{1}{2} \left(\left. \frac{\partial u_2}{\partial x_1} \right|_{(x_1 + \frac{1}{2}\Delta x_1, x_2 + \frac{1}{2}\Delta x_2)} + \left. \frac{\partial u_2}{\partial x_1} \right|_{(x_1 - \frac{1}{2}\Delta x_1, x_2 + \frac{1}{2}\Delta x_2)} \right) \\ &\approx \frac{1}{4\Delta x_1} \left[u_2(x_1 + \Delta x_1, x_2 + \Delta x_2) + u_2(x_1 + \Delta x_1, x_2) \right. \\ &\quad \left. - u_2(x_1 - \Delta x_1, x_2 + \Delta x_2) - u_2(x_1 - \Delta x_1, x_2) \right] \quad (\text{A.57}) \end{aligned}$$

$$\begin{aligned} \left. \frac{\partial u_1}{\partial x_2} \right|_{(x_1 + \frac{1}{2}\Delta x_1, x_2)} &\approx \left. \frac{\partial u_1}{\partial x_2} \right|_{(x_1 + \frac{1}{2}\Delta x_1, x_2 + \frac{1}{2}\Delta x_2)} \\ &\approx \frac{1}{2\Delta x_2} \left[u_1(x_1 + \Delta x_1, x_2 + \Delta x_2) + u_1(x_1, x_2 + \Delta x_2) \right. \\ &\quad \left. - u_1(x_1 + \Delta x_1, x_2) - u_1(x_1, x_2) \right] \quad (\text{A.58}) \end{aligned}$$

$$\begin{aligned} \left. \frac{\partial u_2}{\partial x_1} \right|_{(x_1 + \frac{1}{2}\Delta x_1, x_2)} &\approx \left. \frac{\partial u_2}{\partial x_1} \right|_{(x_1 + \frac{1}{2}\Delta x_1, x_2 + \frac{1}{2}\Delta x_2)} \\ &\approx \frac{1}{2\Delta x_1} \left[u_2(x_1 + \Delta x_1, x_2 + \Delta x_2) - u_2(x_1, x_2 + \Delta x_2) \right. \\ &\quad \left. + u_2(x_1 + \Delta x_1, x_2) - u_2(x_1, x_2) \right]. \quad (\text{A.59}) \end{aligned}$$

Substituting these expressions for the displacement gradients gives the fol-

lowing discrete expressions for the for the x_1 - and x_2 -momentum equations:

$$\begin{aligned} \frac{\partial \sigma_{11}}{\partial x_1} + \frac{\partial \sigma_{12}}{\partial x_2} &\approx \frac{E}{\Delta x_1} \left\{ \frac{u_1(x_1 + \Delta x_1, x_2) - 2u_1(x_1, x_2) + u_1(x_1 - \Delta x_1, x_2)}{\Delta x_1} \right\} + \\ \frac{E}{4\Delta x_2} &\left\{ \frac{u_1(x_1 + \Delta x_1, x_2 + \Delta x_2) + 2u_1(x_1, x_2 + \Delta x_2) + u_1(x_1 - \Delta x_1, x_2 + \Delta x_2)}{\Delta x_2} \right. \\ &\quad - \frac{u_1(x_1 + \Delta x_1, x_2) - 2u_1(x_1, x_2) - u_1(x_1 - \Delta x_1, x_2)}{\Delta x_2} \\ &\quad + \frac{u_2(x_1 + \Delta x_1, x_2 + \Delta x_2) - u_2(x_1 - \Delta x_1, x_2 + \Delta x_2)}{\Delta x_1} \\ &\quad \left. + \frac{u_2(x_1 + \Delta x_1, x_2) - u_2(x_1 - \Delta x_1, x_2)}{\Delta x_1} \right\} \quad (\text{A.60}) \end{aligned}$$

$$\begin{aligned} \frac{\partial \sigma_{21}}{\partial x_1} + \frac{\partial \sigma_{22}}{\partial x_2} &\approx \frac{E}{\Delta x_2} \left\{ \frac{u_2(x_1, x_2 + \Delta x_2) - u_2(x_1, x_2)}{\frac{1}{2}\Delta x_2} \right\} + \\ \frac{E}{4\Delta x_1} &\left\{ \frac{u_2(x_1 + \Delta x_1, x_2 + \Delta x_2) + u_2(x_1 + \Delta x_1, x_2) - 2u_2(x_1, x_2 + \Delta x_2)}{\Delta x_1} \right. \\ &\quad - \frac{2u_2(x_1, x_2) + u_2(x_1 - \Delta x_1, x_2 + \Delta x_2) + u_2(x_1 - \Delta x_1, x_2)}{\Delta x_1} \\ &\quad + \frac{u_1(x_1 + \Delta x_1, x_2 + \Delta x_2) - u_1(x_1 + \Delta x_1, x_2)}{\Delta x_2} \\ &\quad \left. - \frac{u_1(x_1 - \Delta x_1, x_2 + \Delta x_2) + u_1(x_1 - \Delta x_1, x_2)}{\Delta x_2} \right\}. \quad (\text{A.61}) \end{aligned}$$

Expanding using Taylor series expansions about the point (x_1, x_2) and simplifying gives:

$$\begin{aligned} \frac{\partial \sigma_{11}}{\partial x_1} + \frac{\partial \sigma_{12}}{\partial x_2} &= E \left(\frac{\partial^2 u_1}{\partial x_1^2} + \frac{1}{12} \frac{\partial^4 u_1}{\partial x_1^4} \Delta x_1^2 \right) + \frac{E}{2} \left(\frac{\partial^2 u_1}{\partial x_2^2} + \frac{\partial^2 u_2}{\partial x_1 \partial x_2} \right. \\ &\quad \left. + \frac{1}{3} \frac{\partial^3 u_1}{\partial x_2^3} \Delta x_2 + \frac{1}{2} \frac{\partial^3 u_2}{\partial x_1 \partial x_2^2} \Delta x_2 + \frac{1}{3} \frac{\partial^3 u_2}{\partial x_1^3} \frac{\Delta x_1^2}{\Delta x_2} + \frac{1}{2} \frac{\partial^3 u_1}{\partial x_1^2 \partial x_2} \frac{\Delta x_1^2}{\Delta x_2} \right) + \dots \quad (\text{A.62}) \end{aligned}$$

$$\begin{aligned} \frac{\partial \sigma_{21}}{\partial x_1} + \frac{\partial \sigma_{22}}{\partial x_2} &= E \left(\frac{\partial^2 u_2}{\partial x_2^2} \right) + \frac{E}{2} \left(\frac{\partial^2 u_2}{\partial x_1^2} + \frac{\partial^2 u_1}{\partial x_1 \partial x_2} \right. \\ &\quad \left. + \frac{1}{2} \frac{\partial^3 u_1}{\partial x_1 \partial x_2^2} \Delta x_2 + \frac{1}{2} \frac{\partial^3 u_2}{\partial x_2^2 \partial x_2} \Delta x_2 \right) + \dots \quad (\text{A.63}) \end{aligned}$$

Comparing the discrete expressions for the x_1 - and x_2 -momentum equations, Equations (A.62) and (A.63), with the analytical expressions, Equations (A.5) and (A.6), gives the leading-order error terms for the hybrid finite volume method at a boundary node:

$$Error_t = \frac{E}{2} \left(\frac{1}{6} \frac{\partial^4 u_t}{\partial x_t^4} \Delta x_t^2 + \frac{1}{3} \frac{\partial^3 u_t}{\partial x_n^3} \Delta x_n + (-1)^p \frac{1}{2} \frac{\partial^3 u_n}{\partial x_t \partial x_n^2} \Delta x_n + \right. \\ \left. (-1)^p \frac{1}{3} \frac{\partial^3 u_n}{\partial x_t^3} \frac{\Delta x_t^2}{\Delta x_n} + (-1)^q \frac{\partial^3 u_t}{\partial x_t^2 \partial x_n} \frac{\Delta x_t^2}{\Delta x_n} \right) \quad (A.64)$$

$$Error_n = \frac{E}{2} \left((-1)^p \frac{1}{2} \frac{\partial^3 u_t}{\partial x_t \partial x_n^2} \Delta x_n + (-1)^q \frac{1}{2} \frac{\partial^3 u_n}{\partial x_t^2 \partial x_n} \Delta x_n \right) \quad (A.65)$$

where $q = 1$ for the left and right boundaries and $q = 2$ for the bottom and left boundaries and the rest of the symbols are as previously defined.

Corner Node - Vertex-centred FVM

For a corner node as shown in Figure A.3 the partial derivatives of stress are:

$$\frac{\partial \sigma_{11}}{\partial x_1} \approx \frac{\sigma_{11}(x_1, x_2) - \sigma_{11}(x_1 - \frac{1}{2} \Delta x_1, x_2)}{\frac{1}{2} \Delta x_1} \quad (A.66)$$

$$\frac{\partial \sigma_{12}}{\partial x_2} \approx \frac{\sigma_{12}(x_1, x_2 + \frac{1}{2} \Delta x_2) - \sigma_{12}(x_1, x_2)}{\frac{1}{2} \Delta x_2} \quad (A.67)$$

$$\frac{\partial \sigma_{21}}{\partial x_1} \approx \frac{\sigma_{21}(x_1, x_2) - \sigma_{21}(x_1 - \frac{1}{2} \Delta x_1, x_2)}{\frac{1}{2} \Delta x_1} \quad (A.68)$$

$$\frac{\partial \sigma_{22}}{\partial x_2} \approx \frac{\sigma_{22}(x_1, x_2 + \frac{1}{2} \Delta x_2) - \sigma_{22}(x_1, x_2)}{\frac{1}{2} \Delta x_2}. \quad (A.69)$$

Using the stress-strain relation, Equation (A.2), and the strain-displacement relationship, Equation (A.3), the stress terms are given by:

$$\sigma_{11}(x_1 - \frac{1}{2} \Delta x_1, x_2) = E \frac{\partial u_1}{\partial x_1} \Big|_{(x_1 - \frac{1}{2} \Delta x_1, x_2)} \quad (A.70)$$

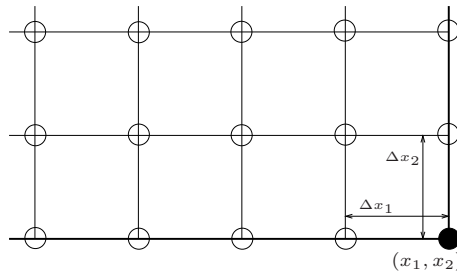


Figure A.3: Schematic of the mesh indicating a corner node

$$\sigma_{22}(x_1, x_2 + \frac{1}{2}\Delta x_2) = E \frac{\partial u_2}{\partial x_2} \Big|_{(x_1, x_2 + \frac{1}{2}\Delta x_2)} \quad (\text{A.71})$$

$$\sigma_{12}(x_1, x_2 + \frac{1}{2}\Delta x_2) = \frac{E}{2} \left(\frac{\partial u_1}{\partial x_2} + \frac{\partial u_2}{\partial x_1} \right) \Big|_{(x_1, x_2 + \frac{1}{2}\Delta x_2)} \quad (\text{A.72})$$

$$\sigma_{21}(x_1 - \frac{1}{2}\Delta x_1, x_2) = \frac{E}{2} \left(\frac{\partial u_2}{\partial x_1} + \frac{\partial u_1}{\partial x_2} \right) \Big|_{(x_1 - \frac{1}{2}\Delta x_1, x_2)} \quad (\text{A.73})$$

The displacement gradients are computed from Equation (3.50) as:

$$\frac{\partial u_1}{\partial x_1} \Big|_{(x_1 - \frac{1}{2}\Delta x_1, x_2)} \approx \frac{u_1(x_1, x_2) - u_1(x_1 - \Delta x_1, x_2)}{\Delta x_1} \quad (\text{A.74})$$

$$\frac{\partial u_2}{\partial x_2} \Big|_{(x_1, x_2 + \frac{1}{2}\Delta x_2)} \approx \frac{u_2(x_1, x_2 + \Delta x_2) - u_2(x_1, x_2)}{\Delta x_2} \quad (\text{A.75})$$

$$\frac{\partial u_1}{\partial x_2} \Big|_{(x_1, x_2 + \frac{1}{2}\Delta x_2)} \approx \frac{u_1(x_1, x_2 + \Delta x_2) - u_1(x_1, x_2)}{\Delta x_2} \quad (\text{A.76})$$

$$\begin{aligned} \frac{\partial u_2}{\partial x_1} \Big|_{(x_1, x_2 + \frac{1}{2}\Delta x_2)} &\approx \frac{1}{2} \left(\frac{\partial u_2}{\partial x_1} \Big|_{(x_1, x_2 + \Delta x_2)} + \frac{\partial u_2}{\partial x_1} \Big|_{(x_1, x_2)} \right) \\ &\approx \frac{1}{2\Delta x_1} \left[u_2(x_1, x_2 + \Delta x_2) + u_2(x_1, x_2) \right. \\ &\quad \left. - u_2(x_1 - \Delta x_1, x_2 + \Delta x_2) - u_2(x_1 - \Delta x_1, x_2) \right] \quad (\text{A.77}) \end{aligned}$$

$$\begin{aligned} \frac{\partial u_1}{\partial x_2} \Big|_{(x_1 - \frac{1}{2}\Delta x_1, x_2)} &\approx \frac{1}{2} \left(\frac{\partial u_1}{\partial x_2} \Big|_{(x_1 - \Delta x_1, x_2)} + \frac{\partial u_1}{\partial x_2} \Big|_{(x_1, x_2)} \right) \\ &\approx \frac{1}{2\Delta x_2} \left[u_1(x_1 - \Delta x_1, x_2 + \Delta x_2) + u_1(x_1, x_2 + \Delta x_2) \right. \\ &\quad \left. - u_1(x_1 - \Delta x_1, x_2) - u_1(x_1, x_2) \right] \quad (\text{A.78}) \end{aligned}$$

$$\frac{\partial u_2}{\partial x_1} \Big|_{(x_1 - \frac{1}{2}\Delta x_1, x_2)} \approx \frac{u_2(x_1, x_2) - u_2(x_1 - \Delta x_1, x_2)}{\Delta x_1} \quad (\text{A.79})$$

Using the above expressions for the displacement gradients and stress terms, the discrete expressions for the x_1 - and x_2 -momentum equations are:

$$\begin{aligned} \frac{\partial \sigma_{11}}{\partial x_1} + \frac{\partial \sigma_{12}}{\partial x_2} &\approx \frac{E}{\Delta x_1} \left\{ \frac{u_1(x_1, x_2) - u_1(x_1 - \Delta x_1, x_2)}{\frac{1}{2}\Delta x_1} \right\} \\ &+ \frac{E}{\Delta x_2} \left\{ \frac{u_1(x_1, x_2 + \Delta x_2) - u_1(x_1, x_2)}{\Delta x_2} + \frac{u_2(x_1, x_2 + \Delta x_2)}{2\Delta x_1} \right. \\ &\left. + \frac{u_2(x_1, x_2) - u_2(x_1 - \Delta x_1, x_2 + \Delta x_2) - u_2(x_1 - \Delta x_1, x_2)}{2\Delta x_1} \right\} \quad (\text{A.80}) \end{aligned}$$

$$\begin{aligned} \frac{\partial \sigma_{21}}{\partial x_1} + \frac{\partial \sigma_{22}}{\partial x_2} &\approx \frac{E}{\Delta x_2} \left\{ \frac{u_2(x_1, x_2 + \Delta x_2) - u_2(x_1, x_2)}{\frac{1}{2}\Delta x_2} \right\} \\ &+ \frac{E}{\Delta x_1} \left\{ \frac{u_2(x_1 - \Delta x_1, x_2) - u_2(x_1, x_2)}{\Delta x_1} + \frac{u_1(x_1, x_2) + u_1(x_1 - \Delta x_1, x_2)}{2\Delta x_2} \right. \\ &\left. - \frac{u_1(x_1, x_2 + \Delta x_2) - u_1(x_1 - \Delta x_1, x_2 + \Delta x_2)}{2\Delta x_2} \right\}. \quad (\text{A.81}) \end{aligned}$$

Expanding using Taylor series expansions about the point (x_1, x_2) and simplifying gives:

$$\frac{\partial \sigma_{11}}{\partial x_1} + \frac{\partial \sigma_{12}}{\partial x_2} = E \left(\frac{\partial^2 u_1}{\partial x_1^2} - \frac{1}{3} \frac{\partial^3 u_1}{\partial x_1^3} \Delta x_1 \right) + \frac{E}{2} \left(\frac{\partial^2 u_1}{\partial x_2^2} + \frac{\partial^2 u_2}{\partial x_1 \partial x_2} - \frac{\partial^2 u_2}{\partial x_1^2} \frac{\partial x_1}{\Delta x_2} \right) + \dots \quad (\text{A.82})$$

$$\frac{\partial \sigma_{21}}{\partial x_1} + \frac{\partial \sigma_{22}}{\partial x_2} = E \left(\frac{\partial^2 u_2}{\partial x_2^2} \right) + \frac{E}{2} \left(\frac{\partial^2 u_2}{\partial x_1^2} + \frac{\partial^2 u_1}{\partial x_1 \partial x_2} - \frac{\partial^2 u_1}{\partial x_2^2} \frac{\Delta x_2}{\Delta x_1} \right) + \dots \quad (\text{A.83})$$

By comparing the discrete expressions for the x_1 - and x_2 -momentum equations, Equations (A.82) and (A.83), with the analytical expressions, Equations (A.5) and (A.6), the leading-order error term for the vertex-centred FVM at a corner node is:

$$Error_i = \frac{E}{2} \left((-1)^p \frac{\partial^2 u_k}{\partial x_i^2} \frac{\Delta x_i}{\Delta x_k} \right) \quad (\text{A.84})$$

with

- $i = 1; k = 2$ for the x_1 -momentum equation
- $i = 2; k = 1$ for the x_2 -momentum equation
- $p = 1$ for the top-left and bottom-right corners
- $p = 2$ for the top-right and bottom-left corners.

Corner Node - Hybrid FVM

Finally, for a corner node (Figure A.3) with the hybrid FVM, the elemental-based gradients are computed using Equation (3.53) as:

$$\begin{aligned} \left. \frac{\partial u_1}{\partial x_2} \right|_{(x_1, x_2 + \frac{1}{2}\Delta x_2)} &\approx \left. \frac{\partial u_1}{\partial x_2} \right|_{(x_1 - \frac{1}{2}\Delta x_1, x_2 + \frac{1}{2}\Delta x_2)} \\ &\approx \frac{1}{2\Delta x_2} \left[u_1(x_1, x_2 + \Delta x_2) - u_1(x_1, x_2) \right. \\ &\quad \left. + u_1(x_1 - \Delta x_1, x_2 + \Delta x_2) - u_1(x_1 - \Delta x_1, x_2) \right] \end{aligned} \quad (\text{A.85})$$

$$\begin{aligned} \left. \frac{\partial u_2}{\partial x_1} \right|_{(x_1, x_2 + \frac{1}{2}\Delta x_2)} &\approx \left. \frac{\partial u_2}{\partial x_1} \right|_{(x_1 - \frac{1}{2}\Delta x_1, x_2 + \frac{1}{2}\Delta x_2)} \\ &\approx \frac{1}{2\Delta x_1} \left[u_2(x_1, x_2 + \Delta x_2) + u_2(x_1, x_2) \right. \\ &\quad \left. - u_2(x_1 - \Delta x_1, x_2 + \Delta x_2) - u_2(x_1 - \Delta x_1, x_2) \right] \end{aligned} \quad (\text{A.86})$$

$$\begin{aligned} \left. \frac{\partial u_1}{\partial x_2} \right|_{(x_1 - \frac{1}{2}\Delta x_1, x_2)} &\approx \left. \frac{\partial u_1}{\partial x_2} \right|_{(x_1 - \frac{1}{2}\Delta x_1, x_2 + \frac{1}{2}\Delta x_2)} \\ &\approx \frac{1}{2\Delta x_2} \left[u_1(x_1, x_2 + \Delta x_2) + u_1(x_1, x_2) \right. \\ &\quad \left. + u_1(x_1 + \Delta x_1, x_2 + \Delta x_2) - u_1(x_1 - \Delta x_1, x_2) \right] \end{aligned} \quad (\text{A.87})$$

$$\begin{aligned} \left. \frac{\partial u_2}{\partial x_1} \right|_{(x_1 + \frac{1}{2}\Delta x_1, x_2)} &\approx \left. \frac{\partial u_2}{\partial x_1} \right|_{(x_1 - \frac{1}{2}\Delta x_1, x_2 + \frac{1}{2}\Delta x_2)} \\ &\approx \frac{1}{2\Delta x_1} \left[u_2(x_1, x_2 + \Delta x_2) - u_2(x_1 - \Delta x_1, x_2 + \Delta x_2) \right. \\ &\quad \left. + u_2(x_1 + \Delta x_1, x_2) - u_2(x_1 - \Delta x_1, x_2) \right]. \end{aligned} \quad (\text{A.88})$$

Substituting these expressions for the displacement gradients gives the fol-

lowing discrete expressions for the for the x_1 - and x_2 -momentum equations:

$$\begin{aligned} \frac{\partial \sigma_{11}}{\partial x_1} + \frac{\partial \sigma_{12}}{\partial x_2} \approx & \frac{E}{\Delta x_1} \left\{ \frac{u_1(x_1, x_2) - u_1(x_1 - \Delta x_1, x_2)}{\frac{1}{2} \Delta x_1} \right\} \\ & \frac{E}{2\Delta x_2} \left\{ \frac{u_1(x_1, x_2 + \Delta x_2) + u_1(x_1 - \Delta x_1, x_2 + \Delta x_2) - u_1(x_1, x_2)}{\Delta x_2} \right. \\ & - \frac{u_1(x_1 - \Delta x_1, x_2)}{\Delta x_2} + \frac{u_2(x_1, x_2 + \Delta x_2) - u_2(x_1 - \Delta x_1, x_2 + \Delta x_2)}{\Delta x_1} \\ & \left. + \frac{u_2(x_1, x_2) - u_2(x_1 - \Delta x_1, x_2)}{\Delta x_1} \right\} \quad (\text{A.89}) \end{aligned}$$

$$\begin{aligned} \frac{\partial \sigma_{21}}{\partial x_1} + \frac{\partial \sigma_{22}}{\partial x_2} \approx & \frac{E}{\Delta x_2} \left\{ \frac{u_2(x_1, x_2 + \Delta x_2) - u_2(x_1, x_2)}{\frac{1}{2} \Delta x_2} \right\} \\ & \frac{E}{2\Delta x_1} \left\{ \frac{u_2(x_1 - \Delta x_1, x_2 + \Delta x_2) + u_2(x_1 - \Delta x_1, x_2) - u_2(x_1, x_2)}{\Delta x_1} \right. \\ & - \frac{u_2(x_1, x_2 + \Delta x_2)}{\Delta x_1} + \frac{u_1(x_1 - \Delta x_1, x_2) - u_1(x_1 - \Delta x_1, x_2 + \Delta x_2)}{\Delta x_2} \\ & \left. + \frac{u_1(x_1, x_2) - u_1(x_1, x_2 + \Delta x_2)}{\Delta x_2} \right\}. \quad (\text{A.90}) \end{aligned}$$

Expanding using Taylor series expansions about the point (x_1, x_2) and simplifying gives:

$$\begin{aligned} \frac{\partial \sigma_{11}}{\partial x_1} + \frac{\partial \sigma_{12}}{\partial x_2} = & E \left(\frac{\partial^2 u_1}{\partial x_1^2} - \frac{1}{3} \frac{\partial^3 u_1}{\partial x_1^3} \Delta x_1 \right) + \frac{E}{2} \left(\frac{\partial^2 u_1}{\partial x_2^2} + \frac{\partial^2 u_2}{\partial x_1 \partial x_2} \right. \\ & \left. - \frac{\partial^2 u_2}{\partial x_1^2} \frac{\partial x_1}{\Delta x_2} - \frac{\partial^2 u_1}{\partial x_1 \partial x_2} \frac{\partial x_1}{\Delta x_2} \right) + \dots \quad (\text{A.91}) \end{aligned}$$

$$\begin{aligned} \frac{\partial \sigma_{21}}{\partial x_1} + \frac{\partial \sigma_{22}}{\partial x_2} = & E \left(\frac{\partial^2 u_2}{\partial x_2^2} \right) + \frac{E}{2} \left(\frac{\partial^2 u_2}{\partial x_1^2} + \frac{\partial^2 u_1}{\partial x_1 \partial x_2} - \frac{\partial^2 u_1}{\partial x_2^2} \frac{\Delta x_2}{\Delta x_1} \right. \\ & \left. - \frac{\partial^2 u_2}{\partial x_1 \partial x_2} \frac{\Delta x_2}{\Delta x_1} \right) + \dots \quad (\text{A.92}) \end{aligned}$$

Comparing the discrete expressions for the x_1 - and x_2 -momentum equations, Equations (A.91) and (A.92), with the analytical expressions, Equations (A.5) and (A.6), gives the leading-order error term for the hybrid FVM at a corner node:

$$\text{Error}_i = \frac{E}{2} \left((-1)^p \frac{\partial^2 u_k}{\partial x_i^2} \frac{\Delta x_i}{\Delta x_k} - \frac{\partial^2 u_i}{\partial x_i \partial x_k} \frac{\Delta x_i}{\Delta x_k} \right) \quad (\text{A.93})$$

where the nomenclature is as previously defined.

Appendix B

Derivation of Third-Order Gradient Approximation

The higher-order finite volume formulation uses third-order approximations for the displacement gradients at boundary nodes. The derivation of this approximation is shown in this section.

Consider a boundary node as shown in Figure B.1. To derive a third-order approximation for the gradient $\frac{\partial u_1}{\partial x_2}$, we note that the displacement values over three elements are required. The form of the resulting equation is:

$$\frac{\partial u_1}{\partial x_2} \approx Au_{1(x_1, x_2)} + Bu_{1(x_1, x_2 + \Delta x_2)} + Cu_{1(x_1, x_2 + 2\Delta x_2)} + Du_{1(x_1, x_2 + 3\Delta x_2)}. \quad (\text{B.1})$$

Expanding each displacement term to third-order using Taylor series expansions about the point (x_1, x_2) gives:

$$Au_{1(x_1, x_2)} = Au_1 \quad (\text{B.2})$$

$$Bu_{1(x_1, x_2 + \Delta x_2)} \approx Bu_1 + B\frac{\partial u_1}{\partial x_1}\Delta x_2 + B\frac{1}{2}\frac{\partial^2 u_1}{\partial x_2^2}\Delta x_2^2 + \frac{1}{6}B\frac{\partial^3 u_1}{\partial x_2^3}\Delta x_2^3 \quad (\text{B.3})$$

$$Cu_{1(x_1, x_2 + 2\Delta x_2)} \approx Cu_1 + 2C\frac{\partial u_1}{\partial x_1}\Delta x_2 + 2C\frac{\partial^2 u_1}{\partial x_2^2}\Delta x_2^2 + \frac{4}{3}C\frac{\partial^3 u_1}{\partial x_2^3}\Delta x_2^3 \quad (\text{B.4})$$

$$Du_{1(x_1, x_2 + 3\Delta x_2)} \approx Du_1 + 3D\frac{\partial u_1}{\partial x_1}\Delta x_2 + \frac{9}{2}D\frac{\partial^2 u_1}{\partial x_2^2}\Delta x_2^2 + \frac{27}{6}D\frac{\partial^3 u_1}{\partial x_2^3}\Delta x_2^3. \quad (\text{B.5})$$

Now, since we want a third-order approximation we note that:

$$A + B + C + D = 0 \quad (\text{B.6})$$

$$B + 2C + 3D = 1 \quad (\text{B.7})$$

$$\frac{1}{2}B + 2C + \frac{9}{2}D = 0 \quad (\text{B.8})$$

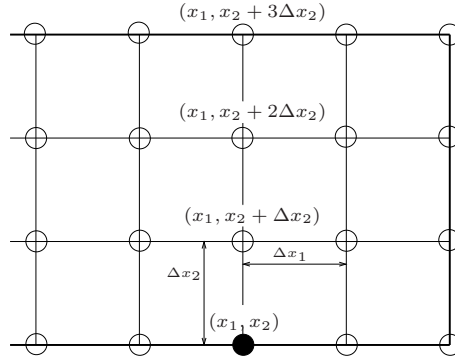


Figure B.1: Schematic of mesh indicating a boundary node at the bottom boundary of a beam

$$\frac{1}{6}B + \frac{4}{3}C + \frac{27}{6}D = 0. \quad (\text{B.9})$$

Solving the equations above simultaneously yields the following expression for the gradient $\left. \frac{\partial u_1}{\partial x_2} \right|_{(x_1, x_2)}$:

$$\left. \frac{\partial u_1}{\partial x_2} \right|_{(x_1, x_2)} \approx \frac{-11u_{1(x_1, x_2)} + 18u_{1(x_1, x_2 + \Delta x_2)} - 9u_{1(x_1, x_2 + 2\Delta x_2)} + 2u_{1(x_1, x_2 + 3\Delta x_2)}}{6\Delta x_2}. \quad (\text{B.10})$$

A similar approach is followed to obtain the remaining displacement gradient approximations.

Bibliography

- [1] B. Hubner, E. Walhorn, and D. Dinkler. A monolithic approach to fluid-structure interaction using space-time finite elements. *Computer Methods in Applied Mechanics and Engineering*, 193:2087–2104, 2004.
- [2] A.K. Slone, K. Pericleous, C. Bailey, M. Cross, and C. Bennett. A finite volume unstructured mesh approach to dynamic fluid-structure interaction: an assessment of the challenge of predicting the onset of flutter. *Applied Mathematical Modelling*, 28:211–239, 2004.
- [3] C. Farhat and M. Lesoinne. Two efficient staggered algorithms for the serial and parallel solution of three-dimensional nonlinear transient aeroelastic problems. *Computer Methods in Applied Mechanics and Engineering*, 182:499–515, 2000.
- [4] C.A. Taylor, T.J.R. Hughes, and C.K. Zarins. Finite element modelling of blood flow in arteries. *Computer Methods in Applied Mechanics and Engineering*, 158:155–196, 1998.
- [5] J. Hron and M. Madlik. Fluid-structure interaction with applications in biomechanics. *Nonlinear Analysis: Real World Applications*, 8:1431–1458, 2007.
- [6] J. De Hart, G.W.M. Peters, P.J.G. Schreurs, and F.P.T. Baaijens. A three-dimensional computational analysis of fluid-structure interaction in the aortic valve. *Journal of Biomechanics*, 36:101–112, 2003.
- [7] K.-J. Paik, P.M. Carrica, D. Lee, and K. Maki. Strongly coupled fluid-structure interaction method for structural loads on surface ships. *Ocean Engineering*, 36:1346–1357, 2009.
- [8] K. Fujita. Flow-induced vibration and fluid-structure interaction in nuclear power plant components. *Journal of Wind Engineering and Industrial Aerodynamics*, 33:405–418, 1990.
- [9] A.C. Khanduri, T. Stathopoulos, and C. Bedard. Wind-induced interference effects on buildings – a review of the state-of-the-art. *Engineering Structures*, 20:617–630, 1998.

- [10] W. Dettmer and J.D. Peric. A computational framework for fluid-structure interaction: Finite element formulation and application. *Computer Methods in Applied Mechanics and Engineering*, 195:5754–5779, 2006.
- [11] C.J. Greenshields H.G. Weller. A unified formulation for continuum mechanics applied to fluid-structure interaction in flexible tubes. *International Journal for Numerical Methods in Engineering*, 64:1575–1593, 2005.
- [12] K.J. Bathe and G.A. Ledezma. Benchmark problems for incompressible fluid flows with structural interactions. *Computers and Structures*, 85:628–644, 2007.
- [13] A.K. Slone, K. Pericleous, C. Bailey, and M. Cross. Dynamic fluid-structure interaction using finite volume unstructured mesh procedures. *Computers and Structures*, 80:371–390, 2002.
- [14] G. Xia and C.-L. Lin. An unstructured finite volume approach for structural dynamics in response to fluid motions. *Computers and Structures*, 86:684–701, 2008.
- [15] A. G. Malan. *Investigation into the Continuum Thermodynamic Modeling of Investment Casting Shell-Mould Drying*. PhD thesis, University of Wales Swansea, 2002.
- [16] A.G. Malan and R.W. Lewis. An artificial compressibility CBS method for modelling heat transfer and fluid flow in heterogeneous porous materials. *International Journal for Numerical Methods in Engineering*, 87:412–423, 2011.
- [17] O.F. Oxtoby, A.G. Malan, and P. Nithiarasu. A novel matrix free, edge based finite volume method for partitioned solution of fluid-structure interaction problems. *International Journal for Numerical Methods in Engineering*, submitted for review.
- [18] O. Oxtoby and A.G. Malan. A 3D, parallel fluid-structure interaction code. In *Proceedings of the 2nd African Conference on Computational Mechanics An International Conference - AfriComp11*, Cape Town, South Africa, 5-8 January 2011.
- [19] A.G. Malan and O. Oxtoby. A 3D parallel free-surface-modelling code for industrial sloshing problems. In *Proceedings of the 2nd African Conference on Computational Mechanics An International Conference - AfriComp11*, Cape Town, South Africa, 5-8 January 2011.
- [20] R. Suliman, O. Oxtoby, A.G. Malan, and S. Kok. An enhanced matrix-free edge-based finite volume approach to model structures. In S. Kok, D.N. Wilke, and H.M. Inglis, editors, *In proceedings: The 7th South African Conference on Computational and Applied Mechanics (SACAM10)*, pages 399–406, Pretoria, South Africa, 10-13 January 2010.

- [21] O. C. Zienkiewicz and R. L. Taylor. *The Finite Element Method: Volume 1 - The Basis*. Butterworth-Heinemann, Oxford, fifth edition, 2000.
- [22] S. V. Patankar. *Numerical Heat Transfer and Fluid Flow*. McGraw-Hill, New York, 1980.
- [23] E. Oñate, M. Cervera, and O. C. Zienkiewicz. A finite-volume format for structural mechanics. *International Journal for Numerical Methods in Engineering*, 37:181–201, 1994.
- [24] M.A. Wheel. A finite-volume approach to the stress analysis of pressurized axisymmetric structures. *International Journal of Pressure Vessels and Piping*, 68:311–317, 1996.
- [25] J. Fainberg and H.-J. Leister. Finite volume multigrid solver for thermo-elastic stress analysis in anisotropic materials. *Computer Methods in Applied Mechanics and Engineering*, 137:167–174, 1996.
- [26] M.A. Wheel. A finite volume method for analysing the bending deformation of thick and thin plates. *Computer Methods in Applied Mechanics and Engineering*, 147:199–208, 1997.
- [27] A.K. Slone, C. Bailey, and M. Cross. Dynamic solid mechanics using finite volume methods. *Applied Mathematical Modelling*, 27:69–87, 2003.
- [28] N. Fallah. A cell vertex and cell centred finite volume method for plate bending analysis. *Computer Methods in Applied Mechanics and Engineering*, 193:3457–3470, 2004.
- [29] R.D. Cook, D.S. Malkus, M.E. Plesha, and R.J. Witt. *Concepts and Applications of Finite Element Analysis*. John Wiley & Sons Ltd., United States, fourth edition, 2002.
- [30] P. Wenke and M.A. Wheel. A finite volume method for solid mechanics incorporating rotational degrees of freedom. *Computers and Structures*, 81:321–329, 2003.
- [31] N. Fallah, C. Bailey, M. Cross, and G.A. Taylor. Comparison of finite element and finite volume methods application in geometrically nonlinear stress analysis. *Applied Mathematical Modelling*, 24:439–455, 2000.
- [32] M. Vaz Jr., P.A. Munoz-Rojas, and G. Filippini. On the accuracy of nodal stress computation in plane elasticity using finite volumes and finite elements. *Computers and Structures*, 87:1044–1057, 2009.
- [33] J.H. Ferziger and M. Perić. *Computational Methods for Fluid Dynamics*. Springer, third edition, 2002.
- [34] J. Blazek. *Computational Fluid Dynamics: Principles and Applications*. Elsevier Science, Oxford, first edition, 2001.

- [35] X. Lv, Y. Zhao, X.Y. Huang, G.H. Xia, and X.H. Su. A matrix-free implicit unstructured multigrid finite volume method for simulating structural dynamics and fluid-structure interaction. *Journal of Computational Physics*, 225:120–144, 2007.
- [36] Z.C He, G.R. Liu, Z.H. Zhong, G.Y. Zhang, and A.G. Cheng. Coupled analysis of 3D structural-acoustic problems using the edge-based smoothed finite element method/finite element method. *Finite Elements in Analysis and Design*, 46:1114–1121, 2010.
- [37] S. Mitra and K.P. Sinhamahapatra. 2D simulation of fluid-structure interaction using finite element method. *Finite Elements in Analysis and Design*, 45:52–59, 2008.
- [38] T.E. Tezduyar, S. Sathe, R. Keedy, and K. Stein. Space-time finite element techniques for computation of fluid-structure interactions. *Computer Methods in Applied Mechanics and Engineering*, 195:2002–2027, 2006.
- [39] P.R.F. Texeira and A.M. Awruch. Numerical simulation of fluid-structure interaction using the finite element method. *Computers and Fluids*, 34:249–273, 2005.
- [40] J. Degroote, R. Haelterman, S. Annerel, P. Bruggeman, and J. Vierendeels. Performance of partitioned procedures in fluid-structure interaction. *Computers and Structures*, 88:446–457, 2010.
- [41] M. von Scheven and E. Ramm. Strong coupling schemes for interaction of thin-walled structures and incompressible flows. *International Journal for Numerical Methods in Engineering*, 87:214–231, 2011.
- [42] U. Küttler and W. A. Wall. Fixed-point fluid–structure interaction solvers with dynamic relaxation. *Computational Mechanics*, 43:61–72, 2008.
- [43] W. A. Wall, S. Genkinger, and E. Ramm. A strong coupling partitioned approach for fluid–structure interaction with free surfaces. *Computers and Fluids*, 36:169–183, 2007.
- [44] D. P. Mok and W. A. Wall. Partitioned analysis schemes for the transient interaction of incompressible flows and nonlinear flexible structures. In W. A. Wall and K.-U. Bletzinger, editors, *Trends in computational structural mechanics*, pages 689–698, Barcelona: CIMNE, 2011.
- [45] P. Le Tallec and J. Mouro. Fluid structure interaction with large structural displacements. *Computer Methods in Applied Mechanics and Engineering*, 190:3039–3067, 2001.
- [46] H. G. Matthies and J. Steindorf. Partitioned strong coupling algorithms for fluid–structure interaction. *Computers and Structures*, 81:805–812, 2003.

- [47] J. Vierendeels, L. Lanoye, J. Degroote, and P. Verdonck. Implicit coupling of partitioned fluid-structure interaction problems with reduced order models. *Computers and Structures*, 85:970–976, 2007.
- [48] J. Degroote, K. J. Bathe, and J. Vierendeels. Performance of a new partitioned procedure versus a monolithic procedure in fluid-structure interaction. *Computers and Structures*, 87:793–801, 2009.
- [49] G.A. Holzapfel. *Nonlinear Solid Mechanics: A continuum Approach for Engineering*. John Wiley & Sons Ltd., West Sussex, England, 2001.
- [50] O. C. Zienkiewicz and R. L. Taylor. *The Finite Element Method: Volume 2 - Solid Mechanics*. Butterworth-Heinemann, Oxford, fifth edition, 2000.
- [51] R. Löhner. *Applied CFD Techniques*. John-Wiley and Sons Ltd., Chichester, 2001.
- [52] Y. Zhao and B. Zhang. A high-order characteristics upwind FV method for incompressible flow and heat transfer simulation on unstructured grids. *International Journal for Numerical Methods in Engineering*, 37:3323–3341, 1994.
- [53] I. Bijelonja, I. Demirdzic, and S. Muzafferija. A finite volume method for incompressible linear elasticity. *Computer Methods in Applied Mechanics and Engineering*, 195:6378–6390, 2006.
- [54] W. Pan, M.A. Wheel, and Y. Qin. Six-node triangle finite volume method for solids with a rotational degree of freedom for incompressible material. *Computers and Structures*, 88:1506–1511, 2010.
- [55] G.A. Taylor, C. Bailey, and M. Cross. Solution of the elastic/visco-plastic constitutive equations: A finite volume approach. *Applied Mathematical Modelling*, 19:746–760, 1995.
- [56] G.A. Taylor, C. Bailey, and M. Cross. A vertex-based finite volume method applied to non-linear material problems in computational solid mechanics. *International Journal for Numerical Methods in Engineering*, 56:507–529, 2003.
- [57] S. Kok. Class notes MSY 411 continuum mechanics notes. *Department of Mechanical and Aeronautical Engineering, University of Pretoria*, February 2007.
- [58] P. I. Crumpton, P. Moinier, and M. B. Giles. An unstructured algorithm for high Reynolds number flows on highly stretched meshes. In C. Taylor and J. T. Cross, editors, *Numerical Methods in Laminar and Turbulent Flow*, pages 561–572. Pineridge Press, 1997.
- [59] A. G. Malan and R. W. Lewis. Modeling coupled heat and mass transfer in drying non-hygroscopic capillary particulate materials. *Communications in Numerical Methods in Engineering*, 19(9):669–677, 2003.

- [60] A. Jameson. Time dependent calculations using multigrid, with applications to unsteady flows past airfoils and wings. *AIAA Paper*, 91-1596, 1991.
- [61] V. Venkatakrishnan and D. J. Mavriplis. Implicit method for the computation of unsteady flows on unstructured grids. *Journal of Computational Physics*, 127:380–397, 1996.
- [62] T. Beléndez, C. Neipp, and A. Beléndez. Large and small deflections of a cantilever beam. *European Journal of Physics*, 23:371–379, 2002.
- [63] C.W. Hirt, A.A. Amsden, and J.L. Cook. An arbitrary Lagrangian-Eulerian computing method for all flow speeds. *Journal of Computational Physics*, 14:227–253, 1974.
- [64] O.F. Oxtoby and A.G. Malan. A matrix-free, implicit, incompressible fractional-step algorithm for fluid-structure interaction applications. *Journal of Computational Physics*, submitted for review.
- [65] C. Farhat, M. Lesoinne, and P. LeTallec. Load and motion transfer algorithms for fluid/structure interaction problems with non-matching discrete interfaces: Momentum and energy conservation, optimal discretization and application to aeroelasticity. *Computer Methods in Applied Mechanics and Engineering*, 157:95–114, 1998.
- [66] A. de Boer, A.H. van Zuijlen, and H. Bijl. Review of coupling methods for non-matching meshes. *Computer Methods in Applied Mechanics and Engineering*, 196:1515–1525, 2007.
- [67] G. Karypis and V. Kumar. A fast and high quality multilevel scheme for partitioning irregular graphs. *SIAM Journal on Scientific Computing*, 20(1):359–392, 1999.
- [68] W. Wall. *Fluid-struktur-interaktion mit stabilisierten finiten elementen*. PhD thesis, Universitat Stuttgart, 1999.